N° d'ordre: .....

République Algérienne Démocratique et Populaire
Ministère de l'Enseignement Supérieur et de la Recherche Scientifique

Université Yahia Farès de Médéa
Faculté de Technologie
Département de Génie Électrique

THÈSE

En vue de l'obtention du diplôme de

Doctorat LMD en Génie électrique

Filière: *Automatique*
Spécialité: *Automatique et Informatique Industrielle*

Présentée par:
HALITIM Ali Mounir

THÈME :

Contribution au développement d'un système de localisation intelligent : Application à l'agriculture de précision

Soutenue publiquement le : 23/06/2024

Devant le jury composé de :

M. OULD ZMIRLI Mohamed	**Prof.**	**Université de Médéa**	**Président**
M. BOUHEDDA Mounir	**Prof.**	**Université de Médéa**	**Directeur de thèse**
Mme BENBLIDIA Nadjia	**Prof.**	**Université de Blida 1**	**Examinatrice**
M. DJENDI Mohamed	**Prof.**	**Université de Blida 1**	**Examinateur**
M. BENGHERBIA Billel	**MCA**	**Université de Médéa**	**Examinateur**
M. TCHOKECTH KEBIR Sofiane	**MCB**	**Université de Médéa**	**Invité**

Thèse préparée au sein du Laboratoire des Systèmes Électroniques Avancés (LSEA)
de l'Université de Médéa, ALGÉRIE

People's Democratic Republic of Algeria
Ministry Of Higher Education And Scientific Research

Yahia Farès University of Médéa
Faculty of Technology
Department of Electrical Engineering



THESIS

To obtain the title of

LMD Doctorate in Electrical Engineering

Major: *Automatic Control*
Speciality: *Automatic Control and Industrial Computing*

Presented by:

HALITIM Ali Mounir

THESIS :

Contribution to the development of an intelligent localization system: Application to precision agriculture

Publicly defended on : 23/06/2024

Jury :

Mr OULD ZMIRLI Mohamed	Prof.	University of Médéa	President
Mr BOUHEDDA Mounir	Prof.	University of Médéa	Supervisor
Ms BENBLIDIA Nadjia	Prof.	University of Blida 1	Reviewer
Mr DJENDI Mohamed	Prof.	University of Blida 1	Reviewer
Mr BENGHERBIA Billel	MCA	University of Médéa	Reviewer
Mr TCHOKECTH KEBIR Sofiane	MCB	University of Médéa	Invited

Thesis prepared within the Laboratory of Advanced Electronic Systems (LSEA)
at the University of Médéa, ALGERIA

Dedications

To My Beloved Parents,

Your unconditional love and sacrifices have guided me through every step of my life. I dedicate this achievement to you with profound gratitude and admiration.

To My Wonderful Wife,

Your unwavering belief in me has been my greatest source of strength. I dedicate this thesis to you.

To My Amazing Kids,

You are my greatest joy and motivation. Your smiles light up my darkest days, and your presence fills my life with meaning. I dedicate this thesis to you, hoping to inspire you to pursue your dreams with the same passion and dedication.

To My Supportive Brothers,

I dedicate this thesis to you as a token of my appreciation for always being there for me.

To My Dear Friends,

This thesis is dedicated to our friendship, which I know you will recognize yourselves in.

With deepest gratitude and affection,

Ali Mounir HALITIM

Acknowledgments

I wish to express my heartfelt gratitude to **Prof. Mounir BOUHEDDA**, my thesis supervisor, for his guidance, unwavering availability, and generous sharing of his wealth of experience. I am sincerely thankful and immensely proud to have had the privilege of collaborating with him throughout my research journey.

I would like to extend my gratitude to **Dr. TCHOKETCH KEBIR Sofiane** for being a supportive co-supervisor and for his invaluable guidance throughout my doctoral studies.

My deepest gratitude goes to **Prof. OULD ZMIRLI Mohamed** for chairing the jury of my doctoral thesis defense. I am equally grateful to the esteemed members of the jury: **Prof. BENBLIDIA Nadjia**, **Prof. DJENDI Mohamed**, and **Dr. BENGHERBIA Billel**. Their insightful questions and constructive feedback were invaluable and significantly contributed to the success and enriching nature of the examination.

I would also like to thank **Dr. Samia REBOUH** for her contribution to the writing of the publications.

My appreciation goes to the members of the Laboratory of Advanced Electronic Systems and its president, **Prof. OULD ZMIRLI Mohamed**.

My sincere thanks go to the countless teachers and professors, from my earliest years to university, who have guided and inspired me throughout my academic journey.

List of Publications

The research work included in this thesis has led to the following publications:

International Research Articles:

A. M. Halitim, M. Bouhedda, S. Tchoketch-Kebir, and S. Rebouh, "Artificial neural network for tilt compensation in yaw estimation," Trans. Inst. Meas. Control, pp. 1–10, 2023.

URL: *https://journals.sagepub.com/doi/abs/10.1177/01423312231214832*

A. M. Halitim, M. Bouhedda, S. Tchoketch-Kebir, and S. Rebouh, "Real-Time Implementation of Relative Positioning Approaches Using Low-Cost Single-Frequency GPS Receivers and Raspberry Pi Platform for Agriculture Applications," J. Control. Autom. Electr. Syst., pp. 1–14, 2024.

URL: *https://link.springer.com/article/10.1007/s40313-024-01069-x*

International Conferences:

A. M. Halitim, M. Bouhedda, and S. Tchoketch-Kebir, "Assessment of a Real-time Relative Positioning Method in Urban Area Using Low-cost Single-frequency GPS Receivers," in 1st International Conference on Engineering and Applied Natural Sciences, ICEANS 2022, 10-13 May 2022, Konya, Turkey, pp. 1148–1154.

URL: *https://www.iceans.org/1-st-iceans-2022*

ملخص

في ظل التحديات البيئية المتزايدة والمطالب الزراعية المتنامية، أصبح الانتقال نحو تقنيات الزراعة الحديثة عالية الدقة أمراً حتمياً. غالباً ما ينطوي هذا التحول على دمج المركبات الزراعية الذاتية التحكم، حيث يعد التقدير الدقيق للموقع و زوايا التوجيه أمرا أساسيا لضمان تشغيل فعّال وإدارة فعّالة للموارد.

يقــوم الجزء الأول من هذه الرسالة البحثية بدراسة إمكانية استخدام تقنيات تحديد المواقع النسبي باستخدام نظام تحديد المواقع العالمي في الوقت الفعلي لتطبيقات الزراعة بدلاً من حلول تحديد المواقع المطلقة التقليدية. باستخدام أجهزة استقبال منخفضة التكلفة أحادية التردد، تظهر نتائجنا تحسناً ملحوظا في دقة التحديد بالمقارنة مع تحديد المواقع المطلق، وهو مستوى من الدقة يضاهي بعض خدمات نظام تحديد المواقع العالمي التفاضلي، مما يسمح بالتنفيذ الفعال لعدد من العمليات الزراعية.

يتناول الجزء الثاني من هذه الرسالة البحثية جانباً من اشكالية تقدير الاتجاه، وهو تحديداً تعويض الميل في تقدير الانحراف الأفقي وقد كشفت التجارب المنجزة عن نقائص طريقة تعويض الميل التقليدية. بعد ذلك، تم اقتراح طريقة تعتمد على التعلم الآلي باستخدام شبكة عصبية اصطناعية. تُظهر النتائج التي تم الحصول عليها باستخدام وحدة قياس بالقصور الذاتي ذات التكلفة المنخفضة تفوق النظام المقترح على طريقة تعويض الميل التقليدية وعلى اثنتين من خوارزميات تقدير الاتجاه.

كلمات مفتاحية : شبكة عصبية اصطناعية، نظام تحديد المواقع العالمي، الزراعة الدقيقة، تحديد المواقع النسبي، وحدة قياس بالقصور الذاتي، تعويض الميل، تقدير الانحراف الأفقي

Résumé

Face aux exigences croissantes de l'agriculture et aux défis environnementaux, il est devenu impératif d'adopter les techniques modernes de l'agriculture de précision. Cette transition implique généralement l'utilisation de véhicules agricoles autonomes, dont l'estimation de la position et de l'orientation joue un rôle crucial dans l'assurance d'une utilisation efficace et d'une gestion optimale des ressources.

La première partie de cette thèse évalue la possibilité d'utiliser des approches de positionnement relatives basées sur le GPS en temps réel pour les applications agricoles, en remplacement des solutions de positionnement absolu habituelles. En utilisant des récepteurs GPS à bas coût et à fréquence unique, les résultats obtenus mettent en évidence une amélioration significative de la précision de positionnement par rapport au positionnement GPS absolu. Ce niveau de précision est comparable à celui de certains services DGPS, ce qui permet l'exécution efficace de diverses opérations agricoles.

La seconde partie de cette thèse aborde un aspect spécifique de l'estimation d'orientation, à savoir la compensation de l'inclinaison dans l'estimation du lacet. Des expériences pratiques ont permis de mettre en évidence les limitations de la méthode conventionnelle de compensation de l'inclinaison. Par la suite, une méthode intelligente utilisant un réseau de neurones artificiels a été proposée. Les résultats obtenus avec une unité de

mesure inertielle à faible coût démontrent la supériorité de notre approche par rapport à la méthode conventionnelle de compensation de l'inclinaison et à deux algorithmes bien établis d'estimation d'orientation.

Mots clés: Agriculture de Précision, Compensation de l'Inclinaison, Estimation du Lacet, Global positioning system (GPS), Positionnement relatif, Réseau de Neurones, Unité de Mesure Inertielle.

Abstract

In the face of growing agricultural demands and environmental challenges, a transition towards modern precision agriculture techniques has become imperative. This shift often involves integrating autonomous agricultural vehicles, whose precise positioning and orientation estimation play a vital role in ensuring efficient operation and resource management.

The first part of this thesis explores the feasibility of employing real-time GPS-based relative positioning approaches for agriculture applications instead of the typical absolute positioning solutions. Using low-cost single-frequency GPS receivers, our findings showcase a notable enhancement in positioning accuracy compared to standalone GPS positioning. This level of accuracy is comparable to certain DGPS services, enabling the effective execution of various farming operations.

The second part of this thesis addresses a particular aspect in orientation estimation, specifically, the tilt compensation in yaw estimation. Through a series of experiments, the limitations of the conventional tilt compensation method have been revealed. Subsequently, a machine-learning method employing an Artificial Neural Network (ANN) was proposed. Results obtained using a low-cost Inertial Measurement Unit (IMU) demonstrate the superiority of our approach over the conventional tilt-compensation method and two well-established orientation estimation algorithms.

Keywords : Artificial Neural Network (ANN), Global positioning system (GPS), Inertial Measurement Unit (IMU), Precision Agriculture, Relative positioning, Tilt Compensation, Yaw Estimation.

Contents

List of Figures . . . x
List of Tables . . . xi
List of Abbreviations . . . xii

I Introduction **1**
I.1 Background, Motivation and Problem Statement . . . 2
I.1.1 For Positioning . . . 2
I.1.2 For Orientation . . . 3
I.2 Novel Research Contributions . . . 4
I.3 Dissertation Organization . . . 4

II Positioning Systems in Agriculture **6**
II.1 Introduction . . . 6
II.2 Previous Developments . . . 7
II.2.1 Mechanical-based Systems . . . 7
II.2.2 Odometry Sensors . . . 8
II.2.3 Inertial Sensors . . . 8
II.2.4 Camera-based Sensors . . . 9
II.2.5 Laser Scanner Sensors . . . 9
II.2.6 Ultrasonic Sensors . . . 9
II.2.7 Discussion . . . 10
II.3 Satellite-based Positioning Systems . . . 10
II.3.1 GPS for Precision Agriculture . . . 11
II.3.2 GPS Overview . . . 12
II.3.2.1 GPS Segments . . . 12
II.3.2.2 GPS working principle . . . 13
II.3.2.3 GPS Signal . . . 13
II.3.2.4 GPS Measurement Observables . . . 15
II.3.2.5 GPS Augmentation Systems . . . 18
II.3.2.6 GPS-based Relative Positioning . . . 20
II.4 Conclusion . . . 20

III Experimental Evaluation of GPS-Based Relative Positioning Approaches for Agriculture Applications **22**
III.1 Introduction . . . 22
III.2 Motivation . . . 22
III.3 Literature Review and Contribution . . . 24
III.3.1 Literature Review . . . 24
III.3.2 Contribution . . . 26
III.4 GPS Error Sources and Pseudorange Model . . . 26
III.4.1 GPS Error Sources . . . 27
III.4.1.1 Satellite Clock Error . . . 27
III.4.1.2 Receiver Clock Error . . . 27

III.4.1.3 Atmospheric Errors . . . 28
III.4.1.4 Ephemeris Error . . . 28
III.4.1.5 Multipath Error . . . 29
III.4.1.6 Non-Modeled Errors . . . 29
III.4.2 GPS Pseudorange Model . . . 29
III.5 GPS-based Relative Positioning Approaches . . . 30
III.5.1 Absolute Position Differencing (APD) . . . 30
III.5.2 Pseudorange Single Differencing (PSD) . . . 30
III.5.3 Pseudorange Double Differencing (PDD) . . . 32
III.6 Hardware Architecture . . . 33
III.6.1 u-blox NEO-6M GPS Module . . . 34
III.6.2 nRF24l01+ Radio Transceiver . . . 34
III.6.3 Raspberry Pi 3 Compute Module . . . 35
III.6.4 System Setup . . . 36
III.7 Implementation . . . 38
III.7.1 GPS Data Extraction . . . 39
III.7.2 GPS Data Exchange . . . 40
III.7.3 APD, PSD and PDD Implementation . . . 42
III.8 Experiments, Results and Discussion . . . 43
III.8.1 Experiments and Results . . . 43
III.8.2 Comparison between APD, PSD and PDD . . . 45
III.8.3 PDD Approach for Agriculture Applications . . . 48
III.9 Conclusion . . . 49

IV Orientation Estimation : Sensors and Algorithms 51
IV.1 Introduction . . . 51
IV.2 Definitions and Common Concepts . . . 52
IV.2.1 Definitions . . . 52
IV.2.1.1 Orientation and its Applications . . . 52
IV.2.1.2 Orientation vs. Attitude . . . 52
IV.2.1.3 Orientation vs. Rotation . . . 53
IV.2.1.4 Determination vs. Estimation . . . 53
IV.2.2 Coordinate Frames . . . 53
IV.2.2.1 Body Frame . . . 54
IV.2.2.2 ECEF Frame . . . 54
IV.2.2.3 Local Level Frame . . . 54
IV.2.3 Orientation Representations . . . 55
IV.2.3.1 Euler Angles . . . 55
IV.2.3.2 Quaternions . . . 56
IV.2.3.3 Direction Cosine Matrix (DCM) . . . 57
IV.2.3.4 Other representations . . . 58
IV.2.3.5 Conversion between Representations . . . 59
IV.3 Sensors for Orientation Estimation . . . 60
IV.3.1 Vision-based . . . 60
IV.3.2 GNSS-based . . . 61
IV.3.3 Light Detection And Ranging (LiDAR)-based . . . 61
IV.3.4 Inertial Measurement Unit . . . 61
IV.4 Algorithms for Orientation Estimation . . . 62
IV.4.1 IMU Mathematical Model . . . 62
IV.4.1.1 Accelerometer Output Model . . . 63
IV.4.1.2 Gyroscope Output Model . . . 63
IV.4.1.3 Magnetometer Output Model . . . 63

IV.4.2 Kalman Filters . . . 64
IV.4.2.1 Linear Kalman Filter (LKF) . . . 65
IV.4.2.2 Extended Kalman Filter (EKF) . . . 66
IV.4.2.3 Other Non-linear Kalman Filters . . . 67
IV.4.3 Complementary Filters . . . 68
IV.4.3.1 Madgwick Filter . . . 69
IV.4.3.2 Mahony Filter . . . 70
IV.4.4 Neural Networks . . . 71
IV.4.5 Discussion . . . 73
IV.5 Conclusion . . . 73

V A Machine Learning-based Method for Tilt Compensation in Yaw Estimation 74
V.1 Introduction . . . 74
V.2 Magnetometer Measurements Calibration . . . 74
V.3 Conventional Tilt compensation Method . . . 76
V.3.1 Description of the Conventional Tilt Compensation Method . . . 76
V.3.2 Assessment of the Conventional Tilt Compensation Method . . . 78
V.3.2.1 Pitch and Roll Estimation . . . 78
V.3.2.2 Assessment with MPU9250 . . . 79
V.3.2.3 Assessment with Samsung Galaxy M51 . . . 80
V.4 Solution Approach . . . 81
V.4.1 Motivation . . . 82
V.4.2 Inputs and Outputs Selection . . . 83
V.4.3 Dataset Collection . . . 83
V.4.4 ANN architecture and Training . . . 84
V.5 Results and Discussion . . . 88
V.6 Conclusion . . . 91

VI Conclusions 92
VI.1 Findings and Contributions . . . 92
VI.1.1 For Positioning . . . 92
VI.1.2 For Orientation . . . 93
VI.2 Recommendations for Future Work . . . 93
VI.2.1 For Positioning . . . 93
VI.2.2 For Orientation . . . 94

List of Figures

II.1 Agricultural tractor with automated steering system. 7
II.2 Role of GPS in the precision agriculture cycle. 11
II.3 Trilateration principle. 13
II.4 GPS signal interface definition. 14
II.5 GPS L1 signal composition. 16
II.6 Pseudorange measurement timing relationships. 17
II.7 Pictorial representation of the use of GPS-based relative positioning for agriculture applications. 21

III.1 SBAS service areas 23
III.2 A block diagram that shows the used methods 26
III.3 Baseline estimation between two nodes using pseudorange differencing 31
III.4 Determination of unit vector toward satellite using azimuth and elevation angles 32
III.5 Hardware composition of the proposed system 33
III.6 u-blox NEO-6M GPS Module 34
III.7 nRF24l01+ Radio Transceiver 35
III.8 Raspberry Pi 3b+ Compute Module 36
III.9 Raspberry Pi 3b+ GPIO definition 37
III.10 Raspberry Pi 3b+ and u-blox NEO-6M GPS module wiring 37
III.11 Raspberry Pi 3b+ and nRF24l01+ radio transceiver wiring 38
III.12 High-level block scheme describing the workflow at each node 39
III.13 Details of GPS data extraction 41
III.14 Timing of the GPS Data Exchange 42
III.15 Flowcharts of APD, PSD and PDD approaches 43
III.16 Experiments description 44
III.17 Comparison between APD, PSD and PDD for Scenario SD 46
III.18 Static-Static 6 m experiment results for both campaigns 47
III.19 Histograms of the scenario SS estimation error obtained by APD, PSD and PDD 48
III.20 CDFs of distance error obtained by APD, PSD and PDD for scenario SS in the agricultural field 49
III.21 Comparison between results obtained by PDD and standalone GPS positioning 50

IV.1 Visualization of the rotational (left) and translational (right) motions of a rigid body 51
IV.2 Examples of orientation estimation applications 52
IV.3 Body frame 54
IV.4 Euler angles Definition ((a): yaw, (b): pitch, and (c): roll) 55
IV.5 A and B reference frames 57
IV.6 Functioning principle of KFs 64
IV.7 Block diagram of EKF algorithm 67
IV.8 Block diagram of Madgwick filter 70
IV.9 Block diagram of Mahony filter 71

IV.10 A block diagram that describes the use of NNs in orientation estimation . . . 72

V.1 MPU9250 9 DoF motion sensor . . . 76
V.2 Raspberry Pi 3b+ and MPU9250 module wiring . . . 76
V.3 Magnetometer measurements calibration . . . 77
V.4 Yaw determination using a tri-axis magnetometer . . . 78
V.5 3D non-magnetic scaled platform . . . 79
V.6 Pitch and roll estimation results with Madgwick filter . . . 79
V.7 Pitch and roll estimation results with Mahony filter . . . 80
V.8 Conventional tilt compensation method assessment with MPU9250 . . . 80
V.9 Compass Galaxy application within the Samsung Galaxy M51 smartphone . 81
V.10 Conventional tilt compensation method assessment with Samsung Galaxy M51 smartphone . . . 82
V.11 Inputs and outputs of the adopted ANN model . . . 83
V.12 High-level block scheme describing the dataset collection process . . . 84
V.13 *Google Colab* environment and *Python* programming language . . . 85
V.14 Scheme of ANN training process . . . 86
V.15 ANN's adopted architecture . . . 87
V.16 Performance comparison between different ANN architectures . . . 87
V.17 Training loss history with Adam and SGD optimizers . . . 88
V.18 CDFs of yaw estimation error obtained by the four methods . . . 89
V.19 Histograms of the four methods estimation errors . . . 89
V.20 Performance comparison summary . . . 90

List of Tables

III.1 GPGGA message details 40
III.2 Structure of the exchanged packets 41
III.3 Performance Statistics of APD, PSD and PDD for Scenarios SS and DD . . . 45

IV.1 Multiplication rules of the fundamental quaternion units 56

V.1 Some of the obtained results using different ANN architectures 85
V.2 Statistical results and computational time of the four methods 88

List of Abbreviations

Adam : Adaptive Moment Estimation
AHRS : Attitude and Heading Reference System
AI : Artificial Intelligence
ANN : Artificial Neural Network
APD : Absolute Position Differencing
C/A : Coarse/Acquisition
CDF : Cumulative Distribution Function
CF : Complementary Filter
CKF : Cubature Kalman filter
CPU : Central Processing Unit
DC : Direct Current
DCM : Direction Cosine Matrix
DGPS : Differential Global Positioning System
DoF : Degree of Freedom
ECEF : Earth-Centered Earth-Fixed
ECI : Earth-Centered Inertial frame
EKF : Extended Kalman Filter
ENU : East-North-Up
GNSS : Global Navigation Satellite System
GPIO : General Purpose Input/Output
GPS : Global Positioning System
GPU : Graphics Processing Unit
I2C : Inter-Integrated Circuit
IAR : Inter-Agent Ranging
IDE : Integrated Development Environment
IMU : Inertial Measurement Unit
ISM : Industrial, Scientific and Medical
ITS : Intelligent Transportation System
KF : Kalman Filter
KNN : K-Nearest Neighbor
LADGPS : Local-area Differential Global Positioning System
LIDAR : Light Detection and Ranging
LKF : Linear Kalman Filter
LNAV : Legacy Navigation
LSTM : Long Short-Term Memory
MARG : Magnetic, Angular Rate and Gravity
MEMS : Micro-Electro-Mechanical Systems

MIMU : Magnetic and Inertial Measurement Unit
ML : Machine Learning
MLP : Multilayer Perceptron
MSE : Mean Square Error
NED : North-East-Down
NMEA : National Marine Electronics Association
NN : Neural Network
OS : Operating System
PA : Precision Agriculture
PDD : Pseudorange Double Differencing
PDOP : Precision Dilution of Precision
PI : Proportional-Integral
PPS : Precise Positioning Service
PRN : Pseudorandom Noise
PSD : Pseudorange Single Differencing
PVT : Position, Velocity and Time
RAM : Random Access Memory
RF : Radio Frequency
RFD : Right-Forward-Down
RFID : Radio Frequency Identification
RFU : Right-Forward-Up
RMSE : Root Mean Square Error
RNN : Recurrent Neural Network
RTK : Real-Time Kinematic
SBAS : Satellite-Based Augmentation System
SGD : Stochastic Gradient Descent
SNR : Signal to Noise Ratio
SoC : System on Chip
SPI : Serial Peripheral Interface
SPS : Standard Positioning Service
SVR : Support Vector Regression
TDOA : Time Difference of Arrival
TOA : Time of Arrival
TOF : Time of Flight
UART : Universal Asynchronous Receiver-Transmitter
UAV : Unmanned Aerial Vehicle
UKF : Unscented Kalman Filter
USB : Universal Serial Bus
UTC : Coordinated Universal Time
VRA : Variable Rate Application
WAAS : Wide Area Augmentation System
WADGPS : Wide-area Differential Global Positioning System

Chapter I

Introduction

Over the past century, remarkable progress have occurred in the field of agriculture, propelled by various technological breakthroughs and innovations in production systems. In this context, agricultural production has more than tripled between 1960 and 2015 [1]. Nevertheless, hunger and malnutrition remain as significant challenges in many regions of the world.

In the meantime, the global population is expanding by approximately 240,000 individuals each day. This growth is expected to be mainly concentrated in Africa and South Asia. By 2100, projections suggest that Asia and Africa will accommodate over 80% of the world's population, constituting 9 billion out of a projected total of 11 billion people [1].

In these regions of the world, farmers encounter the highest number of obstacles in addressing the continually increasing demands of the population. These challenges are primarily attributed to the exhaustion and volatility of natural resources, aggravated by the persistent reliance on traditional agricultural practices.

Projections suggest that agricultural production must rise by 70% in order to meet the food needs of the growing population by 2050 [2]. To maximize the use of existing resources and achieve optimal yields, it is imperative for many countries to enhance their agricultural sector through the adoption of innovative precision agriculture techniques. Employing these methods not only enhances food production but also ensures sustainable utilization of available resources.

Precision agriculture can be defined as "The application of modern information technologies to provide, process and analyze multi-source data of high spatial and temporal resolution for decision making and operations in the management of crop production" [3]. Consequently, the majority of precision agriculture techniques involve collecting data on crop health and soil condition, as well as automating various operations such as soil tillage, planting, spraying, and harvesting. Thus, the implementation of precision agriculture often necessitates the utilization of agricultural vehicles.

The manual guidance of these vehicles is an extremely challenging task, requiring operators to navigate along desired paths for extended periods, covering large areas while

avoiding crop damage and ensuring the proper functioning of equipment. Autonomous or semi-autonomous vehicles are emerging as increasingly utilized means in agriculture. They possess the ability to perform multiple agricultural tasks without the need for direct and constant human oversight. By enhancing and transforming conventional agricultural methods, these autonomous vehicles can be part of the solution to the growing demand for food.

One of the pivotal aspects concerning autonomous vehicles, ground or aerial, is the determination of their positions and orientations. This information can be employed for various purposes, including controlling and guiding them, mapping agricultural fields, and gathering information. It is noteworthy that in the literature, certain sources include orientation estimation within the concept of positioning [4]. However, in our study, the term positioning will specifically denote the calculation of position without encompassing orientation, which will be addressed separately as another subject.

I.1 Background, Motivation and Problem Statement

I.1.1 For Positioning

Over the years, various positioning solutions tailored specifically to agricultural applications have been developed and proposed. These solutions encompass mechanical, optical, radio and ultrasonic positioning systems as well as a dead reckoning solution. However, many of these technologies either lack the necessary accuracy for widespread field applications or appear impractical due to their heavy reliance on large-scale or complex installation.

By successfully addressing these limitations, satellite-based positioning systems have emerged as the predominant choice for agricultural applications. The general term "Global Navigation Satellite Systems" (GNSS) has been used to encompass the existing satellites constellations, including the Global Positioning System (GPS).

Two types of GPS receivers exist: single-frequency and multi-frequency. While multi-frequency GPS receivers offer centimeter-level accuracy, their high cost, often several thousand US dollars, make them inaccessible to many farmers [5]. In contrast, low-cost single-frequency GPS receivers dominate the market due to their affordability. Thus, many efforts have been put to enhance their accuracy, typically up to tens of meters, through various augmentation systems [6].

The primary augmentation systems are Differential GPS (DGPS) services, aimed at refining absolute position estimation for GPS receivers. These systems are typically categorized into Wide-area DGPS (WADGPS) and Local-area DGPS (LADGPS) services [7]. Current WADGPS services are primarily regional and do not extend coverage to areas in Africa and South America [8]. On the other hand, LADGPS services are uncommon in various regions due to their reliance on large-scale infrastructures or specific hardware support, some of which are either inaccessible or expensive.

Given the unavailability of augmentation systems in different regions in the world and considering the correlation between the accuracy of standalone GPS receivers and their

cost, relative positioning may be a viable alternative for accurate positioning purposes in agriculture applications.

In fact, current positioning systems tailored for agriculture applications typically aim to determine absolute positions. However, considering the scenario where one GPS receiver is positioned in a known location near an agricultural field, determining accurate relative positions with respect to this static receiver could suffice. This approach enables the accurate positioning of other mobile vehicles equipped with GPS receivers within the agricultural field.

Consecutively, the first part of this thesis will explore the feasibility of employing real-time relative positioning approaches for agriculture applications instead of the typical absolute positioning solutions. The aim is to implement and assess various GPS-based relative positioning approaches for agriculture applications based on the sharing of GPS data.

I.1.2 For Orientation

In the realm of orientation estimation, a multitude of sensors are employed to accurately determine the spatial orientation of objects. Among these sensors, Inertial Measurement Units (IMUs) have emerged as the predominant choice. An IMU typically integrates three primary sensors: accelerometers, gyroscopes, and magnetometers. Accelerometers measure linear acceleration, gyroscopes track angular velocity, and magnetometers detect magnetic fields.

IMUs have gained popularity owing to advancements in Micro-Electro-Mechanical Systems (MEMS) technology. This technology enables the development of compact, lightweight, and cost-effective modules for orientation estimation [9]. The integration of MEMS technology has revolutionized the field of orientation estimation by facilitating the production of IMUs that are both highly accurate and commercially accessible. These IMUs are now widely employed in various applications, including aerospace, robotics, and, notably, agriculture.

The utilization of IMUs has prompted the development of numerous algorithms to fuse data from the accelerometer, gyroscope, and magnetometer sensors. Among these algorithms, Kalman filters (KFs) and Complementary filters (CFs) are the most commonly employed [10]. These filters have proven to be effective in combining sensor readings to accurately estimate orientation in real-time applications.

The combination of accelerometer and gyroscope measurements has yielded precise estimations for pitch and roll angles. However, determining the yaw angle poses a significant challenge. This is because, unlike pitch and roll, accelerometers cannot detect rotations about the z-axis when the sensor frame aligns with the Earth's frame, in addition to the gyroscope's drift [11].

Yaw estimation introduces another challenge due to its susceptibility to external magnetic fields, such as those caused from nearby metallic objects. This interference can obstruct the magnetometer's ability to accurately determine yaw, emphasizing the importance of sensor calibration. Another difficulty arises when the sensor is not aligned parallel to the Earth's

surface. In such cases, a conventional tilt compensation method is typically employed to mitigate inaccuracies.

In the second part of this thesis, we will evaluate the effectiveness of this conventional approach. Based on our findings, we will propose an Artificial Intelligence (AI)-based method to tackle this issue. Moreover, we will evaluate the effectiveness of the proposed solution not only compared to the conventional tilt compensation method but also against two established orientation estimation algorithms.

I.2 Novel Research Contributions

Consistent with the focus of our thesis, titled "Contribution to the development of an intelligent localization system: Application to precision agriculture," our research seeks to present a low-cost positioning system tailored for agricultural use, leveraging GPS-based relative positioning techniques. Furthermore, as part of integrating an "intelligent" dimension into our work, we introduce an AI-based methodology to address a specific aspect of orientation, namely tilt compensation in yaw estimation.

This dissertation makes the following contributions to the relevant body of positioning and orientation estimation research:

- Implementation of various GPS-based relative positioning approaches in real-time, namely Absolute Position Differencing (APD), Pseudorange Single Differencing (PSD), and Pseudorange Double Differencing (PDD). This marks a novel contribution to the field, as previous works predominantly utilized these methods in post-processing mode;
- Evaluation and analysis of the suitability of these relative positioning techniques for agricultural applications, utilizing low-cost single-frequency GPS receivers. Experiments are conducted in both open-sky environments and agricultural fields;
- Execution of a series of experiments to identify the shortcomings of the conventional tilt compensation method employed in yaw estimation;
- Introduction of an innovative AI-based solution, employing Neural Networks to compensate for tilt in yaw estimation using raw measurements obtained from a low-cost IMU. Comparative analysis is conducted not only against the conventional method but also against two established CFs.

I.3 Dissertation Organization

The subsequent sections of this dissertation are structured as follows. The upcoming chapter, Chapter II, presents a comprehensive overview of positioning systems employed in agriculture. It traces the evolution from traditional methods to the latest techniques and recent research works. A particular interest is given to satellite-based positioning systems.

Chapter III starts by recalling fundamental aspects concerning GPS-based relative positioning approaches. Building upon this foundation, this chapter proceeds to detail a real-time implementation of these approaches. To evaluate their effectiveness, field experiments are conducted in various environments, encompassing both open-sky conditions and agricultural settings. The findings and key insights gained from these experiments are highlighted.

Chapter IV begins by outlining the commonly used approaches for orientation representation. It then investigates the array of sensors employed for orientation estimation, with a primary focus on IMUs. Also, this chapter explores the algorithms frequently employed in conjunction with IMUs. Of particular interest are KFs and CFs. Furthermore, with the advancements in AI-based techniques, notably Neural Networks (NNs), this chapter examines how NNs have been integrated into orientation estimation frameworks and discuss their potential advantages and challenges compared to conventional filtering approaches.

Chapter V starts by evaluating the conventional method employed for tilt compensation in yaw estimation. Subsequently, it introduces a Neural Network (NN)-based solution that utilizes accelerometer and magnetometer measurements as features. Following this, the chapter compares the performance of the proposed solution with that of the conventional tilt compensation method and two established CFs, namely Madgwick and Mahony filters.

Chapter VI serves as the concluding segment of the dissertation, where it provides a summary of the thesis work, highlighting its main contributions. It also recapitulates the results and findings of the thesis. Additionally, the chapter suggests potential directions for future research based on insights gained from this study.

Chapter II

Positioning Systems in Agriculture

II.1 Introduction

For safe and successful navigation, an autonomous agricultural vehicle must be able to know its position in the field. An unreliable positioning could result in the vehicle not being able to perform its tasks successfully, in addition to the likely risk of vehicle-to-vehicle collision. That being said, positioning plays a crucial role in the design of any autonomous vehicle dedicated to agriculture [12].

It is worth mentioning that the terms positioning and localization are often used interchangeably, but are normally used to denote two different concepts. Thus, positioning aims to determine a set of numerical coordinates, while localization constrains the position to a particular area using a map or a geographic information system (GIS) [13].

The agricultural environment introduces unique challenges to vehicles' positioning. Unlike controlled indoor settings, agricultural landscapes present various complexities. These include vast and dispersed operating areas, uneven terrain, significant wheel slippage, and environmental factors like rain, fog, and dust. Moreover, the demand for cost-effective systems in this context further complicates the development of positioning solutions.

Over the years, different positioning solutions dedicated to agriculture applications have been proposed. These solutions may be divided into categories according to the data they generate (motion measurement, local features detection, etc.). This categorization can also be based on the type of reference system into those that generate position with respect to a local reference system and those that are based on an absolute coordinates system independent of local characteristics such as satellite-based positioning systems.

Going through traditional positioning solutions in agriculture, up to the latest techniques and recent research works proposed more recently, this chapter covers some of the early and recent developments in positioning systems of agricultural vehicles. A particular interest is dedicated to satellite-based positioning systems. Furthermore, it's essential to note that our research primarily focuses on outdoor positioning systems.

II.2 Previous Developments

II.2.1 Mechanical-based Systems

Notwithstanding the fact that guidance does not appear in the scope of the proposed work, it was considered essential to present an overview of how previous efforts have addressed this problematic. The first efforts in the field of simplification and automation of agricultural operations aimed to help farmers uniformly space their planted rows. Starting from 1870, several solutions, such as row markers, aids for manual steering and autosteering systems were presented [14].

Undoubtedly, one of the discoveries that shaped modern agriculture was the invention of the agricultural tractor in 1913 with its furrow-following automatic steering aid [14], illustrated in Figure II.1. Subsequently, several mechanical-based works have been proposed to allow precise guidance of these tractors within agricultural fields. All these works can be categorized into two distinct modes; approaches based on existing features and those based on specially provided features.

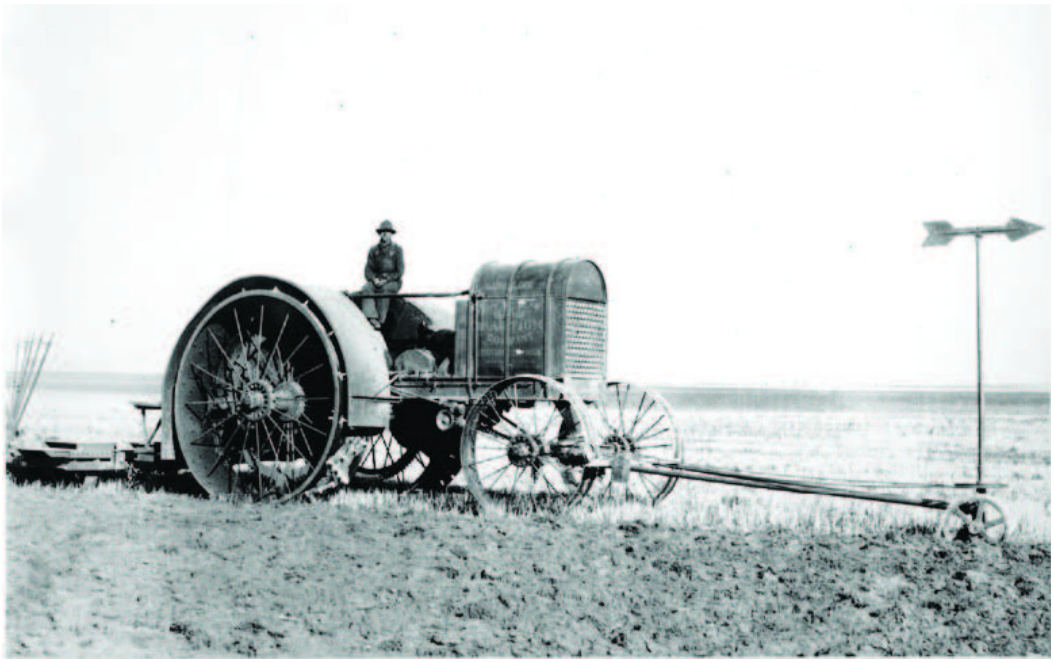


Figure II.1: Agricultural tractor with automated steering system.

As an example of the first mode, we mention the work presented by Kirk et al. [15] where a furrow-engaging device coupled to the steering linkage and placed in front of the tractor's front wheel have been proposed. The work of Wilden and Blair [16] who presented a system based on a cord buried just below the surface serving as markers for guiding tractors is an example of the second mode.

In his review paper [17], Jahns concludes that none of the previously presented techniques could be generalized and that these techniques were not robust enough to meet the needs of agriculture applications. According to Wilson [18], technological developments in several areas including computer vision, and satellite-based positioning systems could lead to the implementation of a universal agricultural guidance system that emulates closely the actions of a human operator.

II.2.2 Odometry Sensors

These sensors are generally used for dead reckoning which is a procedure for determining the actual vehicle position based on previous positions combined with known system's internal information over a given time duration [19]. Odometry sensors are based on the integration of incremental motion information from wheels rotation over time.

On one hand, the simplicity and cost-effectiveness of odometry provide a distinct advantage. On the other hand, the efficiency of these sensors relies strongly on the soil condition. Unfortunately, in the agricultural environment, ground surfaces are usually uneven which makes these sensors highly susceptible to errors resulting from wheel slippage and variation of the track width of the wheels. These errors are cumulative which leads to important positional drift.

II.2.3 Inertial Sensors

In order to avoid the complexity of modeling odometer errors, inertial sensors have been used in a variety of vehicle applications as an alternative to odometers for dead reckoning purposes. Additionally, inertial systems have the benefit of being produced in compact packages that can easily be embedded on vehicles.

They typically consist of accelerometers and gyroscopes. They are often extended by electronic compasses that estimate the orientation of the vehicle relative to the magnetic north. The combination of these sensors gives an estimation of the actual orientation and speed of the vehicle. These latter allow the calculation of the vehicle's current position based on previous positions.

These sensors tend to drift and accumulate errors due to temperature changes, gravity, and exposure to unwanted local magnetic fields. When inertial sensor data are integrated to give speed and position, any small bias in the sensor output will accumulate and result in positional drift. Yet, inertial systems are fairly reliable in the short term [20]. Besides, many research works have led to significant improvement of both robustness and accuracy of these sensors [10].

Another group of sensors used in agricultural vehicles collect environmental information regarding the vehicle's position. This positioning is based on landmarks which are distinct features in the environment that a sensor can recognize. There are two types of landmarks. Natural landmarks are objects or features that are already in the environment and have a function other than vehicle navigation, such as crop rows and crop edges. Artificial landmarks are specially provided objects or markers that need to be placed in the environment with the purpose of enabling positioning [21]. The following sensors are examples of these systems.

II.2.4 Camera-based Sensors

From the 1980s, we have witnessed significant technological developments in the area of image recognition and computers became more powerful, compact and affordable. Thus, the combination of computers along with image sensors provided opportunities for machine vision-based positioning systems [22].

Camera-based systems allow to estimate the relative position and orientation using the image sensor mounted on the vehicle. They are the most suitable sensor for natural landmarks detection and matching [19]. Examples of applications of machine vision-based positioning in agriculture can be found in [23–30]. Unfortunately, unlike industrial applications which deal with relatively simple, well-defined and replicable environments, agricultural applications require advanced technologies to deal with variable factors including lighting, rain, fog, dust and shadowing [20].

In order to extend the detecting range, and overcome the shortcomings of the computer vision-based solutions, a number of works have been proposed where different sensor-fusion strategies, introduced later in this section, have led to a considerable improvement of accuracy as well as robustness.

II.2.5 Laser Scanner Sensors

Several research contributions have been made to the field of positioning using laser scanners [31–35]. This interest is mainly due to the high resolution, large field of view and robust ranging data provided by laser scanners compared to camera-based sensors which give access to a reliable positioning in different weather and illumination conditions [36].

A simple configuration uses three or more artificial landmarks positioned around the field. A vehicle mounted laser is swept in a horizontal plane. by measuring time of flight of laser pulses, relative distances with respect to landmarks are determined and communicated to the positioning system which uses trilateration to calculate to vehicle's position.

This system has the disadvantage of necessitating a communication link between the vehicle and the artificial landmarks [37]. Additionally, One of the major drawbacks of this solution is the noisy laser measurements when the vehicle is traveling on uneven ground [22].

II.2.6 Ultrasonic Sensors

An ultrasonic sensor generates a sound wave in a frequency out of human's audible range (>20KHz). The signal, after being reflected by the target, is recorded by a sensor to estimate the time difference and, consequently, estimate the distance [38]. The use of ultrasonic sensors for navigation and obstacle avoidance for agriculture applications has received much study [39–42].

This interest is motivated by the availability of affordable ultrasonic ranging unit [37]. In outdoor environments, the behavior of natural surfaces differs from indoor reflectors and

has a much smaller amplitude in terms of reflectance. Ultrasonic sensors can be used when accuracy and reliability are not essential because the speed of sound changes due to variations in air temperature and humidity. Thus, they are usually used as complementary sensors which allow to extend their range which is typically less than 10 m.

II.2.7 Discussion

Selection of a sensor should consider range, robustness to lighting condition, robustness to environmental conditions, maintenance, and cost. In [38], a summary of sensors ratings is presented to help select the proper sensor for a specific application. Meanwhile, no single type of sensor has proven to work reliably in all operating conditions and to have clear advantages over the others. It is noteworthy that various recent research studies have suggested combining different systems mentioned earlier [43–45].

Another important aspect to consider is that these early systems and techniques were basically intended to ensure a ground vehicle positioning. Meanwhile, Unmanned Aerial Vehicles (UAVs), commonly referred to as drones, are rapidly replacing ground vehicles, particularly for applications such as efficient crop spraying and field mapping [46]. Yet, most of the positioning sensors mentioned above are impractical for UAVs.

Since the inception of the Global Positioning System (GPS) in the mid-1990s, it was apparent that many of the constraints associated with earlier methods no longer applied to GPS technology. A GPS-based positioning system offers several advantages including high accuracy, particularly in open sky environments, in addition to its affordability and ease of use. Therefore, the use of satellite-based positioning solutions becomes an unavoidable necessity.

II.3 Satellite-based Positioning Systems

All positioning, whether it is relative to a landmark in the environment or to a satellite constellation, can be considered as being relative. Yet, it is important to draw a distinction between positioning techniques that produce a location relative to a nearby reference point and those that produce a location in a geographic coordinates system. Consecutively, the previously exposed methods so far provide relative positioning whereas satellite-based positioning systems provide absolute positioning [19].

The introduction of GPS technology led to extensive research into its applicability for vehicle navigation in agricultural environments [47, 48]. By the early 2000s and with the cancellation of selective availability by the United States Department of Defense [49], several major agricultural equipment manufacturers such as John Deere and Case began offering commercial GPS-based guidance systems, marking the widespread adoption of this technology in various regions across the globe [50].

While GPS triggered the growth of satellite-based positioning systems, it's crucial to acknowledge that other systems have since emerged, including the Global Navigation Satellite System (GLONASS), the European Satellite Navigation System (GALILEO),

China's COMPASS/Bei-Dou, as well as regional systems like India's Regional Navigation Satellite System (IRNSS) and Japan's Quasi-Zenith Satellite System (QZSS) [49].

The general term Global Navigation Satellite Systems (GNSS) has been adopted to embrace the existing satellites constellations. As of the time of this writing, GPS and GLONASS are the only systems that are fully operational [51]. In our work, we opted for GPS primarly due to its widespread adoption and availability.

II.3.1 GPS for Precision Agriculture

Before we explore how GPS is used for positioning in agriculture, we considered important to highlight the significant role that GPS plays in precision agriculture (PA). The emergence of PA and the introduction of GPS are closely related. The availability and expansion of the GPS positioning system were pivotal in inspiring the development of PA techniques. The central concept revolves around the precise application of resources when and where they are required [49].

In fact, GPS technology plays a pivotal role throughout the entire precision agriculture cycle as illustrated in Figure II.2. This latter is consists of four primary stages: data collection, analysis and planning, field operations, and yield monitoring [52].

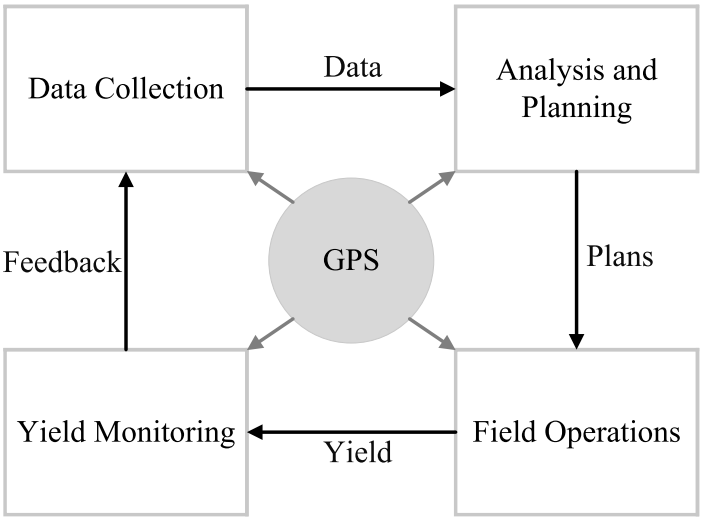


Figure II.2: Role of GPS in the precision agriculture cycle.

During the dataset collection phase, GPS data allows to create precise field maps. These maps are invaluable for planning and providing in-field GPS guidance for agricultural vehicles. Subsequently, employing suitable sensors, a contour map is generated. This map allows to define homogeneous zones in order to develop customized management strategies for each of these zones [53].

For the analysis and planning phase, and considering the variable rate application (VRA) which is a widespread practice in PA, the data collected provides the basis for creating prescription maps for VRA of fertilizer, seed, and chemicals. Guided by GPS data, these maps suggest different input quantities for various zones, taking into account soil characteristics [54].

The use of GPS technology has led to the development of guidance systems that help different types of vehicles to follow predefined tracks and avoiding geofences. Accurate field navigation reduces redundant applications and skipped areas, allowing for optimal ground coverage in the shortest time possible. As the vehicle moves through the field, and based on its actual position within the prescription map, VRA equipment changes the concentration of the input [55].

Yield monitoring is conducted using yield monitors that are attached to harvesting machines. These monitors assess yields in various zones across the field. Through post-processing, farmers can evaluate the effects of the applied technology and use this data to make informed decisions for optimizing future farming processes [53].

II.3.2 GPS Overview

II.3.2.1 GPS Segments

GPS consists of three segments: the space segment, the control segment, and the user segment.

II.3.2.1.1 Space segment The space segment comprises a constellation of satellites that transmit radio signals to users. These satellites are equipped with highly accurate atomic clocks. They transmit pseudorandom noise (PRN)-coded signals, from which the ranging measurements are made. This concept defines GPS as a passive system with signals only being transmitted and the user receiving the signals. Consequently, an unlimited number of users can simultaneously use GPS [7].

As of July 2023, there were a total of 31 medium-Earth orbiting (MEO) operational satellites in the GPS constellation at an altitude of approximately 20,200 km. The GPS constellation is a combination of older and newer satellites, comprising the following generations: Block IIR (6 operational satellites), Block IIR-M (7 operational satellites), Block IIF (12 operational satellites), and GPS III/IIIF (6 operational satellites) [56].

The satellites are arranged into six orbital planes with 4 evenly-spaced satellites per plane. This 24-slot arrangement ensures that a minimum of four satellites can be visible from virtually any point on the planet at any given time. The additional satellites may enhance the performance of GPS but are not regarded as part of the primary constellation [56].

II.3.2.1.2 Control segment The control segment of the GPS system is composed of a global network of ground stations responsible for tracking the GPS satellites. Its main functions include monitoring the health of the satellites by resolving anomalies, managing their orbital and clock errors, and monitoring all satellite navigation signals. To accomplish this, the control segment uploads commands and data into the GPS constellation via the S-band link, ensuring this is performed at least once per day [57].

The current control segment is comprised of 16 monitoring sites and 11 command and control antennas, all under the management of a master control station and an alternate master control station both located in the United States, with one in Colorado and the other in California, respectively [58].

II.3.2.1.3 User segment The user segment includes all GPS receivers responsible for processing the signals transmitted by GPS satellites to determine the user's position, velocity, and precise time (PVT). This process involves detecting, demodulating, and separating the received signals into their individual components.

To achieve this, GPS receivers typically consist of several key components, including an antenna, filtering and downconversion components, an internal oscillator, digital signal processors, and a navigation processor [7].

II.3.2.2 GPS working principle

GPS positioning works on the basis of a mathematical concept called trilateration, as depicted in Figure II.3. The underlying idea is straightforward: to determine a user's position on Earth (R), it is necessary to know the locations of a minimum of three GPS satellites (P1, P2 and P3) and the distances from those satellites to the user's position (D1, D2 and D3).

Unlike conventional trilateration, GPS positioning actually involves four intersecting lines at the unknown point, which is necessary because there are four unknowns: X, Y, Z, and time.

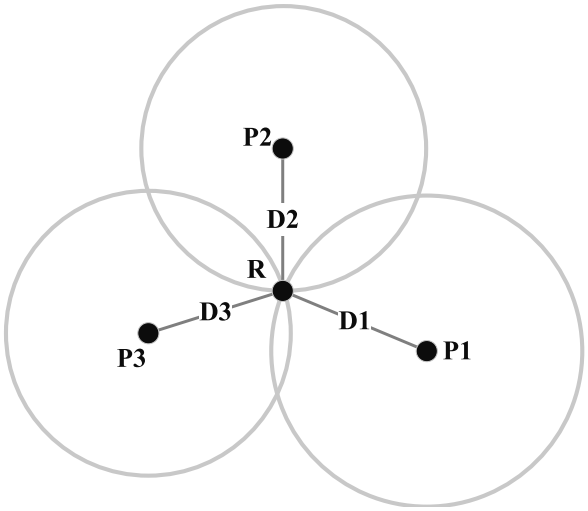


Figure II.3: Trilateration principle.

Hence, determining the position of a GPS receiver relies on having access to two crucial pieces of information: the satellites' positions and the distances between the receiver and these satellites. As previously noted, GPS operates as a passive system, relying solely on the received GPS signals as its primary source of information.

II.3.2.3 GPS Signal

II.3.2.3.1 GPS Signal Interface The atomic clocks of a satellite produce a sine wave with a fundamental frequency f_0 of 10.23 MHz. This fundamental frequency is used to generate the three carrier waves frequencies via multiplication by 154, 120 and 115, denoted respectively L1(1575.42MHz), L2(1227.60MHz) and L3(1176.45MHz).

Thus, the signal interface between the space segment and the user segment comprises three distinct radio frequency links. The L5 link is only available on Block IIF and the subsequent generations of satellites [59], as depicted in Figure II.4.

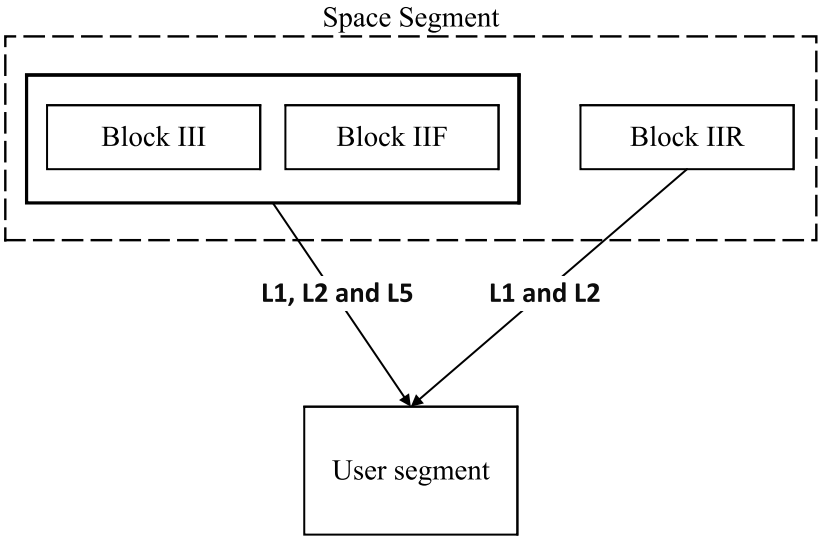


Figure II.4: GPS signal interface definition.

The focus of this research lies strictly with single frequency GPS receivers. Consequently, the signals of interest revolve around the different codes employed to modulate the L1 frequency.

II.3.2.3.2 GPS L1 Signal Structure The GPS L1 frequency is currently the most employed band for navigation purposes, with the majority of applications worldwide relying on signals transmitted at this specific frequency [60].

The L1 signal encompasses ranging codes, employed for determining the distance to the satellite, and navigation messages containing crucial information essential for GPS receivers. This information primarily includes the transmission time of each satellite signal, the precise position of the satellite at the moment of transmission and atmospheric parameter information [61].

GPS Ranging codes Ranging codes are pre-defined repeating pseudorandom noise (PRN) codes. They consist of binary sequences which appear to be noise, but they are actually capable of repetition and correlation. PRN codes serve as the distinct signatures of GPS signals, as two different PRN codes exhibit no correlation. This characteristic allows receivers to distinguish GPS signals originating from different satellites [62].

In addition to the newly introduced L1C code and M-code , two primary ranging codes are transmitted at the moment by GPS using L1 frequency:

- *Coarse/Acquisition (C/A) code* : Each C/A code has a length of 1023 bits, repeated every millisecond. The C/A code for each satellite is a 1 kHz signal made up of continuously repeating PRN sequences over time which modulate the L1 carrier wave at a rate of 1.023 MHz to form a ranging signal using a Bi-Phase Shift Key (BPSK) modulation technique [62].

- *The Precision P(Y)-code*: P-code is the principal military ranging code, while the Y-code is used whenever the anti-spoofing mode is activated [63]. It is transmitted as a 10.23 MHz signal using the same BPSK modulation, however the P(Y)-code carrier is in quadrature with the C/A carrier.

It is worth mentioning that GPS can provide two distinct positioning services [63]:

- *The Standard Positioning Service (SPS)*, available on GPS L1, L2, and L5 frequencies, offers positioning and timing services for peaceful civil, commercial, and scientific use worldwide. The code associated with this service is the C/A code.
- *The Precise Positioning Service (PPS)* is a highly accurate service broadcasted on the GPS L1 and L2 frequencies. Reserved exclusively for authorized users, this service utilizes the P(Y)-code. In our work, we will not be utilizing this service due to its restricted access.

GPS Navigation Messages Today, GPS satellites transmit several navigation messages, but our focus will be on the one designated for SPS, specifically, the legacy Navigation (LNAV) message. This message encompasses details such as the ephemeris, which indicates the location of the GPS satellites, and clock corrections, essential for time conversions and offsets.

Additionally, the LNAV message communicates vital information about the satellites' health in orbit and details regarding the ionosphere. It incorporates almanacs, a set of data providing a GPS receiver with sufficient information to estimate the coordinates of all satellites within the constellation [64].

The complete LNAV message comprises 25 frames, each spanning 1500 bits and further divided into five subframes. Within each subframe, there are 10 words, and each word is composed of 30 bits. Consequently, the overall LNAV message consists of 37,500 bits and is transmitted at a rate of 50 bits per second, requiring 12.5 minutes for complete broadcast [62].

The LNAV message undergoes modulo-2 addition with the P(Y) and C/A codes, and the resulting values are utilized to modulate the L1 signal, as illustrated in Figure II.5.

II.3.2.4 GPS Measurement Observables

In GPS literature, the term 'observable' is employed to denote the signals that, when measured, provide information about the range between the satellite and the receiver. This term serves to distinguish the object being measured, referred to as "the observable," from the actual measurements.

Indeed, the only measurements carried out by a GPS receiver involve determining the time shift necessary for aligning the received and locally generated PRN codes. Additionally, the receiver measures the frequency shift required to maintain synchronization between the received and the locally generated carrier wave [57].

The measurement observables produced by a GPS receiver originate directly from these two observations, encompassing a set of three distinct values: pseudorange, carrier phase, and Doppler shift.

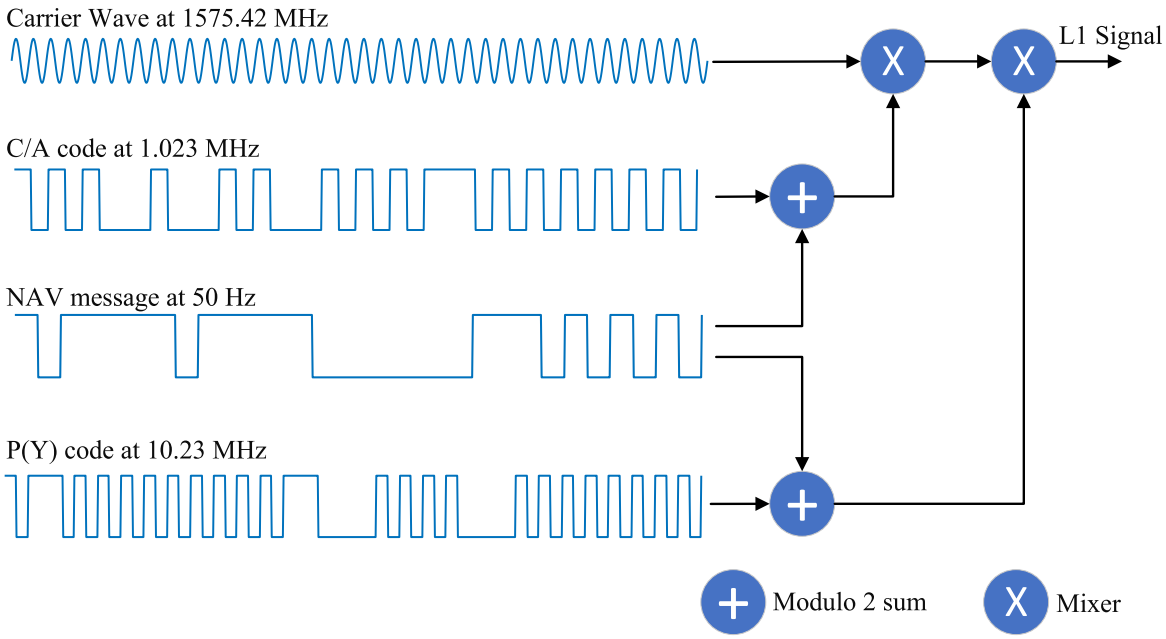


Figure II.5: GPS L1 signal composition.

II.3.2.4.1 Pseudorange Pseudorange represents a measure of the distance between the satellite and the GPS receiver on the Earth. The measured pseudorange deviates from the actual distance due to clock errors and the impact of signal transmission mediums, hence the use of 'pseudo' in its designation.

It is calculated by measuring the time-of-flight (TOF) of the transmitted GPS signal and multiplying it by the propagation speed of the radio signal which equals the speed of light.

The transmit moment is known as it is included in the navigation message. However, the reception time relies on inaccurate local receiver's clock, introducing complexity in measuring pseudorange. This complexity arises from the need to synchronize the receiver's clock to GPS time with precision in order to enable accurate measurement of TOF [7].

The core of estimating reception time involves correlating the code carried on the modulated carrier wave received from a GPS satellite with a replica of that identical code generated in the receiver [57].

Referring to Figure II.6, extracted from [7], we observe the distinction between the actual geometric range and the measured pseudorange, specifically considering the influence of unsynchronized clocks, where:

- T_s is the actual GPS time when the signal was transmitted from the satellite;
- T_u is the actual GPS time when the signal, free from errors, would have reached the receiver;
- Δt is the theoretical TOF of the transmitted GPS signal;
- δt is the satellite clock offset from GPS time;
- t_u is the receiver clock offset from GPS time;

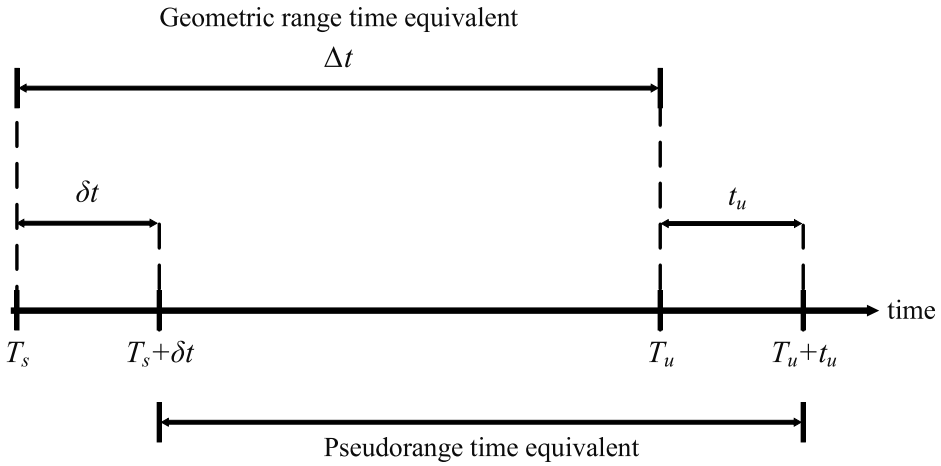


Figure II.6: Pseudorange measurement timing relationships.

.

That being said, The geometric range r and the pseudorange ρ are expressed by relation II.1 where c is the speed of light.

$$\begin{aligned} r &= c(T_u - T - s) = C\Delta t \\ \rho &= c[(T_u + t_u) - (T_s + \delta t)] = r + c(t_u - \delta t) \end{aligned} \tag{II.1}$$

It is important to highlight that this formula presents a generalized model for pseudorange, overlooking other errors like atmospheric delay. in the upcoming chapter, we will present a comprehensive examination of all the known factors that influence the accuracy of pseudorange measurement.

While our work does not directly involve the utilization of carrier phase and Doppler shift, we find it crucial to provide a brief overview of them for a more comprehensive understanding of existing GPS positioning methodologies.

II.3.2.4.2 Carrier phase Pseudorange is commonly used in applications where relatively lower accuracy is acceptable or instant positions are required. In contrast, carrier phase serves as the foundation for techniques employed in high-precision GPS surveys. Nevertheless, many GPS receivers utilize the pseudorange as an initial step to initiate position determination before switching to carrier phase observable in order to refine the obtained position [62].

The carrier phase represents a measure of the phase between the received satellite carrier signal and the receiver's locally generated carrier wave at the reception time. In other words, it is the number of carrier cycles that exists between a satellite and a receiver.

The fractional phase can be measured precisely with precision better than 1% of the wavelength (Theoretically 1.91 mm for L1 carrier wave). Meanwhile the number of carrier cycles includes also an integer carrier cycles term known as Integer Ambiguity which needs to be determined [65].

Once the integer ambiguity terms for the available set of satellites are resolved, the phase measurements can be converted into highly accurate receiver-to-satellite range measurements. Unfortunately, not all GPS receivers can utilize carrier phase for position determination and this feature is not available for consumer-grade GPS receivers.

II.3.2.4.3 Doppler shift Similar to carrier phase, this observable is derived directly from the GPS carrier signal rather than TOF measurements. Doppler shift is a well-known phenomenon that affects the frequency of traveling wavefronts when two objects are in motion at varying speeds relative to each other.

In this case, a radio signal transmitted from a satellite in motion at a nominal frequency will be received at the receiver with a slightly different frequency. This difference in frequency is employed as supporting data for determining both position and velocity. Furthermore, Doppler shift measurement play a crucial role in detecting and correcting cycle slips in positioning solutions based on carrier phase [65].

II.3.2.5 GPS Augmentation Systems

There are two main categories of GPS receivers: single-frequency and multi-frequency. While multi-frequency GPS receivers offer centimeter-level accuracy with suitable positioning techniques, their cost is several thousand US dollars, making them inaccessible for many farmers [5].

In contrast, single-frequency GPS receivers are more affordable, leading to significant efforts to enhance their accuracy through various augmentation systems, driven in part by the accessible prices of these receivers. The most representative augmentation systems are the Differential GPS (DGPS) services in addition to the various multi-sensor fusion approaches [7].

II.3.2.5.1 DGPS Services The widespread adoption of GPS technology in agriculture has markedly increased, primarily driven by improved accessibility to differential correction services. They are divided into two types depending upon the size of the geographic area covered by the DGPS system.

Wide-Area DGPS (WADGPS) WADGPS services play a pivotal role in enhancing the accuracy of GPS-based positioning across large geographic areas. These services include a network of reference stations with precisely known locations, each equipped with high-quality GPS receivers. By comparing the signals received at these reference stations with the known locations, errors affecting the signals can be identified and quantified.

The gathered correction information is then transmitted to users, enabling them to refine their GPS position estimates. This correction data, often transmitted through satellite communication, and known as Satellite-Based Augmentation Systems (SBAS), helps mitigate errors arising from factors like atmospheric delays and satellite clock errors.

An SBAS is a WADGPS system that provides differential GPS corrections using geostationary satellites. It provides corrections data through a signal directly broadcast at the GPS L1 frequency. Examples of SBAS implementations include systems like the Wide Area Augmentation System (WAAS) within the United States, the European Geostationary Navigation Overlay Service (EGNOS) within Europe and the Multifunctional Transport Satellite (MTSAT)-based Augmentation System within Japan and Southeast Asia. Unfortunately, the existing WADGPS so far are regional services and do not cover zones in Africa and South America [8].

Local-Area DGPS (LADGPS) In the LADGPS system, a reference base with known coordinates measures the distance to visible GPS satellites in real-time. Using its precise coordinates, the base calculates the expected distance without error. The difference between the expected and measured distances for each satellite is sent to the receiver, helping determine its position through a radio link.

Corrections can be applied through post-processing methods or in real-time. In the case of real-time corrections, it is referred to as Real-Time Kinematic (RTK) GPS [66]. RTK systems offer the highest accuracy in GPS applications, yielding typical errors of less than 2 cm. However, a drawback is that they necessitate a base station within a 10 km range, limiting their suitability for large farms.

It is worth mentioning that in different parts of the world, LADGPS services are uncommon because they rely on large-scale infrastructures or on specific hardware support, some of which are not generally accessible or are expensive [67].

II.3.2.5.2 Integrating GPS with other sensors To ensure continuous positioning information during GPS signal blockage, periods of interference, and between receiver update intervals, several solutions have been proposed. These solutions involve integrating GPS receivers with various additional sensors. While our intention is not to provide a full review of all existing approaches, we will highlight some of the noteworthy ones.

The majority of current multi-sensor fusion techniques rely on Kalman filtering procedures, recognized as one of the optimal solutions for integrating multiple sensors. A Kalman filter is a linear, model-based estimator that employs stochastic, recursive, weighted, and least squares computing algorithms [36].

One of the well-known approaches based on multi-sensor fusion is the Simultaneous localization and mapping (SLAM). It consists of estimating the current position of a moving vehicle, while simultaneously building a map of the surrounding environment based on sensors such as acoustic sensor, RADAR, camera, Light Detection and Ranging (LiDAR) [68].

Another instance is a sensor fusion approach designed for steep slope vineyards, combining GPS, wheel odometry, and previously marked landmarks [69]. Iqbal et al. also proposed a similar fusion in their work, integrating GPS, 2D laser, and an IMU [70].

Bietresato et al. presented a fusion technique incorporating sonar, IMU, and RTK GPS for vegetation mapping [71]. In a different application, a study suggested the fusion of a monocular camera and a GPS module for in-row weed control [72].

Lastly, Ampatzidis et al. introduced an innovative strategy utilizing radio frequency identification (RFID) for yield mapping [73]. This involved attaching RFID tags to trees and using a reader mounted on a vehicle to identify and navigate between them.

II.3.2.6 GPS-based Relative Positioning

Many studies and researches have proven the spatial and time correlation of most of the GPS pseudorange measurement errors [7]. As a result, and in order to eliminate or reduce the majority of quantifiable errors included in pseudorange measurement, a common technique known as differencing is usually performed.

Differencing serves two primary purposes. The first, known as "Absolute differential positioning" involves improving a receiver's position with respect to an Earth-Centered Earth-Fixed coordinate frame. The second objective, termed "Relative differential positioning," aims to accurately determine a receiver's position relative to a local coordinate system attached to another receiver.

Absolute differential positioning relies on a precisely known reference station, using its known position to compute corrections on GPS measurements. These corrections are then transmitted and applied to mobile GPS receivers, resulting in an improved absolute position. This principle aligns with the approach employed by LADGPS services.

Relative differential positioning, abbreviated as relative positioning in the rest of this thesis, aims to determine the vector between two receivers, commonly referred to as the baseline vector. The positions of these receivers don't necessarily need to be known and may be time-varying. In relative positioning, a minimum of two receivers is involved. In a base-rover configuration, the base assumes a known position, and the goal is to determine the position of the other receiver, the rover, with respect to the base.

Assume one GPS receiver is installed in a known position in the vicinity of an agricultural field. Being able to locate accurately other mobile vehicles equipped with GPS receivers with respect to the static receiver permits to determine their real positions within the agricultural field as shown in Figure II.7. Moreover, the knowledge of relative positions between different moving vehicles is primordial and allow to avoid collisions and optimally divide work tasks.

Consecutively, in the initial phase of our work, we intend to investigate the feasibility of employing different GPS-based relative positioning approaches for agriculture applications. Rather than improving the accuracy of GPS receivers related to an ECEF coordinate frame, the proposed work seeks to enhance positioning accuracy with respect to a local coordinate frame attached to one of the GPS receivers.

II.4 Conclusion

In conclusion, this chapter initiated by surveying various positioning solutions in agriculture, revealing that early systems lacked the needed technical and economic suitability for widespread use in the field.

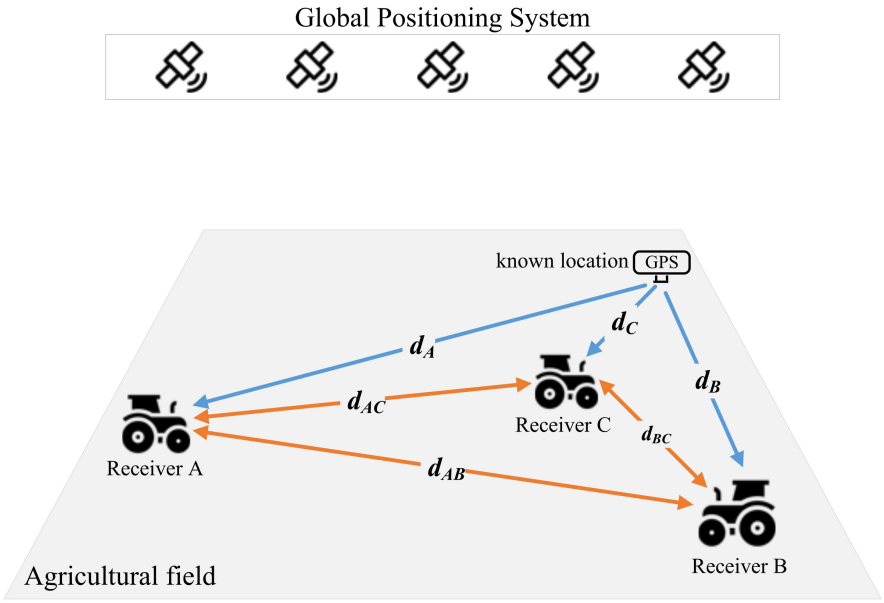


Figure II.7: Pictorial representation of the use of GPS-based relative positioning for agriculture applications.

With the advent of GPS, a pivotal advancement emerged in agricultural applications. This chapter discussed the vital role of GPS in agriculture, providing an overview of the GPS system, its working principle, in addition to the various GPS measurement observables. Augmentation systems for GPS were also introduced in order to enhance customer-grade GPS receivers positioning accuracy.

Finally, we presented a brief overview of the GPS-based relative positioning, emphasizing our aim to evaluate the opportunity of using it in agriculture. The following chapter will provide a detailed examination of GPS-based relative positioning, where we propose to implement various real-time approaches in order to assess its viability for agriculture applications.

Chapter III

Experimental Evaluation of GPS-Based Relative Positioning Approaches for Agriculture Applications

III.1 Introduction

In this chapter, we shift the focus from traditional absolute positioning systems in agriculture to explore the potential of relative positioning. Our goal is to assess the practicality and effectiveness of several GPS-based relative positioning methods. Using affordable modules, we implement these approaches in real-time, making them more accessible for agricultural applications.

To assess their performance, we conduct field experiments in different settings, including an open-sky environment and an agricultural field. The results and insights gained from these experiments are the main highlights of this chapter. We aim to offer a clearer understanding of how relative positioning approaches can be valuable and cost-effective in addressing the specific needs of positioning in agriculture applications.

III.2 Motivation

In parts of the world where traditional farming methods predominate, access to cost-effective positioning technology can revolutionize agricultural practices, empowering farmers with valuable information enabling them to optimize resource management, such as precise application of fertilizers and water, resulting in increased crop yields.

While multi-frequency GPS receivers offer centimeter-level accuracy, they are also very expensive, costing several thousand US dollars and remain out of reach for many farmers [5]. As the low-cost single-frequency GPS receivers dominate most of the GPS market, mainly

due to their lower price, many efforts have been put into improving their accuracy, typically up to tens of meters, through different types of augmentation systems [6].

The primary augmentation systems are Differential GPS (DGPS) services, commonly categorized into wide-area DGPS services (WADGPS) and local-area DGPS services (LADGPS), as explained in section II.3.2.5.1. Unfortunately, current WADGPS services, especially satellite-based (SBAS) ones, are regional and do not extend coverage to areas in Africa and South America, as shown in Figure III.1, sourced from [8].

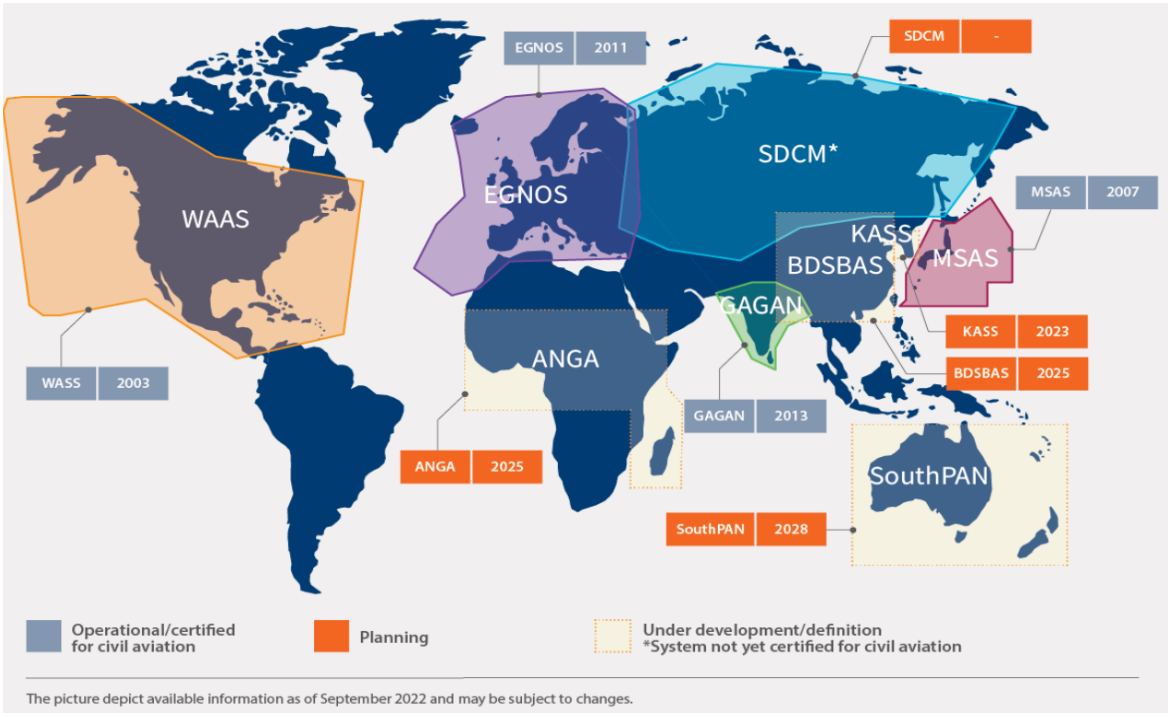


Figure III.1: SBAS service areas

On the other hand, in different parts of the world, LADGPS services are uncommon due to their dependence on large-scale infrastructures or specific hardware devices support, some of which may not be generally available or are costly. A LADGPS solution, suitable for tasks like yield monitoring and soil sampling, typically costs between 3,000 and 5,000 US dollars, offering a Root Mean Square (RMS) accuracy of at least three meters, with a standard accuracy of around one meter.

Given the absence of augmentation systems in different regions in the world and considering that the capacity of standalone GPS receivers to reach high levels of accuracy is proportional to their cost, relative positioning emerges as an alternative for accurate positioning purposes in agriculture applications. Consecutively, in this chapter we intend to implement and evaluate different GPS-based relative positioning approaches for agriculture applications based on low-cost single-frequency GPS receivers.

III.3 Literature Review and Contribution

III.3.1 Literature Review

In many applications a relative position with respect to a local coordinate system may be sufficient. Relative positioning has been used in different fields such as intelligent transportation systems (ITS) and unmanned aerial vehicle (UAV) swarms. In order to measure distance between two vehicles, different methods exist in the literature. The most common approach is to use radio ranging methods such as Received Signal Strength (RSS), Time Of Arrival (TOA), and Time Difference of Arrival (TDOA) techniques [74]. Other techniques using laser and stereo vision camera have also been proposed [75]. In spite of the high levels of accuracy offered by these techniques, their major drawback is certainly the limitation in their perception range. Hence, there have been a significant number of researches devoted to GNSS-based relative positioning.

One study that has addressed the problematic of measuring distances between GPS receivers by sharing pseudorange measurements is the research conducted by Yang et al. They employed the weighted least squares method to implement a Pseudorange Double Differencing (PDD) algorithm, which significantly reduced the average distance error from 12 meters associated with standard GPS fixes to approximately 3 meters [76]. Another approach comes from Alam et al., who suggested replacing traditional radio ranging techniques in relative positioning for a Vehicular Ad Hoc Network (VANET) with GPS measurements. Their focus was specifically on the exchange of GPS measurements among moving neighboring vehicles based on a standardized communication medium [77].

To improve the accuracy of relative positioning, some research groups have focused on the study of the properties of GNSS measurement errors and their effects on relative positioning accuracy. A zero-baseline experiment, which consists in feeding two GNSS receivers with the same signal received by one common antenna, was conducted in order to assess the impact of uncorrelated errors, such as noise and multipath [78].

Likewise, Trigos et al. conducted a similar study, examining various ionospheric correction models to identify conditions that could enhance relative position accuracy [79]. Another investigation delved into the Sagnac effect and its induced errors using a network of Android phones [80].

Among the works found in this field, the research of Müller et al. is highlighted. This work has explored the feasibility of using GNSS-based cooperative relative positioning for safety vehicular applications. Two strategies have been evaluated; one uses absolute positions whereas the second exploits GNSS pseudorange measurements. Further on, two probabilistic approaches were proposed; one uses only measurements from GNSS receivers while the second additionally requires the use of inertial and speed sensors. Real world experiments have shown that the sensor fusion approach gives good results especially in GNSS challenging environments [81].

In the same context, other multi-sensor approaches that use GNSS receivers along with other sensors in order to estimate relative positions have been proposed. Shen et al. proposed to combine GNSS pseudorange double differences with peer-to-peer ranging measurements for multi-UAV formation flight. Simulations and flight experiments have revealed significant

improvement in both accuracy and robustness [82]. In the work of Lassoued et al., GNSS and dead reckoning measurements were used to implement a data fusion algorithm intended for vehicular applications. This latter requires the use of additional sensors to measure the vehicle's yaw angle and speed [83].

Other studies investigated the use of GPS-based relative positioning in ITS applications. As an example, Liu et al. have proposed a ranging technique between vehicles based on GPS pseudorange differencing while taking into consideration the signal to noise ratio (SNR) of each pseudorange measurement [84]. Tang et al. have proposed an experimental evaluation of GPS-based relative positioning for ITS through recording and analyzing the properties of pseudorange measurement provided by cars driving in urban areas [85].

In their investigation, Tahir et al. not only assessed the Absolute Positioning Differencing (APD), Pseudorange Single Differencing (PSD), and PDD approaches but also explored an alternative GNSS-based ranging technique. They introduced a method that employs raw pseudoranges (PR) without any differencing between pseudorange measurements. The research results indicate that this proposed method outperforms other techniques, particularly in scenarios characterized by a prominent multipath phenomenon [86].

Minetto et al. introduced a novel GNSS-based ranging technique known as Inter-Agent Ranging (IAR). This approach involves both pseudorange measurements and the terms derived from the Direction Cosine Matrix (DCM), computed using the Position Time Velocity (PVT) algorithm. With a reduced need for shared GNSS observables, the IAR method effectively decreases the volume of transmitted data and computational complexity, as highlighted in their study [87].

Havyarimana et al. introduced a method designed to estimate inter-vehicle distances using the PDD approach, taking into account various measurement attributes, including the SNR of pseudorange measurements, position dilution of precision (PDOP), and the number of common satellites between GNSS receivers. Furthermore, the study explores the potential of a probabilistic approach by treating the uncommon noise associated with pseudorange measurements as a non-Gaussian distribution [88].

In recent years, the notion of social distance has been adopted to fight the transmission of SARS-CoV-2. Minetto et al. proposed to use the APD, PSD and IAR approaches to compute interpersonal distance in outdoor environments through the exchange of raw data delivered by GNSS receivers which are nowadays integrated into vehicles, smartphones and smartwatches. Notably, the IAR approach emerged as a complementary or alternative technique to other approaches in situations where there is a restricted number of common satellites available for computation [89].

Moreover, notwithstanding the exclusion of carrier phase measurements in the context of this study, it is worth mentioning that several relative positioning approaches based on carrier phase have been proposed [90, 91].

The examined literature has introduced diverse methodologies for determining the relative position between two distinct GNSS receivers. These methods fall into four primary categories depending on the type of exchanged data: absolute position-based, pseudorange-based, carrier phase-based, and multi-sensor fusion-based approaches. Beyond these approaches, numerous studies have explored the influence of GNSS errors on the accuracy of relative positioning.

III.3.2 Contribution

While previous research efforts have primarily focused on developing and evaluating relative positioning techniques for various applications, there seems to be a lack of studies exploring the potential of using relative positioning specifically for agriculture applications in the current literature. In light of this, the present study aims to introduce GPS-based relative positioning into the domain of agriculture.

In line with the prior works, our research aims to implement and evaluate three distinct approaches, namely APD, PSD and PDD approaches, which have been drawn from the existing literature. A block diagram that describes the used methods is shown in Figure III.2.

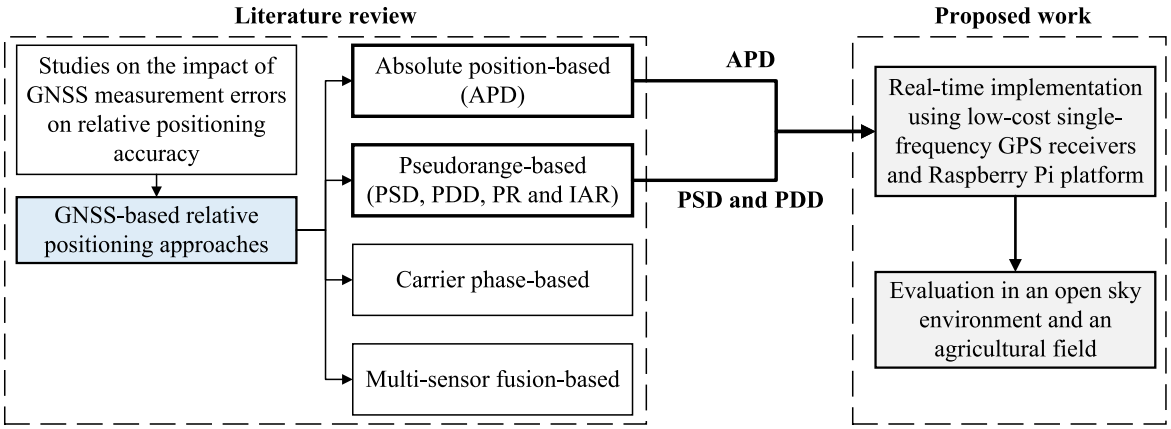


Figure III.2: A block diagram that shows the used methods

The main contributions of our study are summarized as follows:

- First, it proposes to implement different relative positioning approaches based on the use of low-cost single-frequency GPS receivers. These approaches are implemented in real-time through the use of radio frequency transceivers.
- Second, the proposed work has the originality to evaluate the potential of using these relative positioning methods for agricultural applications by conducting experiments in an open sky environment and an agricultural field.

III.4 GPS Error Sources and Pseudorange Model

Determining the range between satellites and the receiver is a crucial operation in GPS-based relative positioning, as it forms the foundation for accurate baseline calculations. In order to measure this range, there are two types of GPS observables; pseudorange and carrier phase, as presented in section II.3.2.4.

Carrier phase is the measured range between a satellite and a receiver expressed in units of carrier cycles. While this measurement offers high precision, there is an ambiguity in the number of whole carrier cycles, requiring resolution [67]. A number of researches have shown

that the resolution of this ambiguity for relative positioning usage is time consuming and computationally heavy [92,93].

On the other hand, pseudorange, directly derived from the estimated travel time of the signal from the satellite to the receiver, offers a straightforward solution for relative positioning [94, 95]. Consequently, our work exclusively focuses on the utilization of pseudorange.

III.4.1 GPS Error Sources

Pseudorange is determined by multiplying the travel time of the signal by its propagation speed, which, in this case, equals the speed of light. However, each GPS pseudorange measurement is susceptible to various sources of error that impact its precision [7]. Hence, comprehending these error sources is crucial for minimizing them to the best extent possible. The following outlines the primary known sources of error affecting pseudorange measurements:

III.4.1.1 Satellite Clock Error

Given the absence of direct communication between satellites, ensuring precise alignment of the clocks on all satellites with a reference time is crucial. This alignment is achieved by synchronizing the highly accurate atomic clocks on each satellite with a designated 'GPS time' directly correlated with Coordinated Universal Time (UTC), to which our Earth clocks are also synchronized.

The control segment guarantees this synchronization by providing clock correction information, which is utilized to align the satellite time with the GPS time, and this correction is subsequently rebroadcast in the GPS navigation message. Note that the time on the satellite clocks is permitted to vary within a tolerable range before synchronization corrections are sent. Typically, these corrections are transmitted to each satellite at least once per day [57].

Failure to apply clock corrections in a GPS receiver can lead to a significant error in pseudorange measurements. The magnitude of clock correction can be nearly 1 ms, resulting in a pseudorange error of up to 300 km. However, when receivers incorporate the satellite clock corrections, the pseudorange measurement error is generally limited to several meters [7].

III.4.1.2 Receiver Clock Error

Similar to GPS satellite clocks, the internal clock within each GPS receiver is susceptible to deviation from GPS time. Meanwhile, and in opposition to satellites, GPS receivers rely on low-cost internal oscillators compared to the highly accurate atomic clocks used on board satellites. This makes the deviation from GPS time much larger and change more rapidly.

The receiver clock error can reach ± 1 ms, resulting in a pseudorange measurement error ranging from -300 km to +300 km [57].

Because this deviation is both large and changes rapidly, it is commonly dealt with through estimation in the positioning process for each GPS receiver. This is possible because it is the same across all satellites, so it can be represented by a single unknown parameter, along with the X, Y, and Z coordinates. The requirement to address this error is why having a fourth satellite is essential in GPS positioning.

III.4.1.3 Atmospheric Errors

After a GPS signal leaves the satellite antenna, it travels through a range of mediums. The primary and most significant segment of this journey occurs through space, where the signal maintains its initial characteristics. At an altitude of about 1,000 km, the GPS signal enters the ionospheric layer which contains various gases that are easily ionized by the sun's radiation. This layer modifies the signal propagation speed and causes an apparent delay in the signal transmit from satellites and receivers.

It's important to consider that the delay experienced by a radio wave in the ionosphere is directly proportional to the time it spends within it. Therefore, ionospheric delay depends not only on the entry point of the signal into the ionosphere but also on the satellite's elevation with respect to the receiver. In practical terms, errors on signals from satellites at low elevations are nearly three times greater than errors on signals arriving directly above the receiver [80].

Every satellite broadcasts ionospheric correction parameters intended for the receiver, capable of reducing ionospheric errors by approximately 50%. Without correction, ionospheric delay can lead to errors ranging from 3-9 meters at night and 15-45 meters during the day.

The troposphere, another atmospheric layer that induces delay in GPS signals, is a refractive layer spanning approximately 8 km to about 50 km above the Earth's surface. Composed predominantly of dry gases and water vapor, the delay is attributed to the index of refraction, influenced by local temperature, pressure, and relative humidity. Tropospheric errors can vary from 2.4 meters for signals arriving directly above the receiver to 25 meters for satellites positioned about 5 degrees above the horizon [65].

III.4.1.4 Ephemeris Error

For determining a receiver's position, it is necessary to have knowledge of the positions of the utilized satellites, which are time-dependent. The control segment predicts and periodically transmits satellite orbital information, referred to as ephemeris. However, these predicted orbital details may not account for all factors affecting satellite movement, such as solar radiation pressure and gravitational forces. Consequently, this omission can introduce an error ranging from 2 to 5 meters in the estimated positions of the satellites [67].

III.4.1.5 Multipath Error

One of the most challenging errors in GPS receiver measurements, often difficult to rectify, is due to a phenomenon known as multipath. Multipath is the reception of one or multiple replicas of the desired signal. Due to reflection caused by surrounding objects or even the ground, the GPS receiver may receive delayed versions of the original signal which could result in an interruption of signal tracking or significant errors in the pseudorange measurement.

As long as the signal reflections arrive after a time greater than the PRN code period, the receiver can identify and discard the erroneous signals, since it is already tracking the accurate direct signal. However, if the reflected signals arrive with short delays (tens or hundreds of nanoseconds), they can distort the autocorrelation between the received signal and the locally generated one, leading to unpredictable errors in the pseudorange measurement [7].

III.4.1.6 Non-Modeled Errors

The category of non-modeled errors in pseudorange measurement involves a range of uncorrelated error sources. They encapsulate various factors related to receiver measurement noise, comprising receiver thermal noise and interference effects. Receiver thermal noise, generated by the internal components of the receiver, contributes to the overall noise level in the measurement. Simultaneously, interference effects, arising from external signals or electronic devices, introduce additional fluctuations.

III.4.2 GPS Pseudorange Model

Consecutively, and by assigning geometric error contributions to each of the previously discussed error sources, a pseudorange measurement ρ_k^a, between receiver k and satellite a, can be defined using relation III.1 [76]:

$$\rho_k^a = r_k^a + \varepsilon_k + e^a + \delta_k^a \tag{III.1}$$

where,

- Subscript refers to an individual receiver and superscript corresponds to an individual satellite;
- r_k^a represents the true range between receiver k and satellite a;
- ε_k is the bias caused by receiver k clock error;
- e^a is the bias associated to satellite a. It encompasses errors related to ephemeris, satellite clock and atmosphere effects;
- δ_k^a is the bias specific to satellite a and receiver k. It includes multipath errors, receiver noise and other residual errors.

It should be pointed out that errors related to atmosphere effects are not dependent on a specific receiver as long as receivers are located in the same region (with a baseline up to 1000 km in ideal conditions) [80].

III.5 GPS-based Relative Positioning Approaches

In our work, we consider a simple situation where we propose to determine the baseline between two receivers. The proposed approaches can easily be adapted for the case of more than two receivers. By definition, the baseline length between two GPS receivers, referred to as nodes k and l, can be expressed by relation III.2.

$$d_{kl} = \|p_k - p_l\| \tag{III.2}$$

where the generic p corresponds to the true location of a node.

III.5.1 Absolute Position Differencing (APD)

As previously mentioned, most GPS errors are highly correlated within a limited geographic area. This suggests that the reported absolute positions from GPS receivers may be influenced by the same errors, resulting in the same shifting bias. In a straightforward approach known as Absolute Position Differencing (APD), the estimation of the baseline involves sharing the calculated positions between nodes and utilizing relation III.3.

$$\tilde{d}_{kl} = \|\tilde{p}_k - \tilde{p}_l\| = d_{kl} + \eta \tag{III.3}$$

where the generic $\tilde{p}$ designates the estimated position, and the term η corresponds to the induced bias due the positioning errors recorded by each of the receivers.

Despite its apparent simplicity, the effectiveness of the APD approach is naturally enhanced when GPS receivers employ similar techniques and utilize the same set of satellites for position determination. Consequently, if receivers use different sets of satellites, it can lead to significant errors, potentially surpassing those encountered in standalone positioning methods [7].

In contrast to the APD approach, which relies on separately estimated positions, pseudorange-based approaches combine pseudorange measurements. As discussed earlier, pseudorange measurements are influenced by various error sources that impact baseline estimation. Fortunately, employing differencing techniques like Pseudorange Single Differencing (PSD) and Pseudorange Double Differencing (PDD) can reduce or even eliminate some of these errors.

III.5.2 Pseudorange Single Differencing (PSD)

Assume we have two nodes k and l able to exchange their respective pseudorange measurements as well as their ephemeris data which include information about satellites location. A between-receivers single differencing is performed on pseudorange measurements to the same satellite. As a result, and under a proximity assumption, the errors related to satellite clock, the atmosphere and the ephemeris are considerably reduced. The difference

between the pseudorange measurements of two receivers k and l to the same satellite a, denoted S^a_{kl} and shown in Figure III.3, is expressed by relation III.4.

$$S^a_{kl} = \rho^a_k - \rho^a_l = \Delta r^a_{kl} + (\varepsilon_k - \varepsilon_l) + (\delta^a_k - \delta^a_l) \tag{III.4}$$

where Δr^a_{kl} is the difference between the true ranges from receivers k and l to the same satellite a.

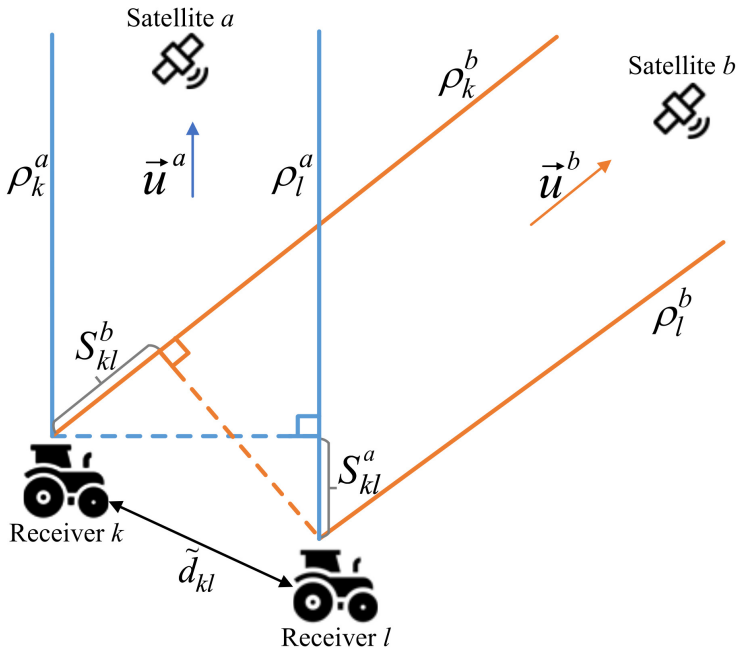


Figure III.3: Baseline estimation between two nodes using pseudorange differencing

Given that the ranges between receivers k and l to satellite a are significantly larger than the actual distance between the receivers, the two vectors pointing from these receivers to the satellite are nearly parallel. Consequently, Δr^a_{kl} represents the projection of the baseline vector in the direction of satellite a and can be expressed using relation III.5.

$$\Delta r^a_{kl} = r^a_k - r^a_l = \vec{u}^a . \vec{d}_{kl} \tag{III.5}$$

where,

- $\vec{u}^a$ denotes the unit vector pointing from receivers k and l in the direction of satellite a. It is expressed as $\vec{u}^a = \vec{p}_k - \vec{p}_a / \|\vec{p}_k - \vec{p}_a\|$ and can be determined using satellite azimuth and elevation angles, as illustrated in Figure III.4;
- $\vec{d}_{kl}$ represents the baseline vector from receiver k to receiver l.

Assuming there are N common satellites visible to both receivers, we can establish a system of equations as shown in relation III.6, neglecting the uncorrelated error term δ. It is important to note that in relation III.4, the contribution of the error term ε associated with receivers' clock errors has not been reduced; on the contrary, it may have increased after the

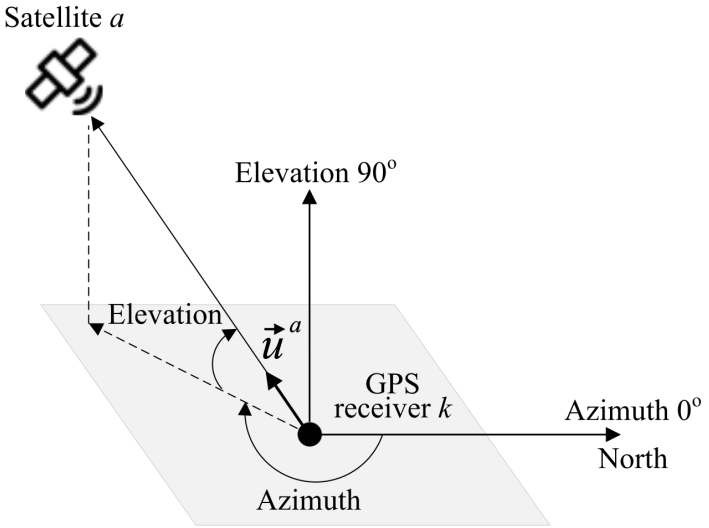


Figure III.4: Determination of unit vector toward satellite using azimuth and elevation angles

differencing operation. As a result, the term $\Delta\varepsilon_{kl} = \varepsilon_k - \varepsilon_l$ remains unknown in the system of equations III.6, and it can be solved using the least squares method.

$$\begin{bmatrix} S_{kl}^1 \\ S_{kl}^2 \\ \vdots \\ S_{kl}^N \end{bmatrix} \approx \begin{bmatrix} \overrightarrow{u}^{1^T} & 1 \\ \overrightarrow{u}^{2^T} & 1 \\ \vdots & 1 \\ \overrightarrow{u}^{N^T} & 1 \end{bmatrix} \begin{bmatrix} \overrightarrow{d}_{kl} \\ \Delta\varepsilon_{kl} \end{bmatrix} \tag{III.6}$$

III.5.3 Pseudorange Double Differencing (PDD)

A second step that aims to eliminate the receiver clock error is performed through double differencing. It consists in differencing two between-receivers single differences toward two different satellites. The pseudorange double difference between receivers k and l toward satellites a and b, denoted D_{kl}^{ab} can be written as shown in relation III.7.

$$\begin{aligned} D_{kl}^{ab} &= S_{kl}^a - S_{kl}^b \\ &= \Delta r_{kl}^a - \Delta r_{kl}^b + [(\delta_k^a - \delta_l^a) - (\delta_k^b - \delta_l^b)] \\ &= (\overrightarrow{u}^a - \overrightarrow{u}^b).\overrightarrow{d}_{kl} + \delta_{kl}^{ab} \end{aligned} \tag{III.7}$$

where the term δ_{kl}^{ab} incorporates the impact of uncorrelated errors on the double difference.

Through this process, the term associated with receivers' clock error $\Delta\varepsilon_{kl}$ is eliminated. Assume that there are N satellites visible to both receivers k and l. By selecting the satellite with the highest SNR values on both receivers as the reference satellite, we can organize the resulting $N-1$ equations in a matrix form as illustrated in relation III.8.

$$D_{kl} = H \overrightarrow{d}_{kl} + \Sigma_{kl} \tag{III.8}$$

where,

- D_{kl} is an array comprising pseudorange double differences between receivers k and l for common visible satellites;
- H is a matrix created using the differences between unit vectors pointing to common visible satellites;
- Σ_{kl} is an array containing the noise term resulting from double differencing operation.

Assuming a zero mean and equal variance for the residual term Σ_{kl}, the system of equations in III.8 can be approximately resolved using the least squares method. As such, the baseline vector is estimated as described by relation III.9.

$$\tilde{d}_{kl} = (H^T H)^{-1} H^T D_{kl} \tag{III.9}$$

III.6 Hardware Architecture

In order to assess the different GPS-based relative positioning approaches, a series of experiments was carried out. The proposed evaluation is conducted using a cost-effective system, depicted in Figure III.5, which integrates the NEO-6 series of u-blox GPS modules, the nRF24l01+ radio transceivers, and the Raspberry Pi 3 compute modules. Each node is powered using a standard smartphone power bank.

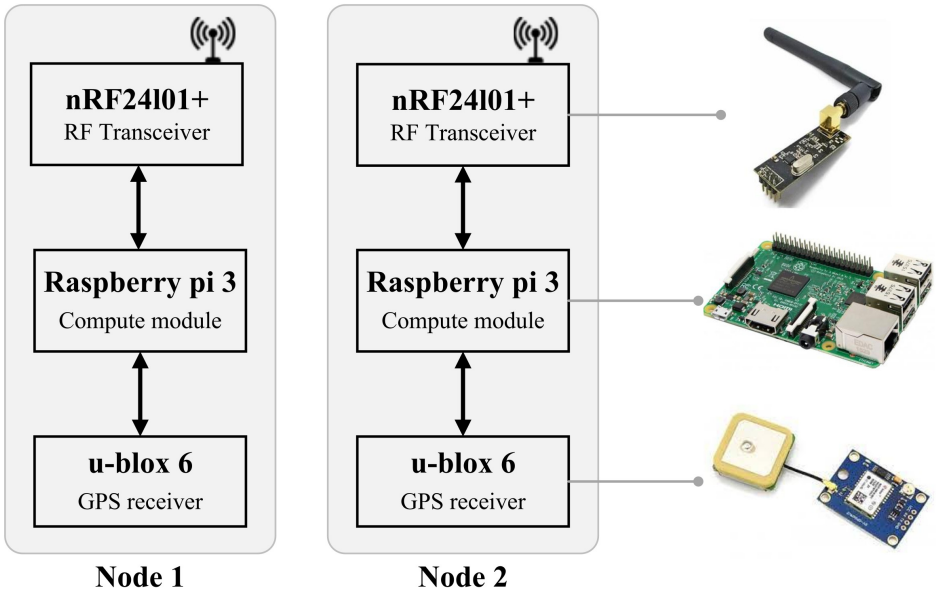


Figure III.5: Hardware composition of the proposed system

III.6.1 u-blox NEO-6M GPS Module

The u-blox NEO-6 series of GPS modules represents a family of compact and reliable devices designed for accurate positioning and navigation applications. Note that the selection of this particular GPS receivers does not limit the generality of the proposed work for other types of modules.

These modules are an example of very popular, cost-effective, high-performance receivers. Their flexible connectivity options, including UART, USB, and I2C interfaces, simplify integration into diverse projects. They typically use an external active antenna connected via an U.FL cable [96].

These GPS modules operate at the L1 frequency and utilize the Coarse Acquisition (C/A) code for signal acquisition. With a tracking sensitivity of -161 dB, they can capture weak signals even in challenging environments. Notably, these modules boast a Time-To-First-Fix of under 1 second, ensuring rapid and accurate positioning information [96].

With multiple variants, such as the NEO-6G, NEO-6M, NEO-6P, and NEO-6V, users can select options with distinct features, including PPP (Precise Point Positioning), raw data support, and dead reckoning capabilities. In our study, we opted for the NEO-6M variant, depicted in Figure III.6. Although this variant initially lacked raw data support, we devised a method to enable raw data output, crucial for our research needs. The modules were configured to deliver both positioning and raw data at a 1 Hz frequency.



Figure III.6: u-blox NEO-6M GPS Module

III.6.2 nRF24l01+ Radio Transceiver

The nRF24L01+ radio frequency (RF) transceiver module is a versatile wireless communication device widely utilized in various electronic applications. Developed by Nordic Semiconductor, this module operates in the license-free 2.4 GHz Industrial, Scientific, and Medical (ISM) band. The nRF24L01+ module supports the SPI protocol, allowing it to operate with all microcontrollers that support SPI communication (e.g., Arduino and Raspberry Pi) [97].

It proposes 125 different channels which give the possibility to have a network of 125 independently working nodes in one zone with 250 kbps, 1 Mbps, and 2 Mbps data rate support. It also offers the possibility to establish communication with up to six different nodes which can be used when implementing a solution with more than two nodes [97].

By employing Nordic's proprietary communication protocol called "Enhanced ShockBurst" the nRF24L01+ offers options such as transmission error management and automatic retransmission in the event of a lack of response from the recipient. Besides, it features automatic packet transmission handling where the terminating part will notify the originating part of a successful transmission using an automatic acknowledgment packet [97].

In selecting the nRF24L01+ radio transceiver, we acknowledge its limitation on maximum data packet size, which is 32 bytes. However, our choice is driven by its noteworthy features that meet the requirements of our study, particularly its cost-effectiveness and the integrated automatic packet transmission handling function.

- The first version, depicted in Figure III.7a, is equipped with a built-in antenna. Its small compact size is suitable for confined spaces but comes at the expense of reduced transmission range;
- The second version, depicted in Figure III.7b and employed in this study, features an external IPX (Internetwork Packet Exchange) antenna and incorporates a power amplifier. This allows for an extended transmission range of up to 1000 meters.



(a) Version 1 **(b)** Version 2

Figure III.7: nRF24l01+ Radio Transceiver

III.6.3 Raspberry Pi 3 Compute Module

The Raspberry Pi is a series of small single-board computers developed in the United Kingdom by the Raspberry Pi Foundation to promote the teaching of basic computer science in schools and in developing countries. Originally designed for educational purposes, its compact size and powerful processing capabilities have made it a popular choice among developers and for research purposes.

The Raspberry Pi 3 compute module, released in February 2016, boasts a family of variants, each catering to different needs and budgets. The standard model (Model B) offers a comprehensive set of features, while others, such as the Raspberry Pi 3 Model B+ and

Raspberry Pi 3 Model A+, introduce enhancements like improved network capabilities. All models feature a Broadcom system on a chip (SoC), which includes an ARM compatible central processing unit (CPU) and an on-chip graphics processing unit (GPU).

In our work, we utilize the Raspberry Pi 3b+ compute module, depicted in Figure III.8. This module is equipped with a Cortex-A53 64-bit Quad-Core processor running at 1.4 GHz and powered by a 5 V/2.5 A DC power input. With 1 GB of RAM, it offers sufficient memory for a wide range of computing tasks. Moreover, it offers diverse connectivity options, encompassing SPI, I2C, UART, and USB, alongside wireless capabilities such as Wi-Fi and Bluetooth [98].

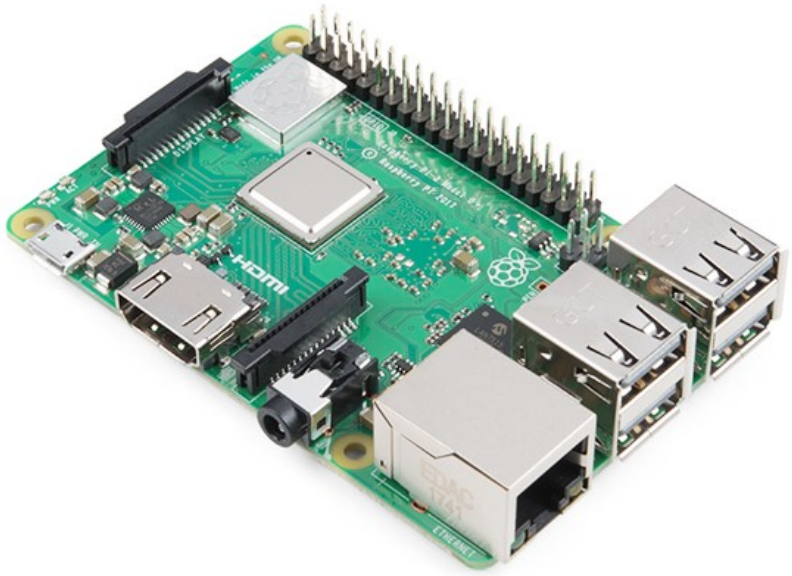


Figure III.8: Raspberry Pi 3b+ Compute Module

As the operating system (OS), it uses the Raspberry Pi OS, formerly known as Raspbian, which is a Unix-like operating system based on the Debian Linux distribution. Nevertheless, The Raspberry Pi is not limited to Raspberry Pi OS, it can use other OS such as DietPi and Batocera. The Raspberry Pi places emphasis on Python as its primary programming language, while also supporting a variety of other languages, including Java and C++.

III.6.4 System Setup

One powerful feature of the Raspberry Pi is its row of GPIO (General-Purpose Input/Output) pins located along the top edge of the board. Serving as a physical interface between the Raspberry Pi and the external environment. These GPIO pins enable the Raspberry Pi to interact with electronic circuits, offering both control and monitoring capabilities. The Raspberry Pi features 40 pins, each serving diverse functions. For a better understanding of the various connectivity options and interfaces, Figure III.9 illustrates the GPIO definition.

The u-blox NEO-6M GPS Module interfaces with the Raspberry Pi 3B+ through the UART (Universal Asynchronous Receiver-Transmitter) interface. UART interface is a fundamental protocol for serial communication, distinguished by features such as

asynchronous operation, full-duplex capability, and bit-by-bit transmission. In its operation, UART uses a start bit to initiate a data frame, followed by 5-8 data bits, an optional parity bit for error detection, and a stop bit to signify the frame's end.

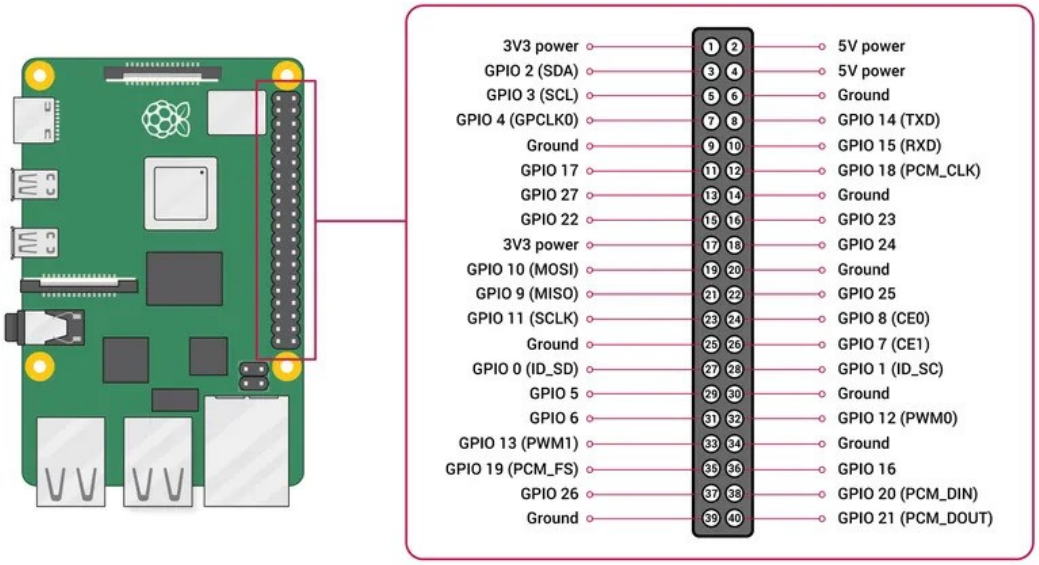


Figure III.9: Raspberry Pi 3b+ GPIO definition

It operates without a shared clock signal, simplifying connections, and supports common data rates like 9600, 19200, 38400, 57600, and 115200 bits per second. UART wiring typically involves three essential wires: TX (Transmit), which carries data from the transmitting to the receiving device; RX (Receive), transmitting data back; and GND (Ground), providing a common voltage reference. Optionally, power (VCC) may be included for voltage supply. The wiring details between the u-blox NEO-6M GPS module and the Raspberry Pi 3b+ is illustrated in Figure III.10.

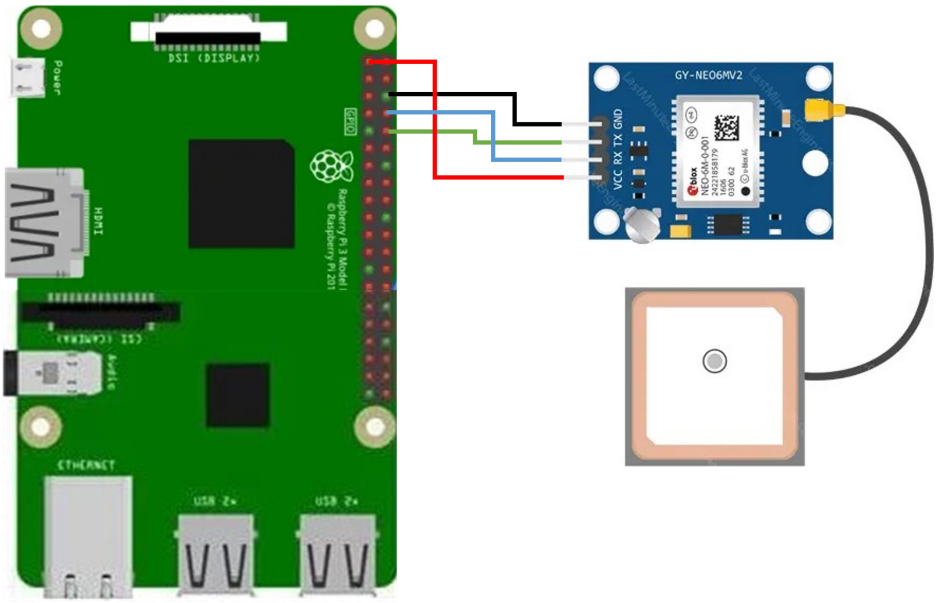


Figure III.10: Raspberry Pi 3b+ and u-blox NEO-6M GPS module wiring

The nRF24l01+ radio transceiver is connected to the raspberry pi 3b+ through Serial Peripheral Interface (SPI) interface. SPI stands out as a synchronous serial communication protocol designed for high-speed data exchange between devices. In this protocol, devices synchronize communication through a shared clock signal, ensuring precise coordination. The full-duplex nature of SPI allows for simultaneous data transmission and reception, enhancing efficiency in data exchange.

The Master-Slave architecture of SPI involves a central device, known as the Master, that initiates and controls communication with one or more peripheral devices, known as Slaves. The communication process is facilitated through four essential wires: SCLK (Serial Clock), MOSI (Master Out Slave In), MISO (Master In Slave Out), and SS (Slave Select). SCLK provides the timing for data transfer, MOSI carries data from the Master to the Slave, MISO carries data from the Slave to the Master, and SS is used by the Master to select the specific Slave for communication.

In operation, the Master initiates communication by selecting a Slave using the SS pin and generating the clock signal (SCLK). Data is then transmitted bit by bit on the MOSI line, synchronized with the SCLK pulses. Simultaneously, data is received on the MISO line, also synchronized with the clock pulses. The transmission concludes as the Master deselects the Slave by raising the SS pin, marking the end of communication. The wiring details between nRF24l01+ radio transceiver and the Raspberry Pi 3b+ is depicted in Figure III.11.

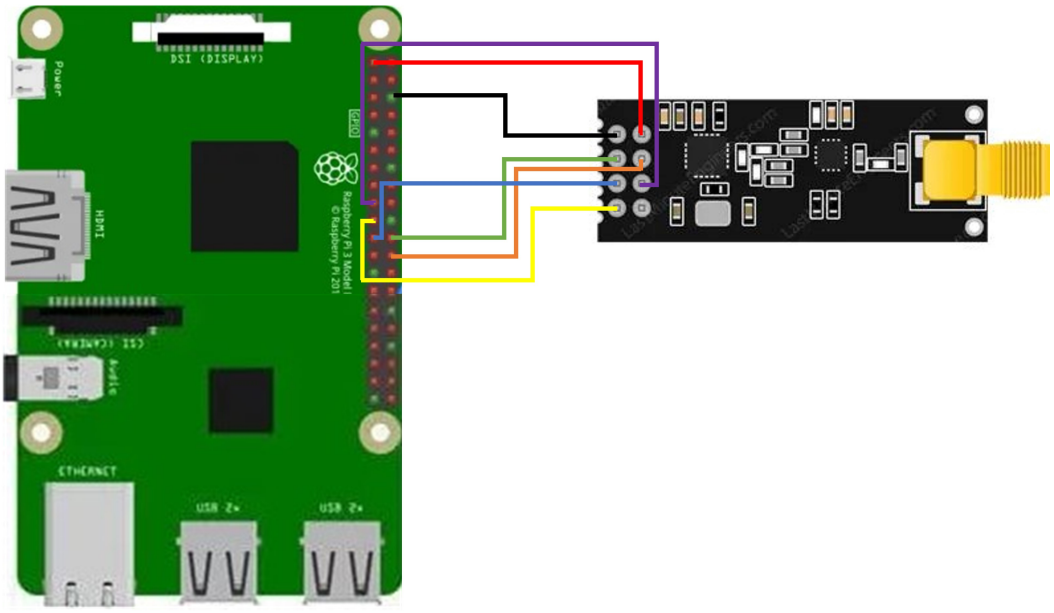


Figure III.11: Raspberry Pi 3b+ and nRF24l01+ radio transceiver wiring

III.7 Implementation

At each node, the Rapsberry Pi 3 compute module undertakes the mission of processing the received GPS messages and extracting the information required for relative positioning approaches implementation. Then, it handles the exchange of this information between the nodes. Once a node in possession of other node GPS information, it implements the different relative positioning approaches. Finally, the obtained real-time results are saved to be collected and analyzed. Figure III.12 summarizes the executed workflow at the level of each node.

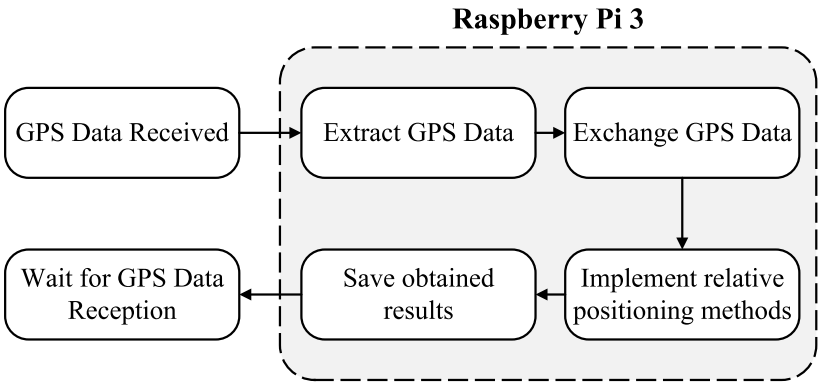


Figure III.12: High-level block scheme describing the workflow at each node

III.7.1 GPS Data Extraction

The implementation of the APD approach requires the nodes to exchange their respective coordinates as well as the measurement time. This information can be extracted from the GPGGA message included in the National Marine and Electronics Association (NMEA) 0183 standard data format supported by most of GPS receivers.

The NMEA 0183 protocol is a standardized communication protocol widely utilized in GPS receivers for the exchange of navigation and positioning data. Originally developed for marine applications, NMEA has become a universal standard in the field of global navigation and positioning systems. It is a text-Based protocol where the information is transmitted as ASCII text strings, making it human-readable.

The most popular NMEA message is the GPGGA message which contains basic information such as measurement time and estimated coordinates. There are also other NMEA messages, such as GPGLL and GPRMC, which, like GPGGA, include GPS coordinates, providing potential alternatives. The following showcases an example of the GPGGA message, and the details are elucidated in Table III.1.

$$\$GPGGA, 181908.00, 3626.70417, N, 00254.39662, E,$$
$$4, 13, 1.00, 495.144, M, 29.200, M, , *40$$

Beyond messages containing GPS coordinates, several companion NMEA messages provide supplementary information. The following are some common ones:

- GPGSA : provides detailed GPS Dilution of Precision (DOP) and comprehensive satellite tracking information, encompassing satellite numbers;
- GPGSV : Presents detailed GPS satellite data, including azimuth and elevation of each tracked satellite;
- GPVTG : Offers information on speed over ground and tracking offset;
- GPGST : Provides estimates of horizontal and vertical precision.

Table III.1: GPGGA message details

N	Item	Description
1	GP	GPS Constellation (GL:GLONASS, GA:GALILEO, GN:Multi GNSS)
2	GGA	Message ID (RMC, GLL, GSA, GSV, etc.)
3	181908.00	UTC time in hours, minutes and seconds (hhmmss.ss)
4	3626.70417	latitude (DDMM.MMMMM) [1]
5	N	North latitude (N or S)
6	00254.39662	longitude (DDDMM.MMMMM)
7	E	East longitude (E or W)
8	4	Quality indicator
9	13	Number of satellites used for positioning
10	1.00	Horizontal dilution of precision (HDOP)
11	495.144	Altitude
12	M	Unit of altitude (Meters or Feet)
13	29.200	Geoidal separation
14	M	Unit of geoidal separation (Meters or Feet)
15	40	Message checksum

[1] D denotes degrees and M denotes minutes

To implement PSD and PDD approaches, exchanging satellite information, including ID, elevation, azimuth, and SNR, between the two nodes is essential. This information is available in GPGSA and GPGSV messages within the NMEA standard data format, as discussed earlier.

Moreover, the exchange of pseudorange measurements to each visible satellite is essential between nodes. This crucial information is derived from the Receiver Manager Messages (RXM) through the u-blox proprietary protocol known as UBX [96].

Unlike the text-based NMEA, UBX transmits data in compact binary format, allowing for faster and more efficient communication. It allows to carry a wealth of information beyond basic navigation data, including receiver status, satellite information, advanced measurements, and raw GPS observations.

UBX messages feature a well-defined structure, ensuring ease of parsing and interpretation. Each message comprises a header that identifies the message type and its length, a payload containing the actual data (with content varying based on the message type), and a checksum mechanism to guarantee data integrity during transmission [96]. The details concerning the extraction of all the required GPS data are summarized in Figure III.13.

III.7.2 GPS Data Exchange

To ensure a fair comparison, it is imperative to implement the various approaches simultaneously, subjecting them to evaluation under identical conditions. However, a

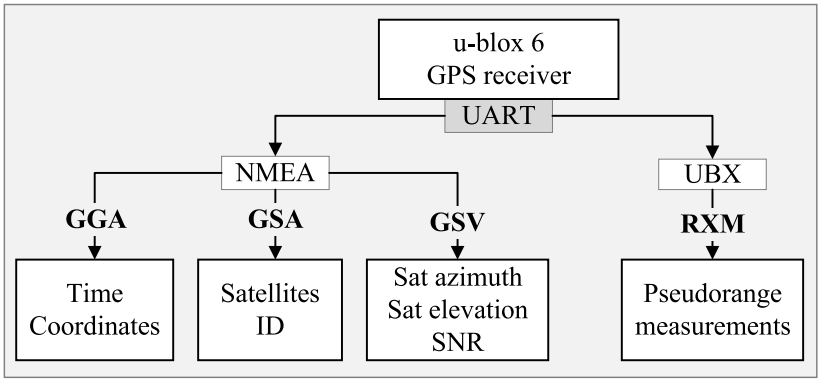


Figure III.13: Details of GPS data extraction

challenge arises due to the size of the necessary GPS data to be exchanged, surpassing the maximum data packet size permitted by nRF24L01+, which is 32 bytes. Consequently, the GPS data are partitioned into a maximum of seven packets, enabling the exchange of information for up to twelve visible satellites, as illustrated in Table III.2.

Table III.2: Structure of the exchanged packets

Packet 1		**Packets 2 to 7**		
Data	**Size(byte)**		**Data**	**Size(byte)**
Packet ID	1		Packet ID	1
Time	3	Sat 1	Pseudorange	8
Latitude	4	Sat 1	Azimuth	2
Longitude	4	Sat 1	Elevation	2
Altitude	4	Sat 1	SNR	1
Fix status	1	Sat 2	Pseudorange	8
DOP	1	Sat 2	Azimuth	2
Sat Number	1	Sat 2	Elevation	2
Sat IDs	12	Sat 2	SNR	1
Packet end	1		Packet end	1
Total	32		**Total**	28

As outlined in section III.6.2, the nRF24L01+ incorporates automatic packet transmission handling, where the receiving part notifies the transmitting part of a successful transmission through an automatic acknowledgment packet. In our study, we take advantage of this functionality. Suppose node one initiates the information exchange by sending a GPS data packet to node two. Upon successful reception, a custom acknowledgment packet containing node two GPS data is compiled and transmitted back to node one within a timeframe not exceeding 130 µs [97].

Experiments confirmed that exchanging one data packet between the two nodes took less than 2 ms at a 1 Mbps data rate. Including a 5 ms delay between transmissions for each of the seven packets, the total communication time remained under 44 ms. Figure III.14 illustrates the timing sequence for GPS data exchange.

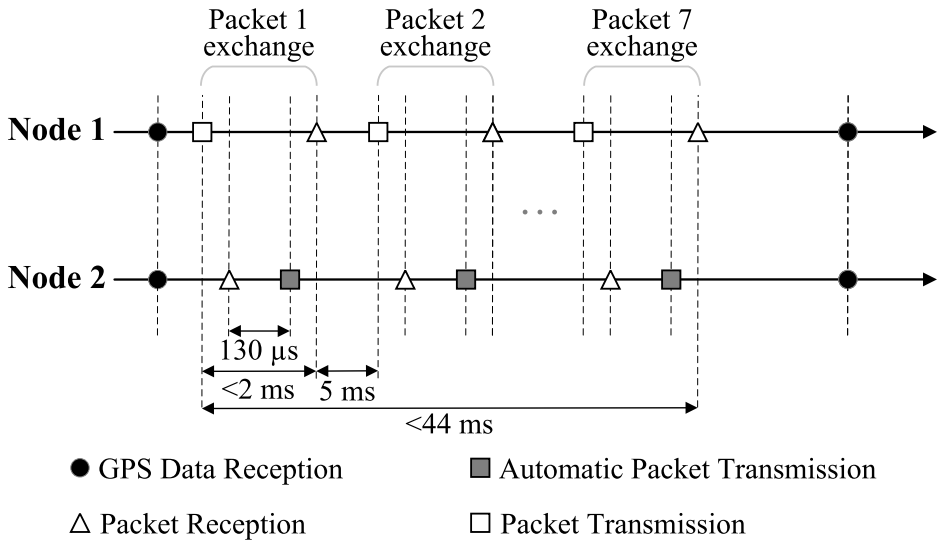


Figure III.14: Timing of the GPS Data Exchange

III.7.3 APD, PSD and PDD Implementation

The APD approach employs a straightforward method by converting geodetic coordinates (latitude, longitude, and altitude) into Cartesian coordinates (X, Y, Z). The baseline between two nodes is then estimated through differencing.

The implementation of PSD and PDD approaches involves identifying common visible satellites and determining corresponding unit vectors. PSD utilizes a single differences matrix, and the least squares method is applied. For PDD, a reference satellite with the highest SNR values on both receivers is selected. The double differences and H matrices are constructed, and the least squares method is employed to estimate the baseline.

It's essential to highlight that the least squares method addresses a system of linear equations ($A \times x = b$), aiming to find a solution for x while minimizing the norm of the residual vector ($b - A \times x$). Figure III.15 provides an overview of the flowcharts for these three approaches.

As for programming language, we have used *python.* for the Integrated Development Environment (IDE), we have used the *Geany* IDE which provides all the essential functionalities to facilitate software development, namely, a source code editor, a debugger, and build automation.

In terms of programming language, we utilized *Python 3.6.* For the Integrated Development Environment (IDE), we opted for *Geany*, which offers essential features to facilitate software development, including a source code editor, debugger, and build automation [99]. Additionally, we incorporated a few open-source libraries, including *serial* for UART communication [100], *spidev* for SPI communication [101], and *lib_nrf24* for interfacing with the nRF24L01+ [102].

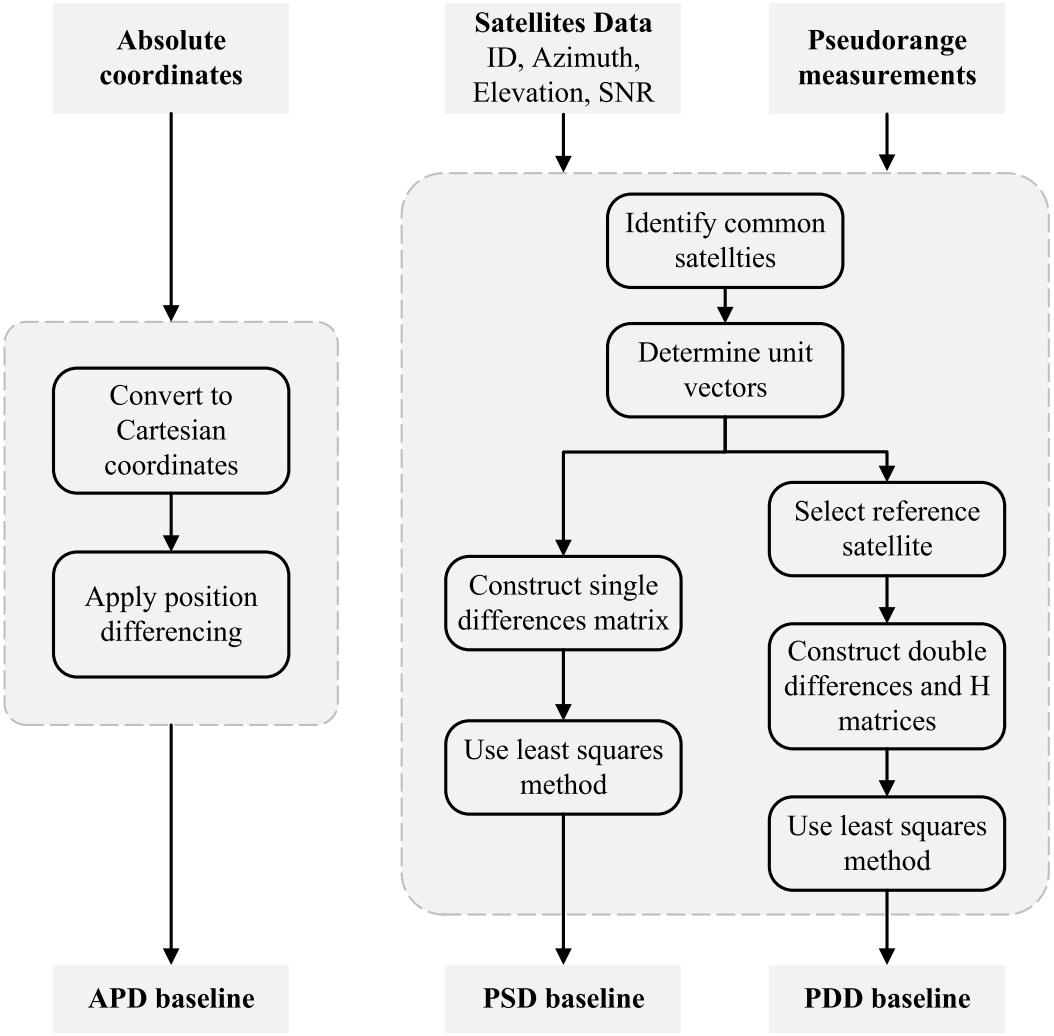


Figure III.15: Flowcharts of APD, PSD and PDD approaches

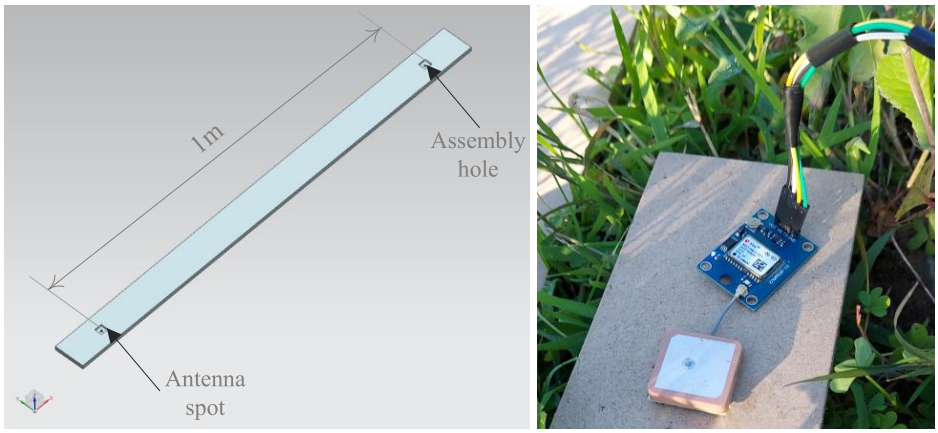
III.8 Experiments, Results and Discussion

III.8.1 Experiments and Results

To assess the proposed approaches, we conducted real-world experiments through two test campaigns. The first campaign took place in an open-sky environment within a soccer stadium, ensuring unobstructed GPS signal propagation and optimal visibility of GPS satellites. The primary objective was to evaluate the proposed approaches under ideal conditions and establish a reference for the second campaign. These tests were carried out at "Imam Lyes" stadium in Medea, Algeria, for approximately 2 hours starting from 1^{st} September 2021, at 08:30 local time (UTC +01).

Regarding the second campaign, we conducted experiments in an agricultural field to assess the applicability of the proposed approaches for agriculture applications. The tests were specifically carried out in an orange trees field situated in the Blida region, Algeria, for about 2 hours, starting from 2^{nd} February 2022, at 08:30 local time (UTC +01). Throughout both campaigns, we considered three distinct scenarios.

In the first scenario, denoted as SS (Static-Static), both nodes remain stationary and are positioned at a predefined distance from each other. To accomplish this, we utilized a set of precisely machined wooden slats, ensuring that the GPS antennas are exactly 1 meter apart, as depicted in Figure III.16. These slats can be assembled to create different baselines. We conducted a total of four tests (2 m, 4 m, 6 m, and 8 m), with each test lasting approximately 5 to 10 minutes.



(a) Design of wooden slats used to set distance between nodes

(b) GPS receiver's antenna setup

Figure III.16: Experiments description

Dynamic scenarios constitute the real challenge for the GPS-based relative positioning approaches. In the second scenario, denoted as scenario DD (Dynamic-Dynamic), both nodes are in motion while maintaining a constant distance between them. Positioned with a fixed 3-meter separation using the slats employed in scenario SS. This scenario is intended to emulate a rover-rover configuration, where each node aims to locate itself with respect to the other node.

In the third scenario, labeled SD (Static-Dynamic), one node remains stationary while the second node is mobile, following a predetermined path. In the stadium, the static node is positioned at the center of the soccer field, and the mobile node moves along the running track. In the agricultural field, the static node is placed at a known location, and the mobile node traverses a square with a side length of 50 meters within the field. Notably, the dynamic experiments were conducted at low speeds, with the moving nodes carried by a walking person (average speed: 1 m/s).

To assess the proposed approaches, the statistical analysis relies on the root mean square error (RMSE), a standard metric that measures the dispersion of estimation errors, given by relation III.10.

$$RMSE = \sqrt{\frac{1}{N}\sum_{i=1}^{N}\left[d(t_i) - \tilde{d}(t_i)\right]^2} \tag{III.10}$$

where $d(t_i)$ and $\tilde{d}(t_i)$ are respectively the real and the estimated distance between the two nodes at time epoch t_i and N is the number of valid samples. Table III.3 summarizes the obtained statistical results for scenarios SS and DD in both campaigns.

Table III.3: Performance Statistics of APD, PSD and PDD for Scenarios SS and DD

Test	Campaign	Valid Samples	RMSE (m)		
			APD	PSD	PDD
SS 2 m	Stadium	684	0.700	1.846	0.066
	Agricultural Field	540	1.859	4.400	1.071
SS 4 m	Stadium	495	1.296	1.666	0.942
	Agricultural Field	539	1.194	2.369	0.960
SS 6 m	Stadium	460	1.014	2.712	0.617
	Agricultural Field	591	2.368	5.320	2.233
SS 8 m	Stadium	271	2.013	1.670	1.513
	Agricultural Field	594	2.508	3.294	1.844
DD 3 m	Stadium	351	1.617	3.104	0.350
	Agricultural Field	627	1.706	4.441	1.373

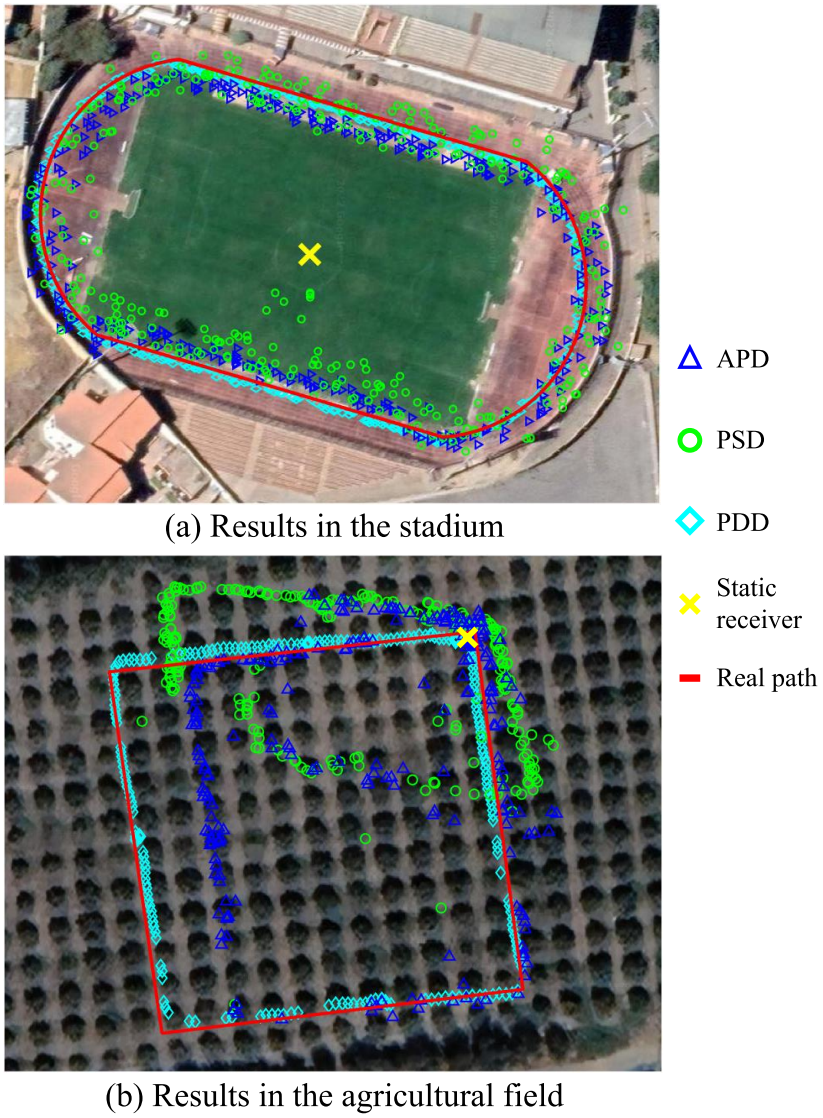
In scenario SD, the georeferenced images (in GeoTIFF format) in Figure III.17 depict the estimated positions obtained by various approaches alongside the actual path. The real path was recorded by recording the coordinates of the mobile node using the u-blox F9P high-precision GNSS receiver. This receiver, operating on multiple frequencies, is known for delivering centimeter-level accuracy, as documented by [103].

III.8.2 Comparison between APD, PSD and PDD

The results in Table III.3 highlight the superior performance of PDD compared to the other two approaches. As discussed in section III.5.3, the double differencing operation effectively minimizes clock biases and correlated errors. However, it tends to increase uncorrelated error terms, including multipath, particularly in dynamic scenarios. Despite this, the obtained RMSE values for the PDD approach in both campaigns, specifically for dynamic scenarios, indicate a relatively minor contribution from these uncorrelated errors. This observation could be attributed to the nature of the conducted dynamic tests, which were characterized by low dynamics.

The APD approach yields relatively good results and secures the second position in terms of accuracy, especially in static scenarios. Despite its straightforward nature, APD's performance improves with increased utilization of common satellites by GPS receivers for position derivation. As depicted in Figure III.18, the results of the SS 6 m experiment are displayed alongside the number of common visible satellites between receivers. Notably, around the orange trees which obstruct GPS signals, the GPS receivers utilize a reduced number of common satellites, elucidating the decline in APD performance in the agricultural field.

The PSD approach demonstrates the lowest performance, particularly in the agricultural field, as illustrated by the results in Figure III.18. Despite the significant reduction in errors associated with satellite clock, atmosphere, and ephemeris through the differencing process



(a) Results in the stadium

(b) Results in the agricultural field

Figure III.17: Comparison between APD, PSD and PDD for Scenario SD

between receivers, the error term linked to the receivers' clock error remains unaddressed. For an accurate baseline estimation, a reliable approximation of this term is required. Accordingly, the underperforming of the PSD approach can be interpreted by a bad estimation of this term.

In theory, the RMSE for any given approach should not vary with the true baseline between nodes. However, in our case, there is some variation among the results of different experiments with different approaches. To provide a comprehensive evaluation of the conducted static scenario tests, the histograms in Figure III.19 show the baseline estimation error statistics obtained by the different approaches in both campaigns.

A general observation reveals that all the approaches exhibit reduced performance in the agricultural field, impacted by the dense foliage of the orange trees, which alters satellite visibility conditions and induces multipath effects. For example, employing the APD approach, nearly 70% of error occurrences in the stadium are less than 1 m, compared to approximately 45% in the agricultural field. Similarly, for the PDD approach, over 76% of the estimation errors are less than 1 m in the stadium, with a noticeable decline in performance observed in the agricultural field.

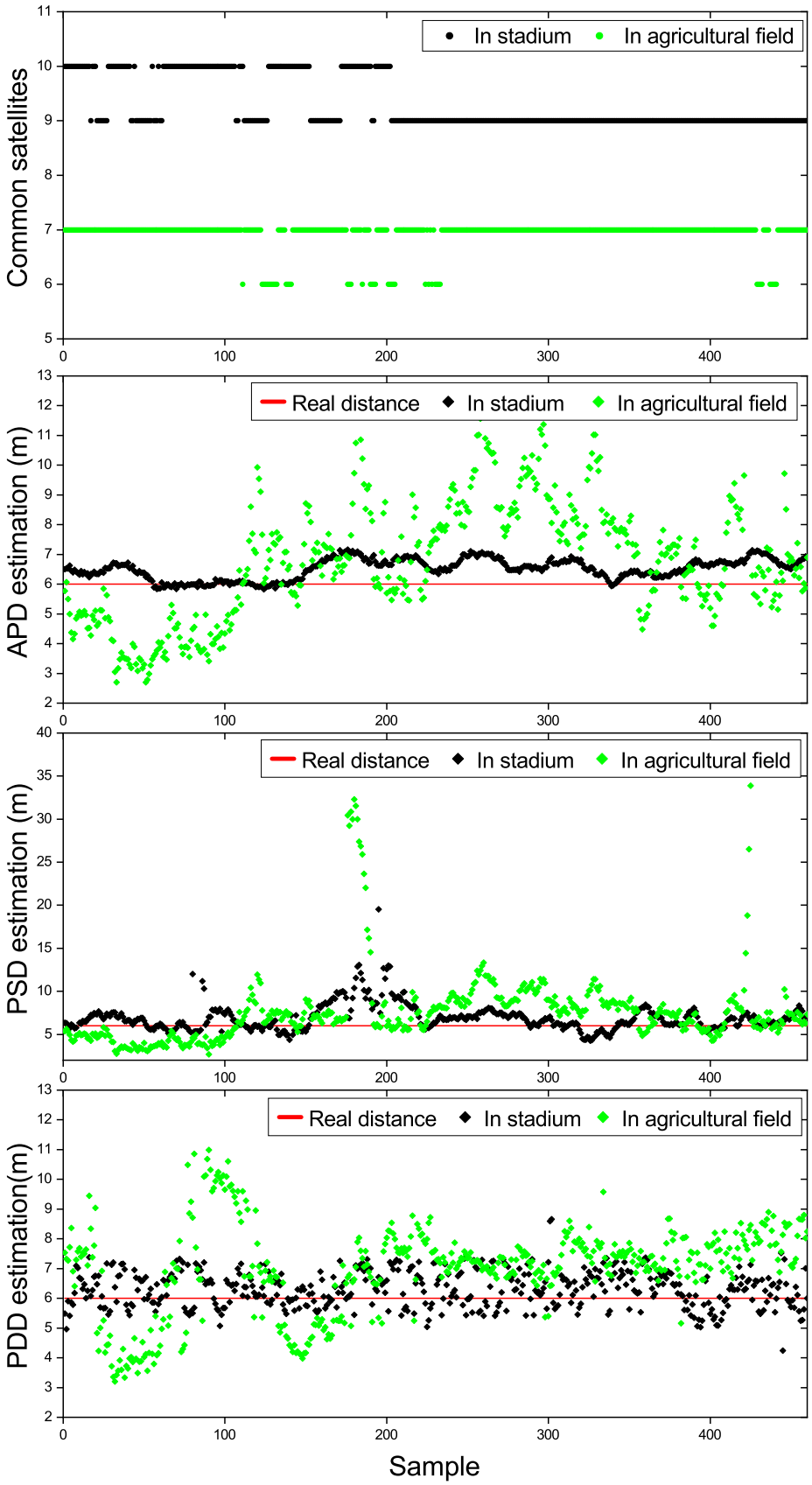


Figure III.18: Static-Static 6 m experiment results for both campaigns

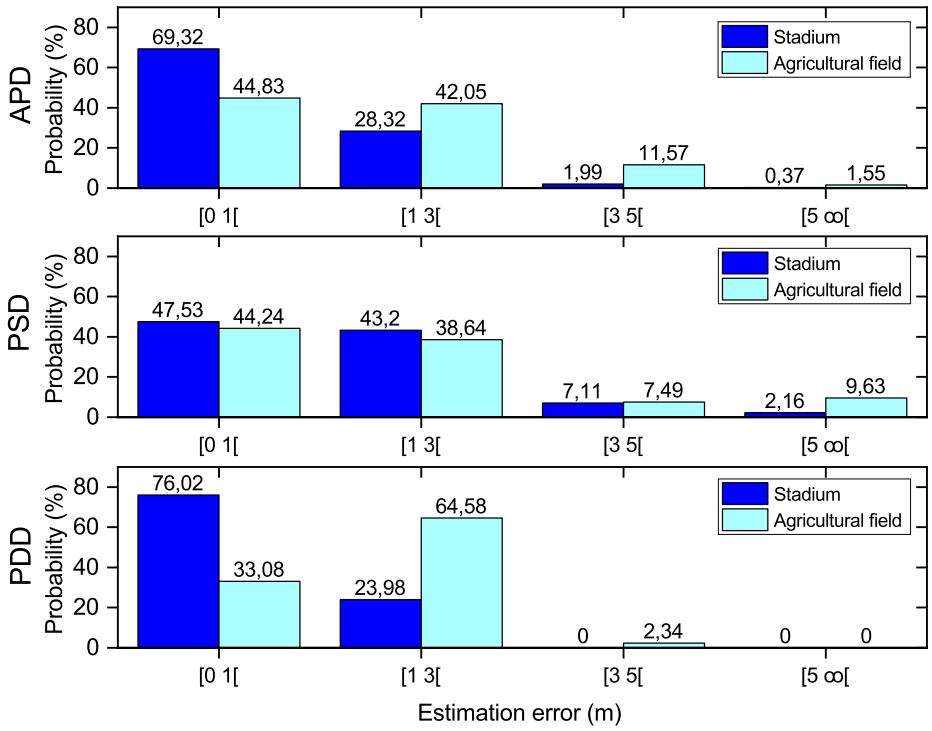


Figure III.19: Histograms of the scenario SS estimation error obtained by APD, PSD and PDD

In the case of scenario SD conducted in the agricultural field, it is noteworthy that the performance of the APD and PSD approaches degrades. Conversely, as depicted in Figure III.17, the PDD approach provides a good estimation in comparison to the actual path followed by the mobile node.

Another crucial aspect to consider when comparing the various approaches is their respective requirements in terms of minimum common visible satellites. As highlighted by Minetto et al. [89], APD can be implemented even when the receivers lack common satellites. However, its performance is expected to significantly degrade in such scenarios. In contrast, PSD and PDD approaches necessitate, at a minimum, the exchange of pseudorange measurements from three and four common satellites, respectively.

In summarizing the performance evaluation of the various approaches, it is noteworthy that the APD approach boasts simplicity in implementation and straightforward information transmission between receivers. However, its effectiveness is highly dependent on the visibility conditions of satellites for both receivers. The PSD approach exhibits the worst performance primarily due to the inaccurate estimation of the term associated with receivers' clock errors. On the other hand, the PDD approach outperforms the others, at the cost of a more elaborate algorithm that demands additional processing time and augments the complexity of information exchange between nodes.

III.8.3 PDD Approach for Agriculture Applications

Figure III.20 presents the Cumulative Distribution Functions (CDFs) depicting the errors between true and estimated distances obtained by various approaches in the agricultural

field. Remarkably, over 97% of the distance estimation errors achieved through the PDD approach are below 3 m, with sub-meter accuracy attainable 33% of the time.

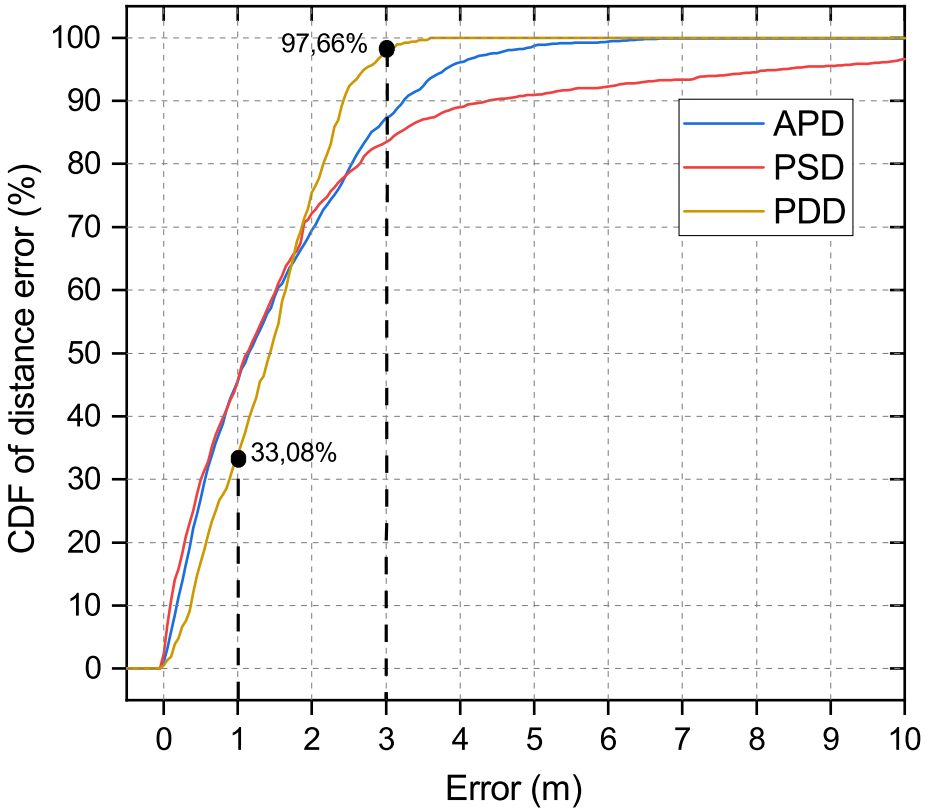


Figure III.20: CDFs of distance error obtained by APD, PSD and PDD for scenario SS in the agricultural field

This corresponds to a considerable improvement in positioning accuracy compared to standalone GPS positioning, which usually provides accuracy within the range of 10 to 15 m, as demonstrated in Figure III.21. Furthermore, this level of performance is comparable to the accuracy offered by the Wide Area Augmentation System (WAAS) service within the USA, delivering better than 3 m accuracy 95% of the time [54].

In precision agriculture, the required level of positioning accuracy varies depending on the specific tasks at hand. Operations like variable rate application, soil and yield data referencing, tillage, certain types of fertilizer and chemical application, and seeding can be effectively accomplished using the proposed solution.

However, for tasks demanding extremely high accuracy in positioning, such as strip-tilling and drip-tape placement, the proposed solution may fall short, and more advanced positioning systems are essential [104]. It's worth noting that the cost of existing solutions capable of performing these operations exceeds several thousand US dollars, while the proposed solution is approximately 100 USD.

III.9 Conclusion

This chapter explores the potential of employing real-time relative positioning methods for agricultural applications as an alternative to conventional absolute positioning solutions.



Figure III.21: Comparison between results obtained by PDD and standalone GPS positioning

We detail various GPS-based relative positioning approaches, including APD, PSD, and PDD. Subsequently, we have effectively implemented these strategies using low-cost modules. Special emphasis has been placed on the design and timing aspects of the GPS data exchange.

Field experiments were conducted in both an open-sky environment and an agricultural field to evaluate the performance of the proposed approaches. PDD demonstrated the best results, achieving around 76% of estimation errors less than 1 m in the open-sky scenario. Despite performance degradation in the agricultural field, over 97% of estimation errors remained below 3 m. APD also delivered good results, but its effectiveness was closely tied to the number of common satellites visible to the receivers. PSD, however, exhibits the worst performance.

Undoubtedly, the PDD approach significantly improved positioning accuracy compared to standalone GPS positioning. This enhancement enables more precise execution of operations such as tillage, seeding, and certain types of fertilizer and chemical application. The proposed system offers a practical and affordable positioning solution, particularly beneficial in regions where farmers face challenges affording expensive existing solutions.

In the field of positioning, our future work aims to enhance the proposed positioning system's robustness by incorporating advanced techniques like sensor fusion and dead reckoning, addressing issues related to GPS signal discontinuity. Additionally, exploring the application of new Artificial Intelligence techniques to mitigate uncorrelated errors such as receiver noise and multipath interference will complement the findings presented in this study.

Chapter IV

Orientation Estimation : Sensors and Algorithms

IV.1 Introduction

The movement of a rigid body in three-dimensional (3D) space involves both translational and rotational motions in 3D. Translation refers to the linear displacement of the mass center, while rotation involves variations in angular position, as illustrated in Figure IV.1. While representing translational motion is straightforward, the representation of orientation is non-trivial and more complex [105]. As a result, various methods for representing orientation have been proposed, and this chapter presents the most commonly used ones.

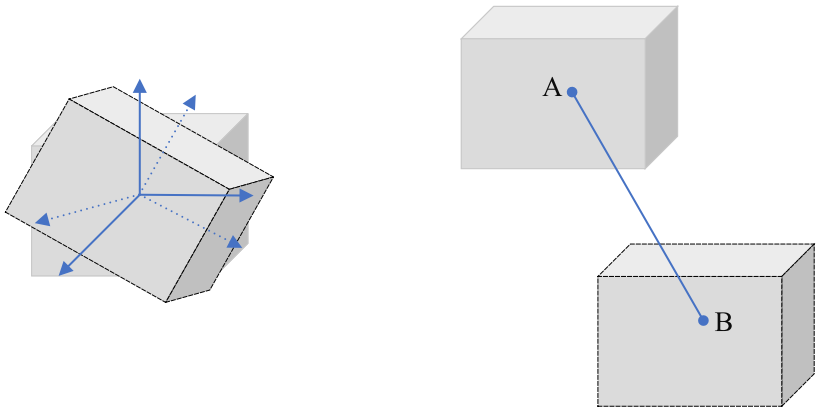


Figure IV.1: Visualization of the rotational (left) and translational (right) motions of a rigid body

Then, we will explore various sensors utilized for orientation estimation, with a primary focus on Inertial Measurement Units (IMUs). While our emphasis lies on IMUs, it's important to note that orientation estimation using IMUs is not limited to agriculture applications. IMUs find wide-ranging applications across various domains beyond agriculture-specific contexts.

In addition to exploring different sensors for orientation estimation, this chapter delves into the algorithms commonly employed with IMUs. Among these algorithms, Kalman filters and complementary filters stand out as the most widely used methods for processing IMU data to estimate orientation. Moreover, with the advancements in AI-based techniques, particularly Neural Networks (NNs), there has been a growing interest in utilizing NNs for orientation estimation. In this chapter, we examine how NNs have been integrated into orientation estimation frameworks and discuss their potential advantages and challenges compared to conventional filtering approaches.

IV.2 Definitions and Common Concepts

IV.2.1 Definitions

IV.2.1.1 Orientation and its Applications

The 3D orientation of a body is determined by the relative orientation between a coordinate frame attached to the body and a reference frame [106]. This reference frame may be a fixed frame or a frame attached to another object, as discussed in section IV.2.2.

Orientation information plays a crucial role in a variety of applications. As depicted in Figure IV.2, potential application scenarios include, but are not limited to, pedestrian dead reckoning [107], human activity recognition [108, 109], bio-logging of animal behaviours [110], and control and navigation of aircraft, satellites, and unmanned vehicles [111, 112].



Figure IV.2: Examples of orientation estimation applications

IV.2.1.2 Orientation vs. Attitude

In the field of 3D geometry and motion, the terms 'attitude' and 'orientation' are often employed interchangeably. However, subtle distinctions emerge, especially in specific applications.

In aviation, attitude typically denotes the orientation of an object, especially an aircraft. It is commonly understood as the orientation relative to the horizontal plane, encompassing only two angles. In the conventional definition, heading is not taken into account. Nevertheless, in certain applications, attitude may also include heading, effectively becoming a synonym for orientation.

IV.2.1.3 Orientation vs. Rotation

The terms 'orientation' and 'rotation' are related concepts but refer to slightly different aspects in the spatial representation of objects. On one hand, orientation refers to the general direction or 'pose' of an object in space relative to a reference frame. It describes how an object is oriented with respect to a reference coordinate system.

On the other hand, rotation specifically refers to the transformation that changes the orientation of an object in three-dimensional space. It describes the process of changing the object's orientation. So, orientation is a broader term that encompasses the overall spatial arrangement of an object, while rotation specifically refers to the transformation that changes this orientation by rotating the object around one or more axes [113].

IV.2.1.4 Determination vs. Estimation

While the terms 'determination' and 'estimation' are frequently used interchangeably in various research papers, it's important to clarify that they represent separate concepts. Orientation determination adopts an algebraic approach, with the primary objective of minimizing the cost function [114]. Specific examples of orientation determination algorithms include tri-axial attitude determination (TRIAD) [115], quaternion estimator (QUEST) [116], and singular value decomposition (SVD) [117].

The evolution of estimation theory has led to the emergence of the concept of orientation estimation. In comparison to orientation determination, orientation estimation diverges by not relying on algebraic methods; instead, it employs data fusion filters that consider the statistical properties of sensors' measurements. Typically, these filters combine predictions and noisy measurements, ensuring that the stochastic characteristics of measurements are taken into account [113].

IV.2.2 Coordinate Frames

Coordinate frames can be classified into reference frames and local frames. Reference frames, like the Earth-Centered Inertial frame (ECI) or the Earth-Centered Earth-Fixed frame (ECEF), are typically considered stationary under specific conditions. Conversely, local frames may exhibit rotation with respect to a reference frame, as exemplified by the body frame. In this section, we will introduce three prevalent coordinate frames: the body frame, the ECEF frame and the local level frame.

IV.2.2.1 Body Frame

As depicted in Figure IV.3, the body frame is composed of an origin typically situated at the object's center of gravity, along with three orthogonal axes forming a right-handed system. In the literature, two commonly employed body frames are the forward-right-down (FRD) frame and the right-forward-up (RFU) frame.

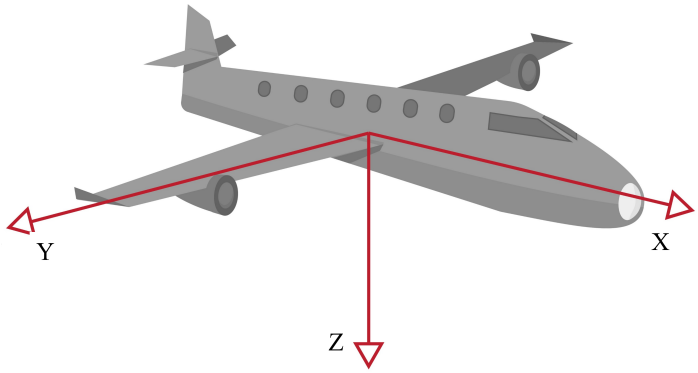


Figure IV.3: Body frame

The distinction between these frames lies in the directions of their axes. In the RFD frame, which will be the reference in the subsequent sections of this thesis, the x-axis points in the forward direction, the y-axis points to the right, and the z-axis points downward.

IV.2.2.2 ECEF Frame

The ECEF frame serves as a global reference frame, with its origin located at the Earth's center and three orthogonal axes fixed relative to the Earth. The z-axis aligns with the geographical north pole, the x-axis points to the intersection of the IERS Reference Meridian (IRM) and the equator, and the y-axis completes the right-handed system. Unlike the ECI frame, which remains fixed in relation to Earth, the ECEF frame undergoes rotation with the Earth at an angular velocity of approximately 15 °/h.

IV.2.2.3 Local Level Frame

This coordinate frame is typically associated with an observer or a vehicle and serves as a local reference for describing orientation relative to the Earth's surface. Similar to the body frame, two variants of the local level frame are recognized: the north-east-down (NED) frame and the east-north-up (ENU) frame. In our study, we employ the NED frame, where the z-axis points vertically downward, aligning with the local gravity vector and defining the 'level' direction. The x-axis corresponds to geographical north, and the y-axis completes the right-handed coordinate system, pointing eastward.

The local level frame is advantageous for tasks such as navigation, where it provides a convenient local reference aligned with the observer's horizontal plane, simplifying the description of movement and orientation in a local context.

IV.2.3 Orientation Representations

As mentioned earlier, representing orientation is more complex than representing translational motion. Consequently, multiple formulations have been developed to depict the orientation of an object [118]. This section presents some commonly used orientation representations along with the associated conversions between them.

IV.2.3.1 Euler Angles

Euler angles, named after the Swiss mathematician Leonhard Euler, are a set of three angles that describe the orientation of a rigid body in three-dimensional space. This representation offers a straightforward way to decompose a complex rotation into a sequence of three fundamental movements around well-defined axes. Euler angles provide a concise and intuitive way to express the orientation of an object and finds widespread application in diverse fields, including aerospace, computer graphics, and robotics.

These three angles correspond to rotations about distinct axes, typically designated as roll (ϕ), pitch (θ), and yaw (ψ) as depicted in Figure IV.4 sourced from [113]. Roll angle signifies the rotation about its x-axis required to align the vehicle's lateral axis with the horizontal plane (positive when rolling to the right). Pitch angle represents the angle between the vehicle's longitudinal axis and its projection on the horizontal plane (positive when pitching up). Yaw angle is the angle between the projection of the vehicle's longitudinal axis on the local horizontal plane and the geographical north (positive in the clockwise direction).

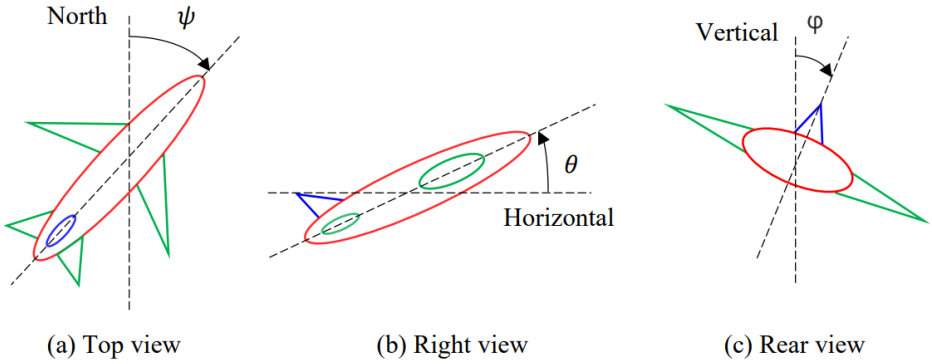


Figure IV.4: Euler angles Definition ((a): yaw, (b): pitch, and (c): roll)

There are several conventions for Euler angles, depending on the axes about which the rotations are carried out. The crucial aspect lies in the sequence of applying rotations. Different conventions like XYZ, ZYX, or YXZ exist, each dictating the order of rotations, and leading to distinct interpretations of the final orientation. In our study, we have adopted the aeronautical convention (ZYX), where the initial rotation is around the z-axis, followed by the y-axis, and finally around the x-axis.

The gimbal lock problem is a well-known issue associated with Euler angles representation. It arises when two rotations bring two axes into alignment, creating a situation where one rotational degree of freedom is lost. This phenomenon introduces complexity in orientation representation and may lead to ambiguity in interpreting the object's orientation. While Euler angles provide an intuitive way to express rotations, gimbal lock phenomenon highlights a limitation in certain scenarios, prompting the exploration of alternative representation methods.

IV.2.3.2 Quaternions

This powerful representation is created by William Hamilton in 1843. By definition, a quaternion is a four-component vector with some additional operations defined on it. A quaternion q has a scalar part q_0 and a three-vector part $q_{1:3}$. Instead of decomposing a rotation into sequential rotations around axes, quaternions capture it directly as a single, compact entity. This structure encodes both the amount of rotation (represented by q_0) and the axis of rotation (represented by $q_{1:3}$). A quaternion q can be written as shown in relation IV.1.

$$q = q_0 + iq_1 + jq_2 + kq_3 = \begin{bmatrix} q_0 \\ q_1 \\ q_2 \\ q_3 \end{bmatrix} = \begin{bmatrix} q_0 \\ q_{1:3} \end{bmatrix} \tag{IV.1}$$

where i, j, and k refer to three imaginary unit numbers, also known as the fundamental quaternion units, q_0 denotes the scalar part and $q_{1:3}$ is a three-dimensional vector.

In our study we adopted the Hamilton convention which implies a right handed rotation rule as illustrated in Table IV.1, where the resulting values are obtained by multiplying row elements with column elements. It is worth noting that in other works the left handed convention can be employed [118].

Table IV.1: Multiplication rules of the fundamental quaternion units

x	**1**	**i**	**j**	**k**
1	1	i	j	k
i	i	-1	k	-j
j	j	-k	-1	i
k	k	j	-i	-1

In quaternion representation, it is crucial to ensure that the quaternion is normalized to maintain its unit length. Normalization is essential for accurate and stable quaternion operations, preventing undesired distortions in the representation of rotations. The normalization process involves dividing the quaternion by its magnitude [119].

Some additional operations are defined on quaternions. The most important quaternion operation is the multiplication of a pair of quaternions p and q, which is defined using as relation IV.2.

$$p \otimes q = \begin{bmatrix} p_0 q_0 - p_{1:3}^T q_{1:3} \\ p_0 q_{1:3} + q_0 p_{1:3} + p_{1:3} \times q_{1:3} \end{bmatrix} = \begin{bmatrix} p_0 q_0 - p_1 q_1 - p_2 q_2 - p_3 q_3 \\ p_0 q_1 + p_1 q_0 + p_2 q_3 - p_3 q_2 \\ p_0 q_2 - p_1 q_3 + p_2 q_0 + p_3 q_1 \\ p_0 q_3 + p_1 q_2 - p_2 q_1 + p_3 q_0 \end{bmatrix} \tag{IV.2}$$

In contrast to Euler angles, which directly correspond to familiar rotations around the x, y, and z axes, quaternion representation is considered less intuitive and can pose challenges

in visualization and interpretation. However, the adoption of quaternions offers significant advantages, particularly in avoiding the notorious gimbal lock phenomenon. The four-dimensional nature of quaternions allows them to effectively address this issue, providing reliability in scenarios involving large or complex rotations, making them a preferred choice in various applications.

IV.2.3.3 Direction Cosine Matrix (DCM)

The DCM, often referred to as a rotation matrix, represents a matrix that facilitates the transformation of vector coordinates from one frame to another [120]. The DCM is a a 3 $\times$ 3 square matrix, comprising nine entries that represent the direction cosine values between an initial reference frame and a second reference frame.

Let's consider two reference frames, denoted as A and B, where B signifies the body frame, and A serves as the initial reference frame. These frames are defined by a set of three orthogonal unit vectors $\{a_1, a_2, a_3\}$ and $\{b_1, b_2, b_3\}$, respectively.

As shown in Figure IV.5, the axis b_1 creates three angles α_{11}, α_{12} and α_{13} with each of the vectors b_1, b_1 and b_1, respectively. The same follows for the other two vectors b_2 and b_3. Then, each of the unit vectors of reference B can be represented in terms of the unit vectors of reference A as shown in relation IV.3.

$$\begin{aligned} b_1 &= \cos(\alpha_{11})a_1 + \cos(\alpha_{12})a_2 + \cos(\alpha_{13})a_3 \\ b_2 &= \cos(\alpha_{21})a_1 + \cos(\alpha_{22})a_2 + \cos(\alpha_{23})a_3 \\ b_3 &= \cos(\alpha_{31})a_1 + \cos(\alpha_{32})a_2 + \cos(\alpha_{33})a_3 \end{aligned} \tag{IV.3}$$

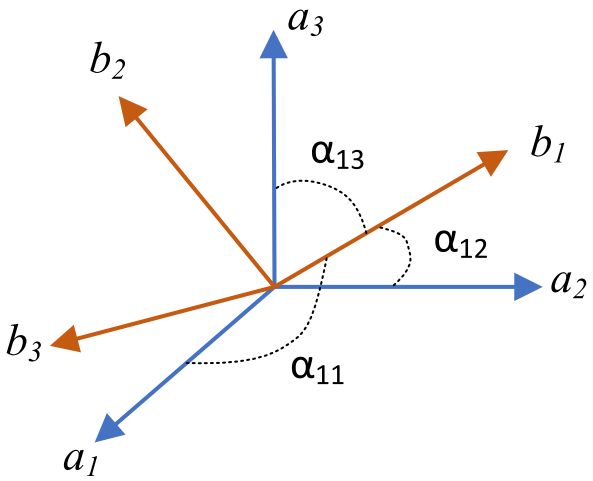


Figure IV.5: A and B reference frames

Thus, the DCM between two unit vectors is just the dot product of them, then the DCM can be expressed as shown in relation IV.4.

$$DCM = \begin{pmatrix} b_1.a_1 & b_1.a_2 & b_1.a_3 \\ b_2.a_1 & b_2.a_2 & b_2.a_3 \\ b_3.a_1 & b_3.a_2 & b_3.a_3 \end{pmatrix} \tag{IV.4}$$

There are a few properties of the DCM that make it a unique method for representing an object's orientation. DCMs are always orthogonal, maintaining perpendicular rows and columns, and possess a determinant of 1. They exhibit a straightforward relationship between inverses and transposes, where the transpose serves as the inverse. Additionally, DCMs offer the ability to represent consecutive rotations through multiplication, allowing for the construction of complex movements from simpler rotations.

While the orientation described using DCM avoids singularities, it comes with a significant drawback. The DCM employs nine parameters to define an orientation, but only three are necessary. This redundancy, where six of the DCM values are redundant, makes it impractical for real-time orientation tracking. Instead, the DCM is commonly employed for vector projection into various reference frames.

IV.2.3.4 Other representations

In addition to the three common representations that have been discussed, various other methods exist for orientation representation. These alternative representations cater to specific applications and mathematical conveniences. While comprehensive details are beyond the scope of our current discussion, it is important to acknowledge their existence and significance in certain contexts.

The Euler axis-angle representation involves expressing orientation with four parameters: a three-component unit axis, often referred to as the Euler axis, and the rotation angle about this axis [121]. On the other hand, the rotation vector representation is a concise representation, utilizing a three-dimensional vector to convey both the axis of rotation and the associated rotation angle. Both representations are based on Euler's theorem which states that a sequence of successive rotations can always be equivalently represented by a single rotation about a specific axis [122]. Although these two representations are fundamentally identical, the former employs four parameters, while the latter achieves the same result with only three parameters.

Rodrigues parameters, also referred to as the Gibbs vector, offer a three-dimensional orientation representation that facilitates transitions between rotation matrices and quaternions. However, it's crucial to note that the orientation described by Rodrigues parameters becomes singular as the rotation angle approaches $\pm\pi$ [118].

In response to this singularity issue, modified Rodrigues parameters emerged as a variant, aiming to decrease the likelihood of numerical singularities. It's noteworthy, though, that the computational load associated with modified Rodrigues parameters is higher compared to the original Rodrigues parameters [113].

Cayley-Klein parameters is a singularity-free representation which provides an alternative means of orientation representation, involving a 2×2 square matrix directly derived from quaternion representation. In opposition to the former representations, it uses complex numbers which encodes both the amount of rotation and the axis of rotation [123].

IV.2.3.5 Conversion between Representations

IV.2.3.5.1 Conversion between Euler angles and DCM As we have chosen to adhere to the aeronautical convention (ZYX) in our study, the DCM corresponding to these rotations can be expressed using the relation given in Equation IV.5, where the abbreviations c = cos and s = sin are used for notation brevity.

$$\begin{aligned} DCM &= R_1(\psi)R_2(\theta)R_3(\phi) \\ &= \begin{pmatrix} c\theta\, c\psi & c\theta\, s\psi & -s\theta \\ s\phi\, s\theta\, c\psi - c\phi\, s\psi & s\phi\, s\theta\, s\psi + c\phi\, c\psi & s\phi\, c\theta \\ c\phi\, s\theta\, c\psi + s\phi\, s\psi & c\phi\, s\theta\, s\psi - s\phi\, c\psi & c\phi\, c\theta \end{pmatrix} \\ &= \begin{pmatrix} B_{11} & B_{12} & B_{13} \\ B_{21} & B_{22} & B_{23} \\ B_{31} & B_{32} & B_{33} \end{pmatrix} \end{aligned} \tag{IV.5}$$

Euler angles ϕ, θ et ψ can be obtained from a given DCM using relation IV.6.

$$\begin{aligned} \phi &= \tan^{-1}(\frac{B_{23}}{B_{33}}) \\ \theta &= -\sin^{-1}(B_{13}) \\ \psi &= \tan^{-1}(\frac{B_{12}}{B_{11}}) \end{aligned} \tag{IV.6}$$

IV.2.3.5.2 Conversion between DCM and Quaternions The process of converting a given quaternion representation to its corresponding rotation matrix is provided in relation IV.7 [124].

$$DCM = \begin{pmatrix} q_0^2 + q_1^2 - q_2^2 - q_3^2 & 2(q_1q_2 - q_0q_3) & 2(q_1q_3 + q_0q_2) \\ 2(q_1q_2 + q_0q_3) & q_0^2 - q_1^2 + q_2^2 - q_3^2 & 2(q_2q_3 - q_0q_1) \\ 2(q_1q_3 - q_0q_2) & 2(q_2q_3 + q_0q_1) & q_0^2 - q_1^2 - q_2^2 + q_3^2 \end{pmatrix} \tag{IV.7}$$

Various methods exist for extracting the quaternion from a given DCM, though some of these methods may encounter divide-by-zero singularities for specific orientations. A numerically stable approach to computing the quaternion involves initiating the process by calculating the squares of each quaternion term, as illustrated by relation IV.8

$$\begin{aligned} q_1^2 &= \frac{1}{4}(1 + B_{11} - B_{22} - B_{33}) \\ q_2^2 &= \frac{1}{4}(1 - B_{11} + B_{22} - B_{33}) \\ q_3^2 &= \frac{1}{4}(1 - B_{11} - B_{22} + B_{33}) \\ q_4^2 &= \frac{1}{4}(1 + B_{11} + B_{22} + B_{33}) \end{aligned} \tag{IV.8}$$

The specific value for a quaternion term can be obtained by taking the square root of the maximum value among the quaternion terms. Subsequently, the remaining terms can be computed utilizing the appropriate formula from relation IV.9.

$$\begin{aligned} q &= \frac{1}{4q_1}\begin{bmatrix} 4q_1^2 \\ B_{12}+B_{21} \\ B_{31}+B_{13} \\ B_{23}-B_{32} \end{bmatrix} = \frac{1}{4q_2}\begin{bmatrix} B_{12}+B_{21} \\ 4q_2^2 \\ B_{23}+B_{32} \\ B_{31}-B_{13} \end{bmatrix} \\ &= \frac{1}{4q_3}\begin{bmatrix} B_{31}+B_{13} \\ B_{23}+B_{32} \\ 4q_3^2 \\ B_{12}-B_{21} \end{bmatrix} = \frac{1}{4q_4}\begin{bmatrix} B_{23}-B_{32} \\ B_{31}-B_{13} \\ B_{12}-B_{21} \\ 4q_4^2 \end{bmatrix} \end{aligned} \tag{IV.9}$$

IV.2.3.5.3 Conversion between Euler angles and Quaternions Deriving a set of Euler angles from a quaternion involves a two-step process utilizing the transformations described above. Initially, the quaternion undergoes transformation into a DCM using relation IV.7. Subsequently, this DCM is further converted into a set of Euler angles through the transformation specified in relation IV.6.

Conversely, computing a quaternion from a set of Euler angles follows a similar two-step approach. Initially, the set of Euler angles is transformed into a DCM using relation IV.5. Subsequent application of relations IV.8 and IV.9 allows for the conversion of the DCM into the corresponding quaternion.

IV.3 Sensors for Orientation Estimation

In this section, we will acknowledge the existence of various sensors used for orientation estimation, providing a brief overview of these sensors with a particular emphasis on Inertial Measurement Units (IMUs).

IV.3.1 Vision-based

A vision sensor has the capability to offer comprehensive details about the surrounding environment. In the past, vision was primarily utilized for position and speed estimation rather than for orientation estimation. However, in recent research, there has been significant advancement in orientation estimation algorithms primarily based on vision.

The utilization of a vision system as the primary sensor for orientation estimation has been implemented through diverse methods, aligning with the specific characteristics of the surrounding environment, be it indoor or outdoor. Various types of targets have been employed, including landmarks, water surfaces, buildings, road centerlines, known ground target positions, etc [125].

It's worth noting that a significant portion of these research studies has integrated additional sensors alongside vision sensors. For instance, in [126], fusion of image positions of landmarks and IMU information was employed to obtain navigation parameters, including orientation. Similarly, in the study conducted in [127], IMU, magnetometer, and altimeter were incorporated alongside a camera to estimate various parameters, including orientation angles.

IV.3.2 GNSS-based

Orientation angles derived using GNSS can be estimated through the utilization of either a single or multiple antennas. The single antenna approach involves estimating orientation angles using signal strength measurements or GNSS-derived acceleration. However, this method necessitates auxiliary information, such as accelerometer or magnetometer measurements. While the single antenna-based approach is advantageous for systems with space limitations, its accuracy typically falls within the range of 0.5° to 10° [128].

Conversely, the multi-antenna method can achieve a higher level of orientation accuracy, typically in the order of 0.1°. In this approach, the orientation is estimated using two or more GNSS antennas mounted on a platform, with the precisely known baselines between the antennas being a crucial parameter in the estimation process [128].

In GNSS-based orientation estimation, both pseudo-range and carrier-phase observations are theoretically employed, with an emphasis on utilizing high-precision carrier phase measurements. Specifically, through the use of double-difference measurements as discussed in Section III.5.3, it becomes feasible to estimate the baseline vector between two antennas, subsequently enabling the determination of the platform orientation [129]. Another category of methods operates within the measurement domain, incorporating orientation parameters into the carrier phase observation model. This allows for the direct solving of orientation parameters based on ambiguity resolution [128].

IV.3.3 Light Detection And Ranging (LiDAR)-based

The acquisition of orientation angles can be achieved through the utilization of LiDARs [130]. The operational approach involves the installation of LiDARs, typically two in number. One LiDAR is positioned overhead, primarily employed for detecting the horizontal position, while the second LiDAR is installed at the bottom to scan the vertical position [131]. In a similar work, two LiDARs were employed alongside an IMU, with the IMU primarily serving to stabilize the LiDAR measurement plane [132].

IV.3.4 Inertial Measurement Unit

While vision-based orientation estimation offers detailed information, it is susceptible to limitations imposed by environmental factors such as rain, fog, and dust. These conditions can alter the accuracy and reliability of vision sensors in estimating orientation. Similarly, LiDAR-based orientation estimation encounters challenges, as the effective application range

of LiDAR is restricted. Furthermore, LiDAR systems generate large-size datasets, imposing a considerable computational burden on data processing. In the case of GNSS-based orientation estimation, the method is dependant on satellite availability, making it susceptible to signal blockages or interruptions. Moreover, it is noteworthy that GNSS systems typically operate at a low data rate, further influencing the overall responsiveness of orientation estimation in dynamic scenarios.

In contrast, Inertial Measurement Units (IMUs) stand out for their self-reliance, as they do not depend on external parameters. IMUs, composed of accelerometers, gyroscopes, and magnetometers, provide high rate data on linear acceleration, angular velocity, and magnetic field strength and direction, enabling robust and independent orientation estimation across diverse environmental conditions [133].

In certain studies, the term IMU is used to describe a system containing only accelerometers and gyroscopes, while the terms Magnetic, Angular Rate, and Gravity (MARG) or Magnetic and Inertial Measurement Unit (MIMU) encompass systems that include accelerometers, gyroscopes in addition to magnetometers [134]. However, in our work, we adopt the term IMU to be equivalent to MARG and MIMU, encompassing all three sensors.

Also, the term Attitude and Heading Reference System (AHRS) is occasionally used interchangeably with IMU. However, it is crucial to emphasize the distinction between these terms. While the two sensors utilize the same set of elementary sensors, including accelerometers, gyroscopes, and magnetometers, IMU solely provides raw measurements from the three sensors without an inherent orientation solution. In contrast, AHRS encompass an embedded orientation solution, offering readily available orientation information.

These sensors consist of either solid-state or Micro-Electro-Mechanical Systems (MEMS) designed to substitute traditional mechanical gyroscopic instruments. MEMS technology has emerged as a compact and cost-effective alternative to conventional solid-state systems. Nevertheless, MEMS-based sensors typically offer estimation solutions with lower accuracy and reliability when compared to those generated from high-grade solid-state sensors [113].

As a result, researchers have been actively engaged in enhancing the performance of solutions relying on low-cost IMUs [135]. By combining the measurements obtained from the three elementary sensors within MEMS-based IMUs, the following section introduces various approaches that leverage these measurements to estimate orientation angles.

IV.4 Algorithms for Orientation Estimation

IV.4.1 IMU Mathematical Model

Before delving into the existing algorithms, it is judged essential to introduce the mathematical model of the IMU. This involves presenting the mathematical model for each of the three sensors [136].

IV.4.1.1 Accelerometer Output Model

The output of the accelerometer at time instant k, represented as $a(k)$, can be expressed as the sum of various components. These include the external non-gravitational acceleration denoted as $nga(k)$, the gravitational acceleration vector denoted as $ga(k)$, the accelerometer bias $b_A(k)$, and a white noise term denoted as $\nu_A(k)$.

$$\begin{aligned} a(k) &= K_A[nga(k) + ga(k)] + b_A(k) + \nu_A(k) \\ nga(k) &= c_a nga(k-1) + \lambda_a(k) \end{aligned} \tag{IV.10}$$

In this equation, K_A represents the scale factor matrix. The external non-gravitational acceleration is characterized as a first-order low-pass filtered white Gaussian noise process $\lambda_a(k)$, where c_a denotes the cut-off frequency of the filter ($0 \leq c_a < 1$).

IV.4.1.2 Gyroscope Output Model

Likewise, the output of the gyroscope at time instant k, represented as $g(k)$, can be formulated as the sum of different elements. These include the true angular velocity denoted as $\omega(k)$, the gyroscope bias $b_G(k)$, and a white noise term $\nu_G(k)$.

$$\begin{aligned} g(k) &= K_G\omega(k) + b_G(k) + \nu_G(k) \\ b_G(k) &= b_G(k-1) + \lambda_b(k) \end{aligned} \tag{IV.11}$$

Here, K_G stands for the scale factor matrix. The gyroscope bias is characterized as a first-order Markov process driven by white Gaussian noise, denoted as $\lambda_b(k)$.

IV.4.1.3 Magnetometer Output Model

Ultimately, the output of the magnetometer at time instant k, represented as $h(k)$, is formulated as the sum of distinct components. These include the true Earth's magnetic field denoted as $m(k)$, where $d(k)$ designates magnetic distortion, and a white noise term denoted as $\nu_M(k)$.

$$\begin{aligned} h(k) &= K_M m(k) + d(k) + \nu_M(k) \\ d(k) &= c_d d(k-1) + \lambda_d(k) \end{aligned} \tag{IV.12}$$

K_M represents the scale factor matrix. The magnetic distortion is characterized as a first-order low-pass filtered white Gaussian noise process, denoted as $\lambda_d(k)$.

As mentioned earlier, in order to enhance the accuracy of estimating the orientation of a rigid body, different fusion techniques can be applied applied using IMU measurements, specifically incorporating angular velocity, linear acceleration, and magnetic field data. This section does not aim to provide an exhaustive review of existing methods but rather focuses on the most commonly utilized ones.

Several studies proposed sensor fusion algorithms, to fuse the estimated orientation with these three sensors data. The most commonly used techniques are Kalman filters (KFs) and Complementary Filters (CFs) [10]. Furthermore, with the advent of recent artificial intelligence (AI) techniques, various approaches based on AI have been suggested for attitude estimation [137].

IV.4.2 Kalman Filters

Originally developed for communication and control applications, the Kalman filter proves to be effective in various applications. It is primarily used to estimate the system state based on multiple data sources that are affected by noise and have a connection to the system state [138].

Let $X_k \in \mathbb{R}^n$ denote the state vector at time k, where n is the system's order. Additionally, $Z_k \in \mathbb{R}^m$ represents the measurement vector at time k, with m being the dimension of the measurement vector.

At time instant k, we have knowledge of the previously estimated state from the preceding step X_{k-1} and the current measurements Z_k. By leveraging these two datasets, KFs can calculate an estimate for the state vector x_k, as depicted in Figure IV.6.

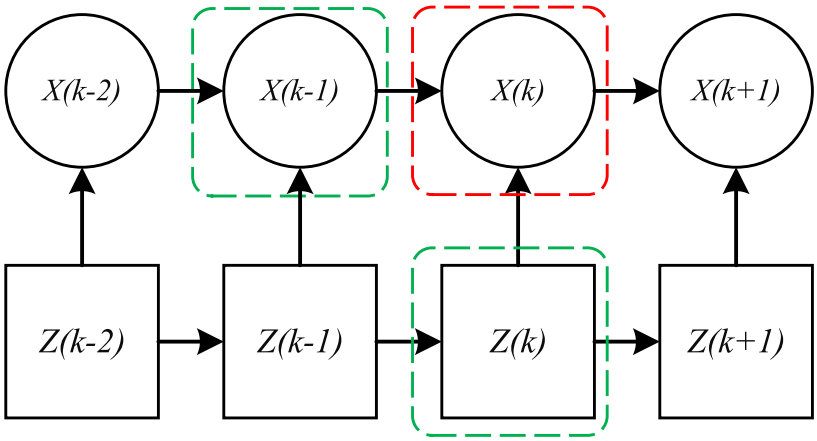


Figure IV.6: Functioning principle of KFs

Strategies employing KFs involve a probabilistic evaluation of the state, modelled as a Gaussian distribution based on the system model [10]. The Linear Kalman Filter (LKF) is optimally applicable only to problems that can be expressed through linear systems. However, a significant number of problems cannot be accurately represented by a linear model. To overcome this limitation, various non-linear techniques based on the Kalman filter have been explored and developed [139].

IV.4.2.1 Linear Kalman Filter (LKF)

Consider the general equations of the state and measurement of the discrete-time linear dynamical system, as shown in relation IV.13.

$$\begin{aligned} X_{k+1} &= AX_k + BU_k + w_k \\ Z_{k+1} &= CX_k + v_k \end{aligned} \tag{IV.13}$$

where U represents any system's external input. The terms w and v denote white Gaussian noise processes that are linked to the system and measurement models, each with respective covariances Q and R.

We define the following probability distributions:

- $p(X_k|X_{k-1})$ is the prediction probability of the future state given the current state;
- $p(Z_k|X_k)$ is the prediction probability of the measurement given the current state.

As previously mentioned, we suppose a Gaussian distribution to represent the system state with a mean μ and a covariance P.

$$p(X_k) = \mathcal{N}(\mu_k, P_k) \tag{IV.14}$$

Building on the relationships given in Equation IV.13 and Equation IV.14, we derive:

$$\begin{aligned} p(X_k|X_{k-1}) &= A\mathcal{N}(\mu_{k-1}, P_{k-1}) + \mathcal{N}(0, Q) \\ p(Z_k|X_k) &= C\mathcal{N}(\mu_k, P_k) + \mathcal{N}(0, R) \end{aligned} \tag{IV.15}$$

By utilizing the properties of Gaussian distributions and after simplification, we obtain:

$$\begin{aligned} p(X_k|X_{k-1}) &= \mathcal{N}(AX_{k-1}, AP_{k-1}A^T + Q) \\ p(Z_k|X_k) &= \mathcal{N}(CX_k, CP_kC^T + R) \end{aligned} \tag{IV.16}$$

By applying Bayes' theorem which allows to determine conditional probability $p(A|B) = \frac{p(B|A)p(A)}{p(B)}$, we obtain:

$$p(X_k|Z_k, X_{k-1}) = \frac{p(Z_k|X_k, X_{k-1})p(X_k|X_{k-1})}{p(Z_k)} \tag{IV.17}$$

By using the Maximum a posteriori estimation method, an optimal estimation of the state vector $\hat{X}_k$ along with the covariance matrix $\hat{P}_k$ can be determined. Overall, the LKF consists of two main steps: the prediction step and the correction step.

During the prediction step, the filter estimates the next state $\hat{X}$ and its covariance $\hat{P}$ at time k, based on the previous state at time $k-1$ using relation IV.18. Subsequently, the correction step refines this estimation using a set of measurements at time k, as illustrated in relation IV.19.

$$\begin{aligned} \hat{X}_k &= AX_{k-1} + BU_k \\ \hat{P}_k &= AP_{k-1}A^T + Q_k \end{aligned} \tag{IV.18}$$

$$\begin{aligned} X_k &= \hat{X}_k + K_k(Z_k - C\hat{X}_k) \\ P_k &= \hat{P}_k - K_k(C\hat{P}_kC^T + R)K_k^T \\ K &= \hat{P}_kC^T(C\hat{P}_kC^T + R)^{-1} \end{aligned} \tag{IV.19}$$

where K is denoted as the Kalman gain.

Given the specific problem under consideration, the state vector is defined to align with the details of the situation. Consecutively, LKF as well as its variants were proposed for estimating orientation in various scenarios, as demonstrated in the studies presented [140–143].

IV.4.2.2 Extended Kalman Filter (EKF)

In this section, we will present the most well-known non-linear algorithm derived from the Kalman filter that will be applied to the orientation estimation problem, being Extended Kalman filter (EKF). The EKF stands out as one of the widely utilized non-linear filtering approaches [139].

For non-linear KFs, we consider the general equations governing the state and measurement of a discrete-time non-linear dynamical system, as shown in relation IV.20.

$$\begin{aligned} X_{k+1} &= f(X_k, U_k) + w_k \\ Z_{k+1} &= h(X_k) + v_k \end{aligned} \tag{IV.20}$$

This method involves conducting a first-order Taylor series expansion of the state and measurement models, thereby obtaining linearized models suitable for the application of Kalman Filter equations [144].

Similar to the LKF, the set of equations encapsulating the EKF algorithm is divided into two main steps: the prediction step and the correction step, as outlined in relations IV.21 and IV.22, respectively.

$$\begin{aligned} \hat{X}_k &= f(X_{k-1}, U_k) \\ \hat{P}_k &= F(X_{k-1}, U_k) P_{k-1} F^T(X_{k-1}, U_k) + Q_k \end{aligned} \tag{IV.21}$$

$$\begin{aligned} X_k &= \hat{X}_k + K_k(Z_k - h(X_k) \\ P_k &= [I - K_k H(X_k)]\hat{P}_k \\ K &= \hat{P}_k H^T(X_k)(H(X_k)\hat{P}_k H^T(X_k) + R)^{-1} \end{aligned} \tag{IV.22}$$

where the matrices F and H are the jacobians of f and h, respectively and are obtained using:

$$\begin{aligned} F(X_{k-1}, U_k) &= \frac{\partial f(X_{k-1}, U_k)}{\partial x} \\ H(X_k) &= \frac{\partial h(X_k)}{\partial x} \end{aligned} \tag{IV.23}$$

The EKF algorithm block scheme is illustrated in Figure IV.7. A notable characteristic of this filter, in contrast to other non-linear filters, is its straightforward implementation and computational efficiency. However, it may not be well-suited for highly non-linear models [139]. Numerous studies utilizing the EKF for orientation estimation can be found in the literature [145–148].

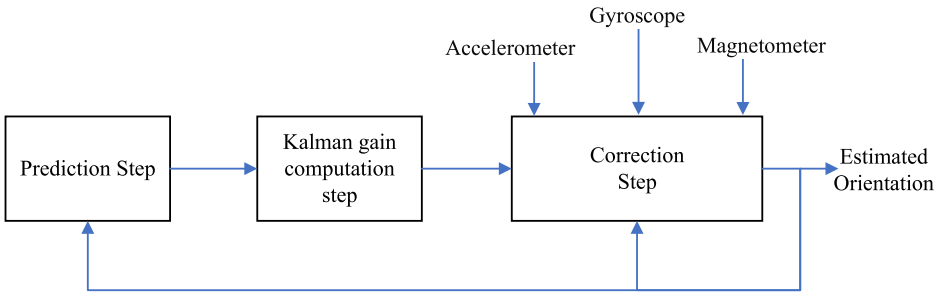


Figure IV.7: Block diagram of EKF algorithm

IV.4.2.3 Other Non-linear Kalman Filters

Another notable alternative is the quaternion EKF, which employs the EKF to estimate orientation represented in quaternion form. In this approach, it initially predicts the new state by utilizing measurements from the gyroscopes. Subsequently, it refines this state

by incorporating measurements from the accelerometers and magnetometers. Instances of utilizing the Quaternion EKF can be found in references [149–151].

Furthermore, it's noteworthy to mention that several non-linear filters, distinct from the EKF, have been proposed for orientation estimation, and we will highlight a few of them. To address the inherent linearization errors in the EKF, an alternative approach is the Unscented Kalman Filter (UKF). Essentially, the UKF propagates the state distribution through the system dynamics using a deterministic sampling approach. This distribution is represented by a minimal set of carefully chosen sample points, known as sigma points. These sigma points enable the capture of the true mean and covariance of the state, contributing to enhanced accuracy in certain scenarios [152]. The primary drawback of the UKF in comparison to the EKF is its tendency to degrade computational efficiency [139].

An additional notable technique is the Cubature Kalman Filter (CKF). Built on the numerical-integration perspective of Gaussian filters, the CKF employs a third-degree spherical-radical cubature rule for the numerical computation of Gaussian-weighted integrals. By employing a set of cubature points with equal weight, the CKF calculates means and covariances of state variables [153].

IV.4.3 Complementary Filters

The Complementary Filters present a valid alternative to KF-based methods due to their simplicity and effectiveness. Based on frequency domain analysis, these filters combine signals to provide an orientation estimation without relying on statistical descriptions [154].

They earn their name due to their unique way of combining the strengths of different sensors to overcome their individual limitations. The IMU sensors offer complementary frequency responses. Accelerometer excels at capturing high-frequency dynamics due to its fast response, while the gyroscope provides accurate information at lower frequencies where its drift is less dominant [155].

In essence, the name complementary filter accurately reflects its core principle of combining the complementary characteristics of different sensors to create a more robust and accurate estimation of the system state, specifically the orientation in our case.

In contrast to Euler Angles, which may encounter Gimbal lock issues and ambiguous representations, quaternion-based complementary filters offer an additional advantage by avoiding singularities through the use of quaternions as the representation form [155]. It is important to note that there is always the option to convert from quaternions to Euler angles through appropriate mathematical transformations, as detailed in section IV.2.3.5.

While various complementary filters have been developed for orientation estimation [156], two of the most widely used and well-known options are Madgwick filter [157] and Mahony Filter [158].

IV.4.3.1 Madgwick Filter

The Madgwick algorithm is a widely used method that uses accelerometer and magnetometer measurements to compensate for errors in the gyroscope measurements. The gyroscope, accelerometer and magnetometer measurements about the x, y and z axes of the sensor frame can be arranged into a quaternion form denoted

$$\begin{aligned} {}^{S}g &= [0, g_x, g_y, g_z] \\ {}^{S}a &= [0, a_x, a_y, a_z] \\ {}^{S}h &= [0, h_x, h_y, h_z] \end{aligned} \tag{IV.24}$$

Madgwick Filter includes three main steps. The initial step involves computing the rate of change, using gyroscope measurements denoted as ${}^{S}_{E}\dot{q}_{g,k}$. It can be calculated as shown in relation IV.25 [157].

$${}^{S}_{E}\dot{q}_{g,k} = \frac{1}{2}\,{}^{S}_{E}\hat{q}_{est,k-1} \otimes {}^{S}g_k \tag{IV.25}$$

Here, ${}^{S}_{E}\hat{q}_{est,k-}$ represents the normalized estimated quaternion at the preceding step $k-1$. It is essential to note that the pre-subscript indicates the source coordinate frame, while the pre-superscript indicates the destination coordinate frame. Additionally, the symbol $\otimes$ signifies a quaternion product.

In the second step, the Madgwick filter utilizes a gradient descent algorithm to compute orientation increment derived from accelerometer and magnetometer measurements. In this process, two reference vectors E_a and E_m, respectively for acceleration and magnetic field, are employed to correct the deviation of the algorithm. E_m vector can be calculated as stated in [159]. E_a is defined as $E_a = [0, 0, 0, g]$, where g is the acceleration due to gravity ($g = 9.8\ \mathrm{m \cdot s^{-2}}$). The orientation increment ${}^{S}_{E}\dot{q}_{\nabla,k}$, computed based on accelerometer and magnetometer measurements (${}^{S}a_k$ and ${}^{S}h_k$) is outlined in relation IV.26.

$$\begin{aligned} {}^{S}_{E}\dot{q}_{\nabla,k} &= \frac{J_k^T F_k}{\|J_k^T F_k\|} \\ F_k &= \begin{bmatrix} {}^{S}_{E}q_{k-1}^{-1} \otimes E_{a,k} \otimes {}^{S}_{E}q_{k-1} - {}^{S}a_k \\ {}^{S}_{E}q_{k-1}^{-1} \otimes E_{a,k} \otimes {}^{S}_{E}q_{k-1} - {}^{S}h_k \end{bmatrix} \end{aligned} \tag{IV.26}$$

where J_k is the Jacobian matrix of the function F_k.

In the third step, a fusion process, controlled by the parameter β, refines the orientation change estimated from gyroscope measurements by incorporating the orientation increment derived from accelerometer and magnetometer measurements. Subsequently, an integration process yields an estimate of the quaternion at the instant k, as described in relation IV.27.

$$\begin{aligned} \dot{q}_k &= {}^{S}_{E}\dot{q}_{g,k} - \beta\, {}^{S}_{E}\dot{q}_{\nabla,k} \\ q_k &= q_{k-1} + \dot{q}_k \Delta T \end{aligned} \tag{IV.27}$$

where β is the divergence rate of the Madgwick filter.

To mitigate numerical issues arising from the finite resolution of numerical representations, the Madgwick algorithm employs quaternion normalization. The block diagram of the Madgwick algorithm is depicted in Figure IV.8. For an in-depth formulation of this algorithm, refer to [157].

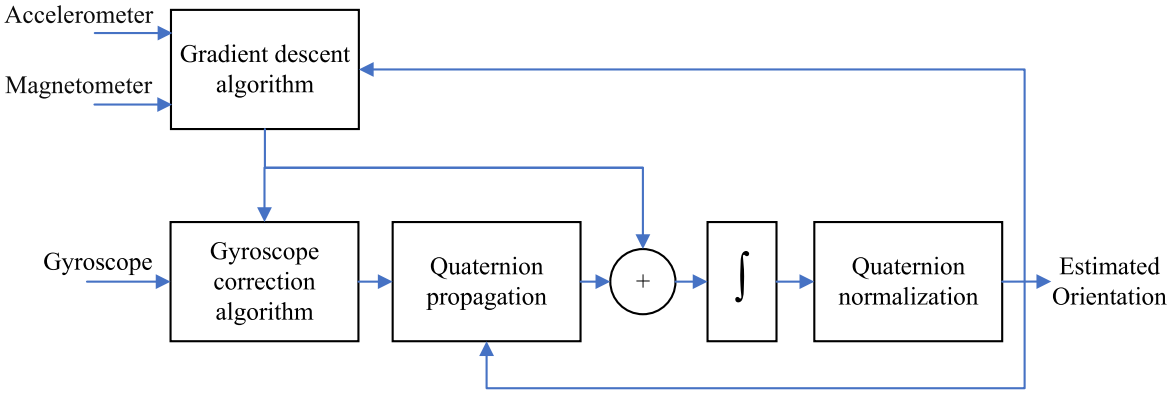


Figure IV.8: Block diagram of Madgwick filter

IV.4.3.2 Mahony Filter

Starting with the estimated orientation computed in the previous step of the algorithm, an orientation error is determined by calculating the cross product between the estimated direction and the measured direction of gravity. Additionally, this error includes the cross product between the estimated magnetic field and the measured magnetic field.

Let v denotes the estimated direction of gravity and w denotes the estimated magnetic field. The orientation error term, denoted e, can be obtained using relation IV.28.

$$\begin{aligned} e &= a \cdot v + h \cdot w \\ v &= 2 \begin{bmatrix} q_1q_3 - q_0q_2 \\ q_0q_1 + q_2q_3 \\ q_0q_0 - q_1q_1 - q_2q_2 + q_3q_3 \end{bmatrix} \\ w &= 2 \begin{bmatrix} b_x(0.5 - q_2q_2 - q_3q_3) + 2b_z(q_1q_3 - q_0q_2) \\ b_x(q_1q_2 - q_0q_3) + 2b_z(q_0q_1 + q_2q_3) \\ b_x(q_0q_2 + q_1q_3) + 2b_z(0.5 - q_1q_1 - q_2q_2) \end{bmatrix} \end{aligned} \tag{IV.28}$$

Here, the terms a and h denote accelerometer and magnetometer measurements, respectively. The values of b_x and b_z are calculated based on the prior estimation of the orientation, coupled with the magnetometer measurements.

Following the integration of the error term, leading to the term e_{int}, this error is employed to adjust the measured angular velocity computed by the gyroscope. This correction is governed by a Proportional-Integral (PI) controller, utilizing the parameters K_p and K_i, as described in Equation IV.29.

$$g = g + K_p e + K_i e_{int} \tag{IV.29}$$

Based on the corrected angular velocity, the estimation of orientation change can be derived using Equation IV.25. Similar to the Madgwick algorithm, the Mahony algorithm aincorporates quaternion propagation and normalization steps to estimate the orientation, ensuring its validity as a representation. The block diagram of the Mahony algorithm is illustrated in Figure IV.9, and a comprehensive formulation can be found in [158].

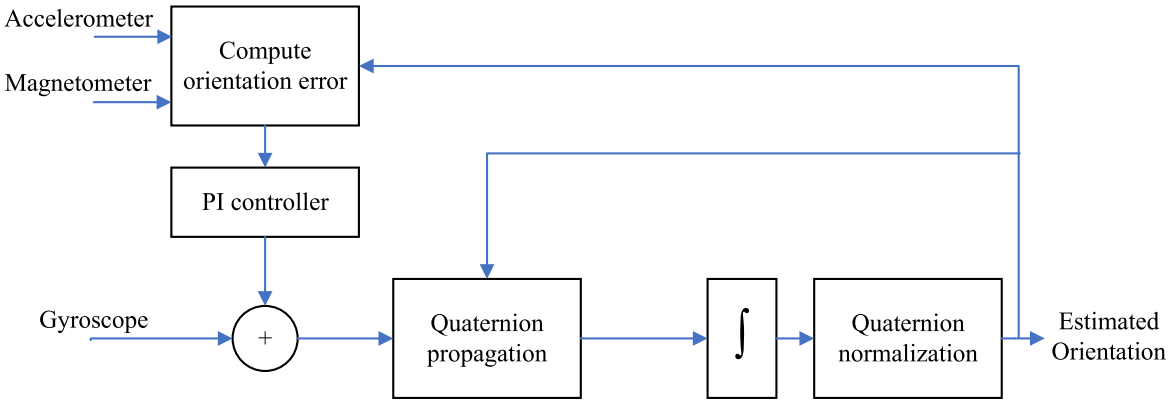


Figure IV.9: Block diagram of Mahony filter

IV.4.4 Neural Networks

While KF-based and CF-based solutions demonstrably attain high accuracy in diverse orientation estimation applications, achieving optimal performance necessitates a rigorous approach to parameter selection. This encompasses covariance matrices in KF methods, fusion weights in CFs, and potentially other critical parameters depending on the chosen method.

Numerous studies has demonstrated the potential of Neural Networks (NNs) in providing data-driven solutions to problems that have conventionally been tackled by model-based approaches. This shift towards data-driven approaches has been facilitated by the increasing availability of large datasets and advancements in computational power [137].

NNs have versatile applications across various scenarios, as illustrated in Figure IV.10. For example, they can serve as augmented solutions to conventional methods, leading to potentially superior performance. In [160], a Recurrent Neural Network (RNN) is employed to process raw gyroscope and accelerometer data, thereby mitigating modeling errors and enhancing sensor fusion capabilities. Similarly, in another study [161], a NN is employed to identify and filter out noise associated with IMU measurements.

Furthermore, NNs have been utilized to calibrate the outputs of IMU sensors in various studies. For instance, the work presented in [162] proposed a method to

generate compensation components for gyroscope measurements, while in [163] a similar approach in introduced for magnetometer measurements. Additionally, another study presented a calibration method based on a back-propagation neural network for temperature compensation. This method is particularly useful as temperature variations significantly impact the performance of MEMS-based IMU sensors [164].

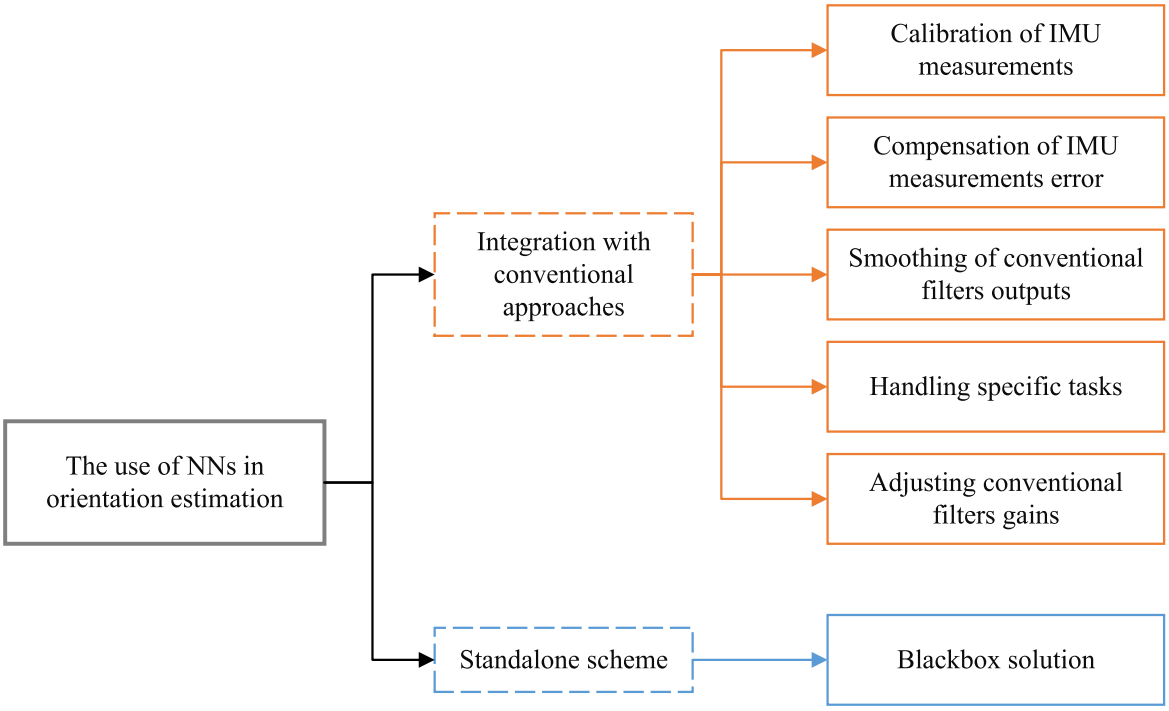


Figure IV.10: A block diagram that describes the use of NNs in orientation estimation

An alternative strategy involves refining the output of conventional filters. For instance, in [165], a feed-forward NN is employed to enhance the smoothness of the Kalman filter's output. Additionally, in [166], the outputs of a CF are employed to train a NN using a supervised approach, utilizing the Bayesian Regularization Backpropagation algorithm. Furthermore, NNs can be leveraged for temporal orientation integration, exemplified by the approach proposed in [167].

Moreover, NNs can be applied to adjust various gains and parameters within conventional filter solutions, as demonstrated in [168]. They proposed the utilization of a long short-term memory (LSTM) network to support an iterative indirect Kalman filter in estimating disturbances. This approach matches the system noise covariance to the strength of perturbation and adapts to the measurement noise covariance.

NNs exhibit further versatility in orientation estimation by not only augmenting existing methods but also handling specific tasks within the estimation process. One approach involves employing NNs for temporal integration of orientation data, as demonstrated in the work presented in [167].

The use of NNs extends beyond their integration with existing approaches and can be used as a standalone solution. NNs can be used as a blackbox solution using directly the output of the IMU's sensors. For instance, [169] introduced RIANN (Robust IMU-based Attitude Neural Network), which is a NN-based orientation estimator that have demonstrated superior performance compared to conventional approaches across various

applications, motion characteristics and sampling rates. In a similar work, a LSTM-NN was proposed for orientation estimation based on data collected during the test flight of a quadrotor [170]. Another notable recent work consists of a convolutional neural network coupled with a LSTM-NN, followed by a feedforward NN, designed to estimate quaternions using 6DoF IMU measurements [171].

IV.4.5 Discussion

Researchers have developed numerous Sensor Fusion Algorithms to estimate orientation using IMU sensors, with KFs and CFs being among the most commonly utilized ones. Studies have highlighted the significance of parameter selection in these filters to achieve satisfactory performance, regardless of their filtering class or mathematical formulation [154].

Furthermore, the research concluded that there isn't a universally optimal filter applicable to all conditions. Instead, the performance of each filter is strongly influenced by the specific experimental conditions. This variability in experimental conditions explains the disparate results reported regarding the performance of sensor fusion algorithms in various studies [136].

Another crucial aspect to consider when comparing these algorithms is their computational efficiency. CFs have been observed to outperform KFs in terms of speed. This observation finds support in the mathematical implementation of the filters [154]. Indeed, the Madgwick and Mahony algorithms exhibit very similar processing times, making them suitable for small embedded processors.In contrast, the EKF has a runtime nearly six times higher [105].

On the other hand, NNs or, more broadly, AI-based techniques offer promising prospects for real-time orientation estimation based on inertial sensors. However, to attain optimal performance, it is imperative to understand their strengths and limitations. Careful consideration of data availability, computational resources, and specific needs is essential when deciding whether to employ NNs instead of conventional methods.

IV.5 Conclusion

In conclusion, this chapter has provided insights into the representation of orientation in three-dimensional space, emphasizing the complexities involved in capturing rotational motions accurately. We have explored various methods for representing orientation and highlighted the most commonly used ones.

Moving forward, our exploration extends to the realm of sensors utilized for orientation estimation, with a particular focus on IMUs. Additionally, we have delved into the algorithms commonly employed with IMUs, highlighting Kalman filters and complementary filters as the predominant methods. However, it's important to recognize that no single filter proves optimal across all scenarios.

In the upcoming chapter, we will introduce a neural network-based approach aimed at addressing a specific aspect, namely tilt-compensation in yaw estimation. Subsequently, we will compare this proposed method with two well-established and commonly utilized complementary filters: the Madgwick filter and the Mahony filter.

Chapter V

A Machine Learning-based Method for Tilt Compensation in Yaw Estimation

V.1 Introduction

While IMUs offer an attractive solution for orientation estimation due to their compactness and self-containment, the accuracy of their yaw angle estimation exhibits lower accuracy compared to pitch and roll [11].

Yaw estimation presents challenges due to its susceptibility to external magnetic fields, such as those caused from nearby metallic objects. This complicates the magnetometer's role in accurately determining yaw. Employing sensor calibration techniques reduce biases and enhances long-term accuracy, underscoring the critical importance of calibration in obtaining accurate magnetometer readings.

Another difficulty arises when the sensor is not aligned parallel to the Earth's surface. In such cases, a conventional tilt compensation method is typically employed. In this chapter, we will evaluate the effectiveness of this conventional method.

Following the assessment outcomes, we intend to introduce an artificial neural network (ANN) as a solution to tackle the tilt compensation challenge in yaw estimation. Additionally, we will compare the effectiveness of our proposed method with two established complementary filters (CFs): the Madgwick filter and the Mahony filter.

V.2 Magnetometer Measurements Calibration

Low-cost sensors, including magnetometers, often encounter inaccuracies resulting from manufacturing limitations such as offset error, sensitivity error, cross-axis sensitivity errors, and sensor measurement noise. However, the primary sources of errors impacting magnetometer measurements are typically perturbations induced by ferromagnetic materials

and electromagnetic systems in the sensor's proximity [172]. These perturbations are commonly classified as hard and soft iron errors.

For a tri-axis magnetometer, the ideal response is a spherical outcome centered at the origin. Hard iron perturbations consist of constant or slowly time-varying magnetic fields produced by magnetized materials or external magnets in the vicinity of the sensor. Consequently, this shifts the magnetic sphere response away from the origin [173]. Conversely, soft iron effects arise from metallic materials like nickel batteries, causing the ideal spherical response to distort into an elliptical shape [11].

A commonly employed technique for calibrating magnetometer readings involves moving the sensor in a figure-eight pattern, noting the minimum and maximum readings across all three axes. These recorded values are subsequently utilized to compute offset values (X_{off}, Y_{off} and Z_{off}) and scale factors (X_{sf}, Y_{sf} and Z_{sf}), as shown in relation V.1. Then, using relation V.3, calibrated magnetometer measurements can be obtained enabling the re-centering and rescaling of the magnetometer response [174].

$$\begin{aligned} Delta_X &= (max(h_x) - min(h_x))/2 \\ Delta_Y &= (max(h_y) - min(h_y))/2 \\ Delta_Z &= (max(h_z) - min(h_z))/2 \\ Delta &= (Delta_X + Delta_Y + Delta_Z)/3 \\ X_{sf} &= Delta/Delta_X \\ Y_{sf} &= Delta/Delta_Y \\ Z_{sf} &= Delta/Delta_Z \\ X_{off} &= (max(h_x) + min(h_x))/2 \\ Y_{off} &= (max(h_y) + min(h_y))/2 \\ Z_{off} &= (max(h_z) + min(h_z))/2 \end{aligned} \tag{V.1}$$

$$\begin{aligned} h_{xCal} &= X_{sf} \times h_x - X_{off} \\ h_{yCal} &= Y_{sf} \times h_y - Y_{off} \\ h_{zCal} &= Z_{sf} \times h_z - Z_{off} \end{aligned} \tag{V.2}$$

Experimental data collection in this chapter involves utilizing the MPU9250 9 DoF motion sensor, depicted in Figure V.1, in conjunction with the Raspberry Pi 3b+ compute module. Detailed information about the Raspberry Pi module can be found in Section III.6.3.

The MPU9250 9 DoF motion sensor serves as an IMU, integrating a 3-axis accelerometer, a 3-axis gyroscope, and a 3-axis AK8963C magnetometer. Each sensor's outputs are digitized using 16-bit analog-to-digital converters. The accelerometer can measure ranges of ±2g, ±4g, ±8g, and ±16g, the gyroscope can measure ±250°/s, ±500°/s, ±1000°/s, and ±2000°/s, while the magnetometer can measure up to ±4800 μT [175].

Interfacing the MPU9250 with the Raspberry Pi 3b+ compute module is accomplished via the I2C protocol. The sampling rate for accelerometer and gyroscope data is configured at 1 KHz, while for magnetometer measurements, it is set to 100 Hz. The wiring diagram detailing the connection between the MPU9250 and the Raspberry Pi 3b+ compute module is provided in Figure V.2. The calibration procedure's outcomes are visualized in Figure V.3.

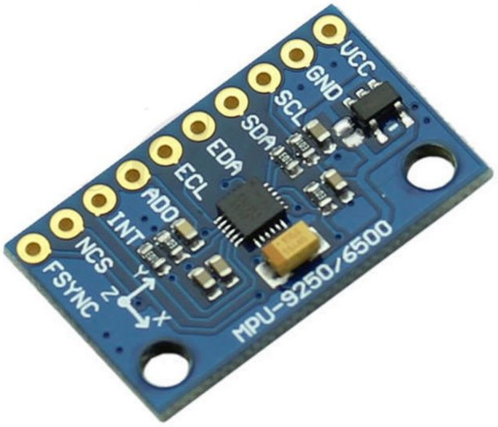


Figure V.1: MPU9250 9 DoF motion sensor

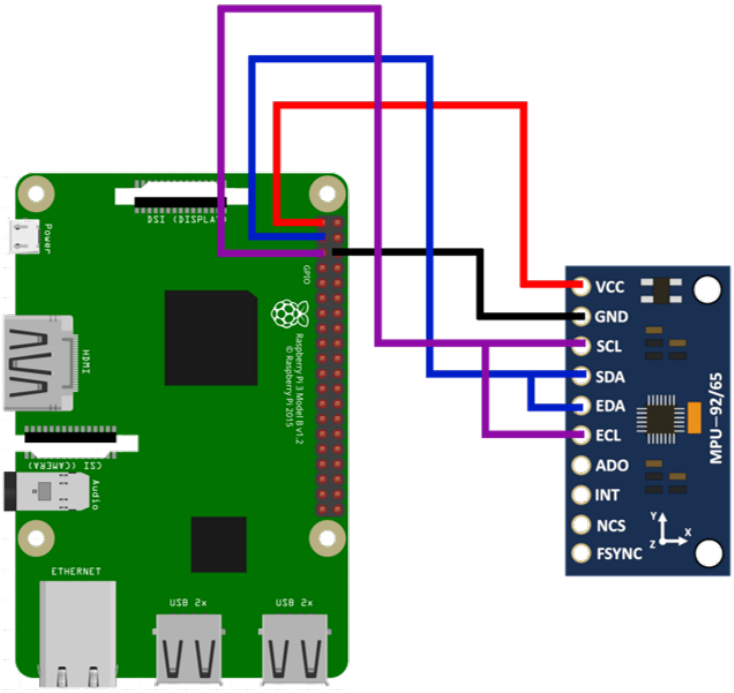


Figure V.2: Raspberry Pi 3b+ and MPU9250 module wiring

V.3 Conventional Tilt compensation Method

V.3.1 Description of the Conventional Tilt Compensation Method

In the previous chapter, we explored various sensor fusion algorithms capable of estimating orientation angles. Notably, yaw estimation can be achieved solely through the utilization of magnetometers which enable the measurement of the surrounding magnetic field. Under ideal conditions, free from magnetic disturbances or with an ideally calibrated magnetometer, it becomes possible to accurately measure the Earth's magnetic field. This measurement serves

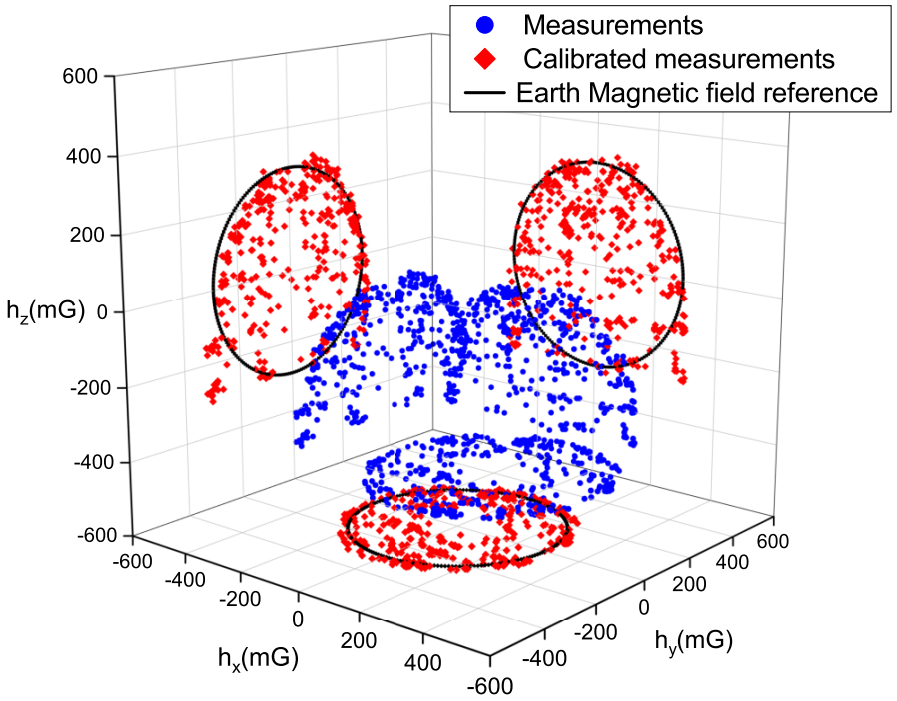


Figure V.3: Magnetometer measurements calibration

as the foundation for determining the angle between the sensor's longitudinal axis and the magnetic north direction.

The magnetic field of the Earth possesses a horizontal component that always aligns with the magnetic north direction. This characteristic enables the calculation of yaw by considering its horizontal components, as indicated by relation V.3.

$$\psi = \begin{cases} 90, & \text{if } H_x = 0 \text{ and } H_y < 0 \\ 270, & \text{if } H_x = 0 \text{ and } H_y > 0 \\ 180 - tan^{-1}(\frac{H_y}{H_x}) \times \frac{180}{\pi}, & \text{if } H_x < 0 \\ -tan^{-1}(\frac{H_y}{H_x}) \times \frac{180}{\pi}, & \text{if } H_x > 0 \text{ and } H_y < 0 \\ 360 - tan^{-1}(\frac{H_y}{H_x}) \times \frac{180}{\pi}, & \text{if } H_x > 0 \text{ and } H_y > 0 \end{cases} \tag{V.3}$$

Here, H_x and H_y represent the horizontal projections of the Earth's magnetic field.

If the sensor is parallel to the ground, then pitch and roll angles would both be zero and yaw can be directly calculated using relation V.3.

In situations where the sensor aligns parallel to the ground, resulting in zero pitch and roll angles, determining yaw becomes straightforward, relying solely on the horizontal components of the magnetic field. However, in practical scenarios such as when magnetometers are mounted on moving vehicles, they are most often not parallel to the Earth's surface. To address this, a conventional tilt compensation method is commonly utilized. This method involves projecting the measurements obtained from the tri-axis magnetometer onto a horizontal plane to account for the tilt angle.

In Figure V.4, the magnetometer axes coincide with the body frame comprising three orthogonal axes. Within this frame, the x-axis aligns with the direction of forward motion, the z-axis points downward, and the y-axis is perpendicular to the plane formed by the x and z axes. The terms hx, hy, and hz denote the magnetometer measurements along the axes of the body frame. By incorporating information about the sensor's tilt angles, we can calculate the projections of the magnetic field onto the horizontal plane defined by the X and Y axes using relation V.4.

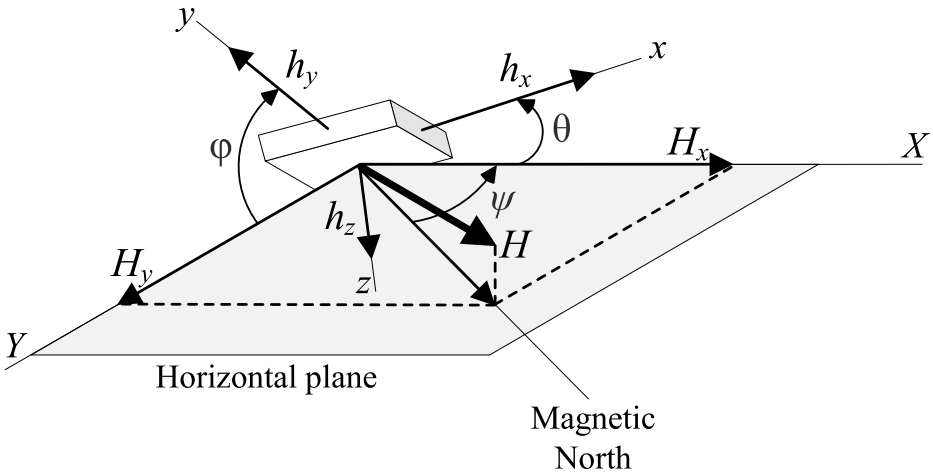


Figure V.4: Yaw determination using a tri-axis magnetometer

$$\begin{pmatrix} H_x \\ H_y \end{pmatrix} = \begin{pmatrix} cos\theta & sin\theta sin\phi & -sin\theta cos\phi \\ 0 & cos\phi & sin\phi \end{pmatrix} \begin{pmatrix} h_x \\ h_y \\ h_z \end{pmatrix} \tag{V.4}$$

where θ and ϕ denote pitch and roll angles, respectively.

It worth noting that other tilt compensation techniques have been documented in the existing literature. For instance, a smartphone-based pedestrian dead reckoning solution that relies on an adaptive tilt compensation method for precise yaw angle estimation were proposed in [176]. Another alternative was introduced in [177] where a probabilistic approach using data from accelerometers and magnetometers were used for tilt compensation.

V.3.2 Assessment of the Conventional Tilt Compensation Method

V.3.2.1 Pitch and Roll Estimation

To effectively implement the conventional tilt compensation method, it is imperative to accurately estimate both pitch and roll angles. To this end, we employ a 3D non-magnetic scaled platform, depicted in Figure V.5. This platform enables the adjustment of pitch and roll angles within a range of $-60°$ to $60°$, while the yaw angle can be set across the full $360°$ range. Importantly, the use of this platform does not result in any magnetic interference, specifically concerning magnetometer measurements.

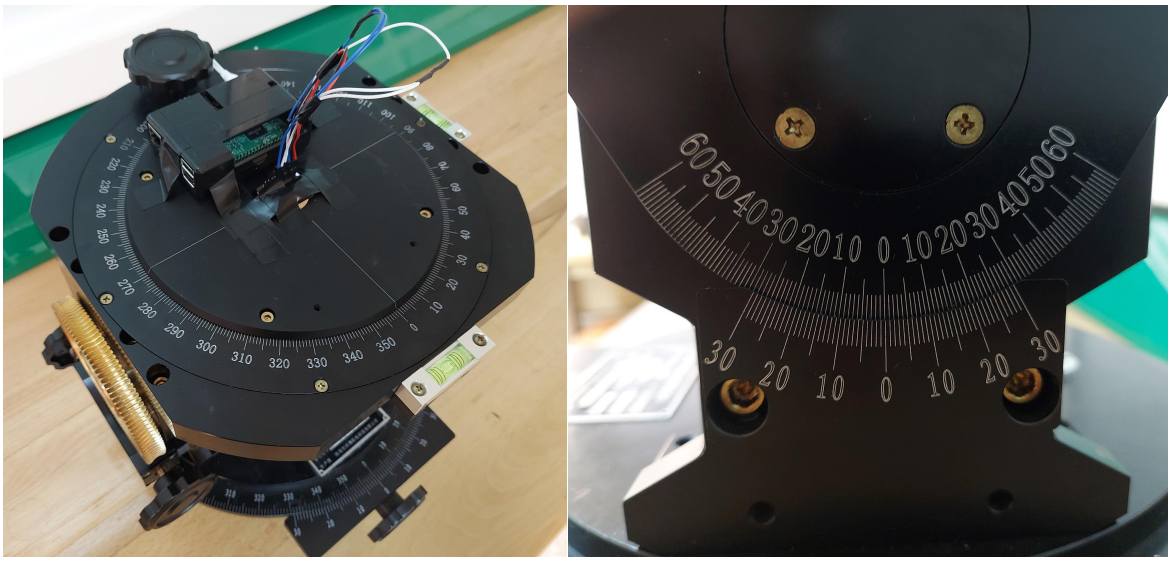


Figure V.5: 3D non-magnetic scaled platform

Here, we opt to employ the Madgwick and Mahony filters, introduced in Section IV.4.3, for pitch and roll estimation. This decision primarily originates from their efficient computational performance, which, despite being relatively low, still maintains a comparable level of accuracy to Kalman Filters.

We configured pitch and roll angles within the range of $-60°$ to $60°$, with increments of $5°$. The outcomes obtained revealed similar performance for both filters. Notably, it is essential to perform calibration due to the MPU9250 module's imperfect alignment parallel to the ground. Following calibration, the estimated pitch and roll angles using both the Madgwick and Mahony filters are depicted in Figure V.6 and Figure V.7, respectively.

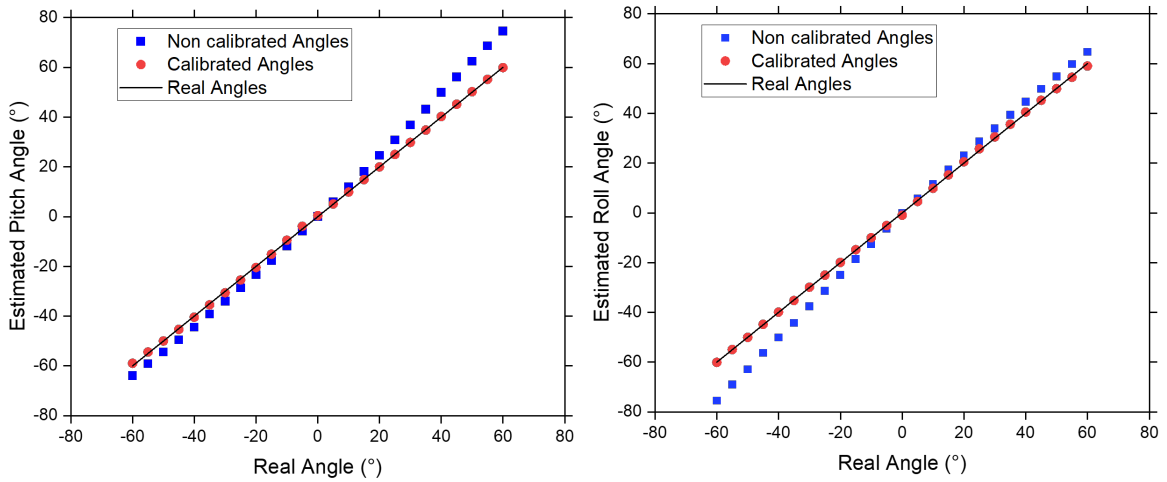


Figure V.6: Pitch and roll estimation results with Madgwick filter

V.3.2.2 Assessment with MPU9250

In this section, we present the experimental evaluation of the conventional tilt compensation method, conducted using the MPU9250 module. To perform these experiments, we make use of relations V.3 and V.4, and employ the 3D non-magnetic scaled platform.

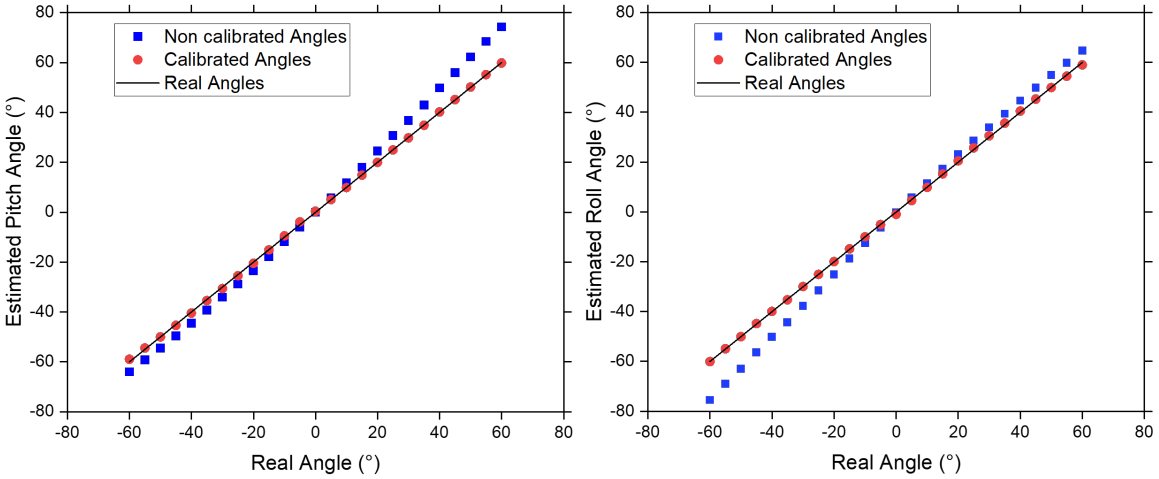


Figure V.7: Pitch and roll estimation results with Mahony filter

We set various yaw angles ranging from 0° to 355° in increments of 5°, and for each of these yaw values, we set different pitch angles spanning from −60° to 60°. The results obtained, as depicted in Figure V.8, indicate that the yaw estimation error may reach up to ±30°.

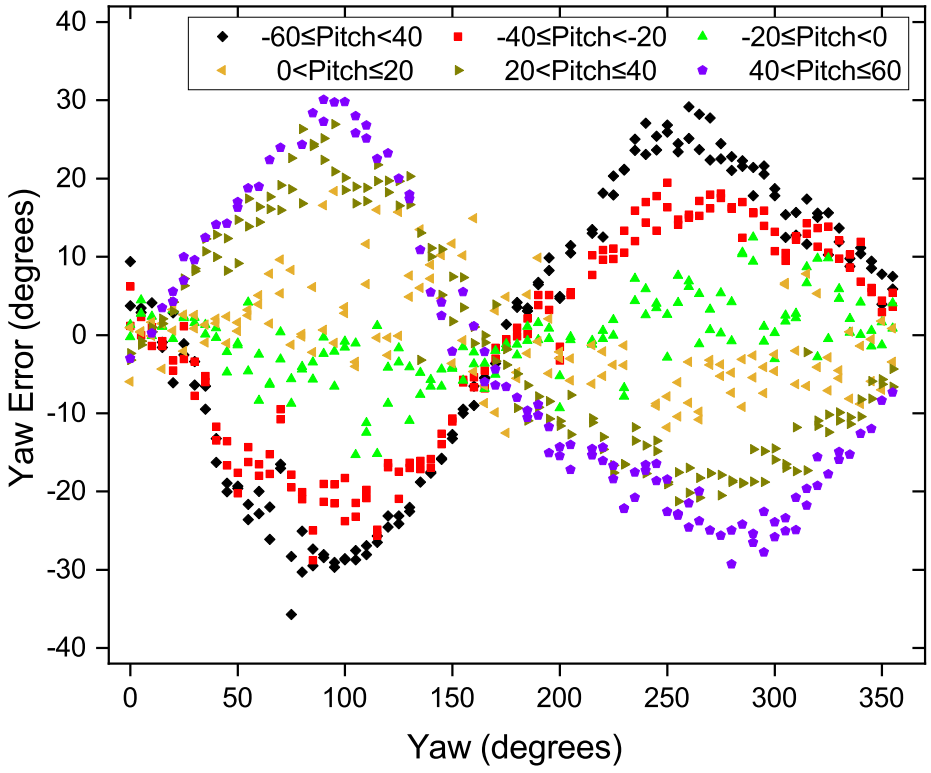


Figure V.8: Conventional tilt compensation method assessment with MPU9250

V.3.2.3 Assessment with Samsung Galaxy M51

The results obtained from the assessment of the conventional tilt compensation method using the MPU9250 module led us to consider the possibility that the inferior outcomes were due

to a faulty implementation of the tilt compensation method. Seeking additional validation, we opted to replicate the tests using the Samsung Galaxy M51 smartphone, which features a built-in magnetic compass.

Using the 3D non-magnetic scaled platform, we set different yaw angles from 0° to 315° with a 45° step. For each yaw value we set different pitch angles from −60° to 60° with a 20° step and record the estimated yaw angles using the Compass Galaxy Application, as shown in Figure V.9. The results obtained are illustrated in Figure V.10.

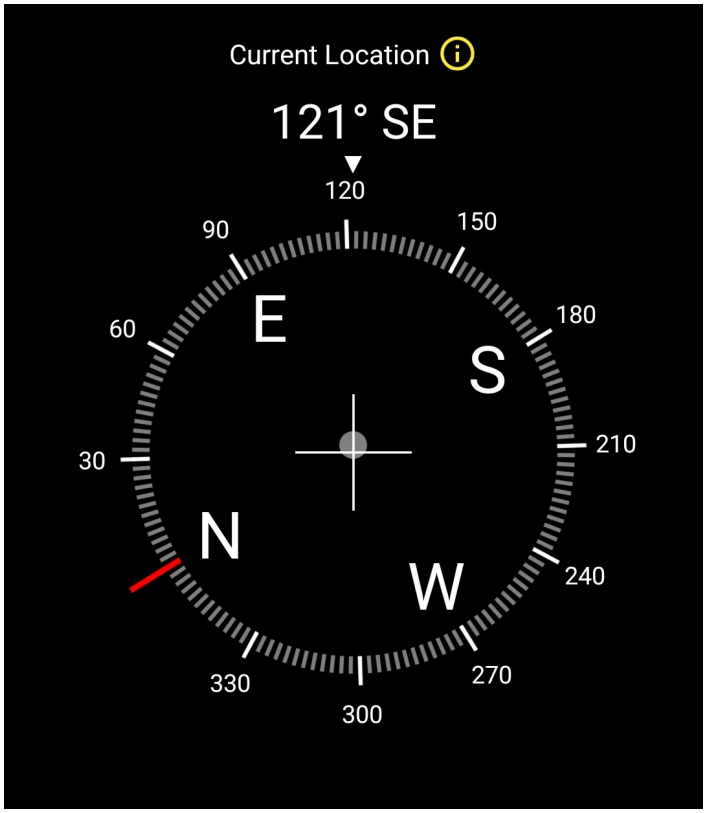


Figure V.9: Compass Galaxy application within the Samsung Galaxy M51 smartphone

The experiments conducted with both the MPU9250 and Samsung Galaxy M51 smartphone produced similar results. Notably, we observed that the error in yaw estimation was found to be dependant on the actual yaw angle, exhibiting smaller errors when the sensors were pointing towards the north or south, and larger errors when directed towards the east or west. Furthermore, we found that the errors were less critical for smaller tilt angles but became more significant as the tilt angles increased.

V.4 Solution Approach

Despite being widely used in the literature [178–181], the performed experiments have revealed the shortcomings of this conventional approach. Consequently, we opted to introduce a novel machine learning (ML)-based method for tilt compensation in yaw estimation, using measurements from a low-cost IMU.

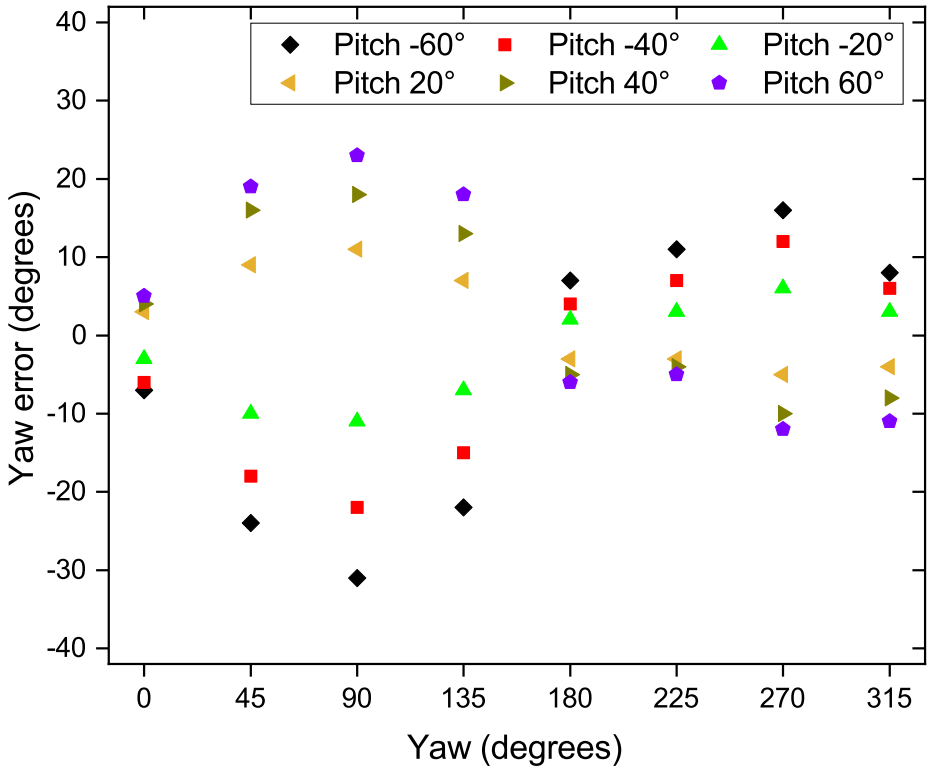


Figure V.10: Conventional tilt compensation method assessment with Samsung Galaxy M51 smartphone

V.4.1 Motivation

The estimation of the yaw angle is a regression problem, which revolves around predicting a continuous response from a given set of inputs. Various regression techniques have been proposed in the literature for this purpose. According to the comparative study conducted by [182], Artificial Intelligence (AI)-based algorithms perform better than traditional methods in this context.

Although the terms AI and ML are frequently used interchangeably, it is crucial to distinguish between the two. ML is a subset of AI, focusing on developing methods for machines that enable them to identify patterns and make predictions. On the other hand, AI encompasses a broader scope, referring to machines' ability to emulate human decision-making processes, as outlined by [183].

Various non-linear ML algorithms have been employed to address regression problems. These encompass well-known methods such as, Neural Networks (NNs), Random Forest (RF), K-Nearest Neighbor (KNN) and Support Vector Regression (SVR). Notably, NNs have emerged as primary tools for achieving satisfactory results, as demonstrated by the comparative studies conducted in [184] and [185]. Hence, in our study, we have opted to utilize one of the variations of NNs, namely the Artificial Neural Network (ANN).

ANNs consist of interconnected nodes, termed artificial neurons, that are designed to mimic the behaviour of the human brain. Within ANNs, signals propagate between neurons, with inputs processed through a combination of weights and biases.

ANNs exhibit a high potential in learning and modeling non-linear and complex relationships between variables. They also possess the ability to generalize and provide predictions for new unseen datasets. ML utilize two primary learning methodologies: unsupervised learning, which uncovers hidden features in input data, and supervised learning, which uses a known set of input-output pairs to train models, as highlighted in [186]. The current study proposes the use of a Multilayer Perceptron (MLP) ANN regressor to estimate the yaw angle, regardless of whether or not there is tilt. It involves of a Feed-Forward NN that processes inputs only in the forward direction, employing a supervised learning approach.

V.4.2 Inputs and Outputs Selection

The selection of input data for the proposed ANN was guided by the fundamental principles governing yaw angle measurement. Specifically, in accordance with relation V.3, the determination of yaw angle relies on the horizontal components of the magnetic field. Relation V.4 further establishes the connection between these components and the readings from the magnetometer (h_x, h_y, and h_z), as well as the tilt of the current sensor, which can be approximated using accelerometer data (a_x, a_y, and a_z). Consequently, our proposed ANN utilizes calibrated measurements from both the magnetometer and accelerometer along the three axes as input features, as illustrated in Figure V.11.

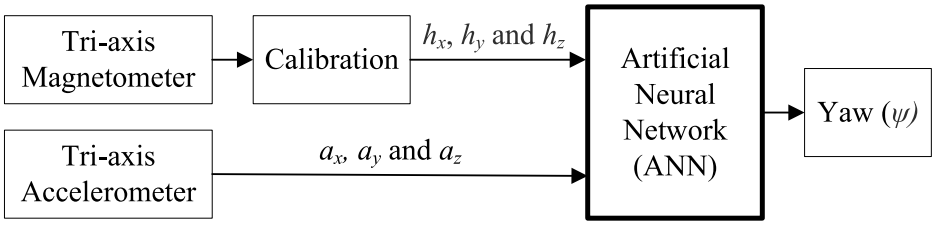


Figure V.11: Inputs and outputs of the adopted ANN model

V.4.3 Dataset Collection

Using the 3D non-magnetic scaled platform, we set different yaw values from 0° to 359° with a 1° step. For each yaw value, we rotate the platform arbitrary along X and Y axes. At a sample rate of 10 Hz, a total of 206300 samples have been recorded, each of which includes the following data:

- The actual yaw value read from the 3D non-magnetic scaled platform, used to label the collected features;
- The calibrated magnetometer measurements along the three axes;
- The accelerometer measurements along the three axes.

As mentioned earlier, other sensor fusion algorithms for attitude estimation can intrinsically address the problematic of tilt compensation in yaw estimation, such as Madgwick and Mahony filters. These two filters are one of the most efficient algorithms for orientation estimation. Consequently, we incorporate them into our study, implementing and

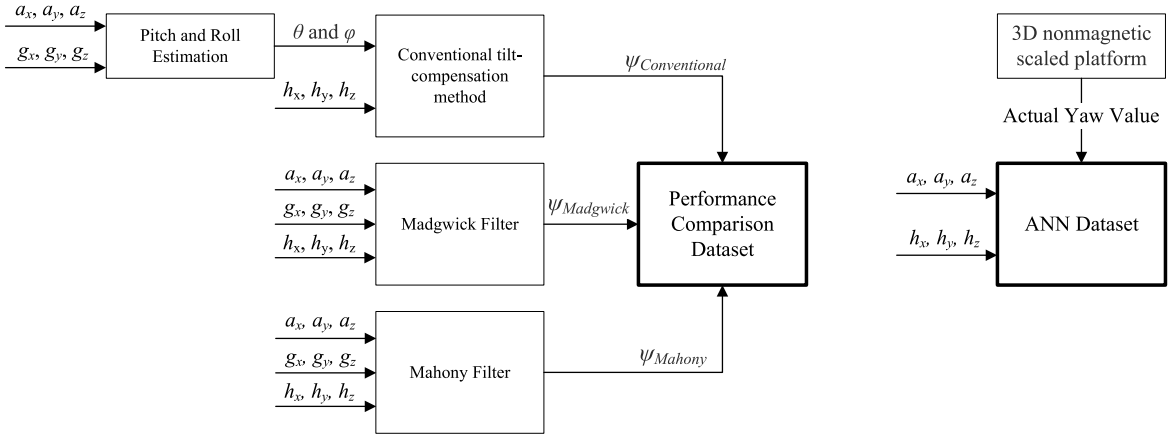


Figure V.12: High-level block scheme describing the dataset collection process

recording their outcomes for comparison with our proposed solution. Figure V.12 provides an overview of the dataset collection process.

It is important to note that both the Madgwick and Mahony filters are constant gain filters. Therefore, their performance is dependant on the selected gain value. In order to provide a fair qualitative comparison, we chose the gains that minimize the Root Mean Square Error (RMSE) of the estimation for each filter.

In the Madgwick filter, the only tunable parameter β serves as a trade-off factor which determines when the gyroscope measurements take over accelerometer measurements. Additionally, it is necessary to define the initial estimates for both attitude and biases. Assuming the sensor is at rest, the initial attitude can be set to zero. As for biases, they are determined by averaging samples collected while the IMU is stationary.

Within the Mahony filter, increasing the proportional gain, K_p, enhances the system's ability to respond to noise. However, an excessively large K_p can induce oscillations in the estimation process. Conversely, the integral component accumulates the error term over time, causing even minor errors to gradually increase the integral component. In our study, we employ a very small value for K_i to mitigate this effect.

V.4.4 ANN architecture and Training

The architecture of a neural network plays a crucial role in its performance. The configuration of input and output layers is directly related to the number of features and outputs, which, in our case, are 6 and 1, respectively. However, there is no one-size-fits-all solution for defining the best internal architecture, as it depends on the specific problem at hand and the data available. A typical strategy involves beginning with a basic architecture and gradually increase its complexity and explore various combinations of parameters like the number of hidden layers and neurons, activation functions, and optimization algorithms until desirable performance is attained.

It is crucial to consider a trade-off between model complexity and generalization capability. A model that is too simple may under-fit the data, leading to poor performance.

On the other hand, an excessively complex model may excel in fitting the training data but struggle to generalize well to new, unseen data.

Prior to training the ANN, the collected dataset goes through a pre-processing. During this stage, the output is scaled to align with the range of the chosen activation function on the output layer [187]. Additionally, given the different scales of accelerometer and magnetometer measurements, it is advisable to normalize input variables. This operation ensures that each input feature contributes equally in the learning process, preventing features with larger scales from dominating the learning process [188, 189].

In our work, we start with a simple ANN featuring a single hidden layer. Subsequently, we aim to enhance accuracy by experimenting with varying sizes and depths of the ANN. Utilizing the *Google Colab* environment and *Python* programming language, as illustrated in Figure V.13, an optimization algorithm is employed to adjust the ANN's weights and biases based on a suitable metric, known as the loss function. In our case, we opt for the mean squared error (MSE) between the ANN predicted output and the actual output. Figure V.14 provides a summary of the training process of ANN. Table V.1 contains some of the results obtained through different ANN architectures.

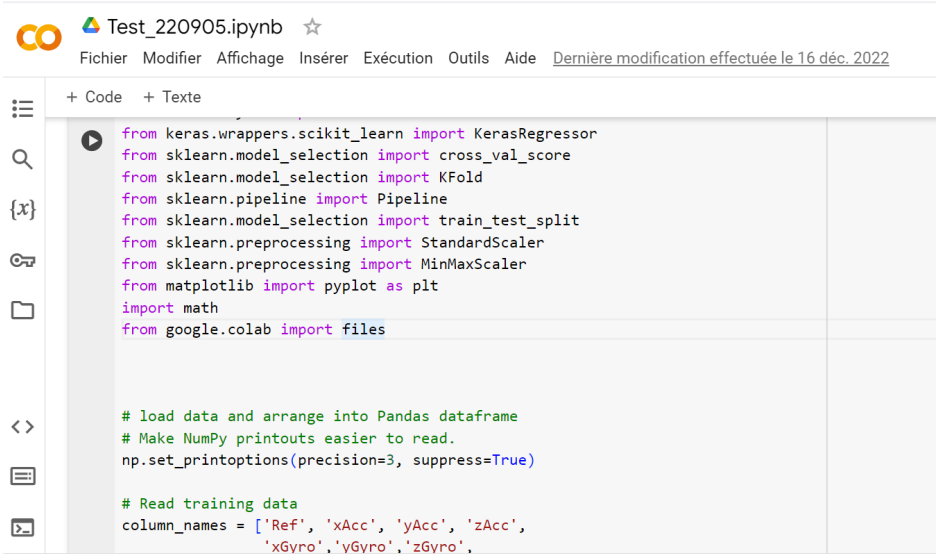


Figure V.13: *Google Colab* environment and *Python* programming language

Table V.1: Some of the obtained results using different ANN architectures

Architecture	Trainable parameters	Training MSE (deg^2)	Test MSE (deg^2)	Training max error (deg)	Test max error (deg)	Number of iterations
[254]	2033	7.97	8.29	64.41	64.54	1000
[12,6]	169	4.72	4.51	132.12	28.03	1000
[24,12]	481	3.98	4.01	33.95	20.00	830
[12,6,4]	195	3.69	3.79	13.79	11.98	610
[12,12,12]	409	3.87	3.90	18.32	8.20	450
[24,12,4]	**525**	**3.73**	**3.79**	**8.79**	**8.72**	**120**
[24,12,4,4]	545	3.68	3.71	9.12	7.58	110

To tackle the issue of overfitting, we employed a widely-used technique called k-fold cross-validation. This method involves dividing the training dataset into k subsets, or folds, where one fold is reserved for validation while the remaining $k-1$ folds are utilized for training

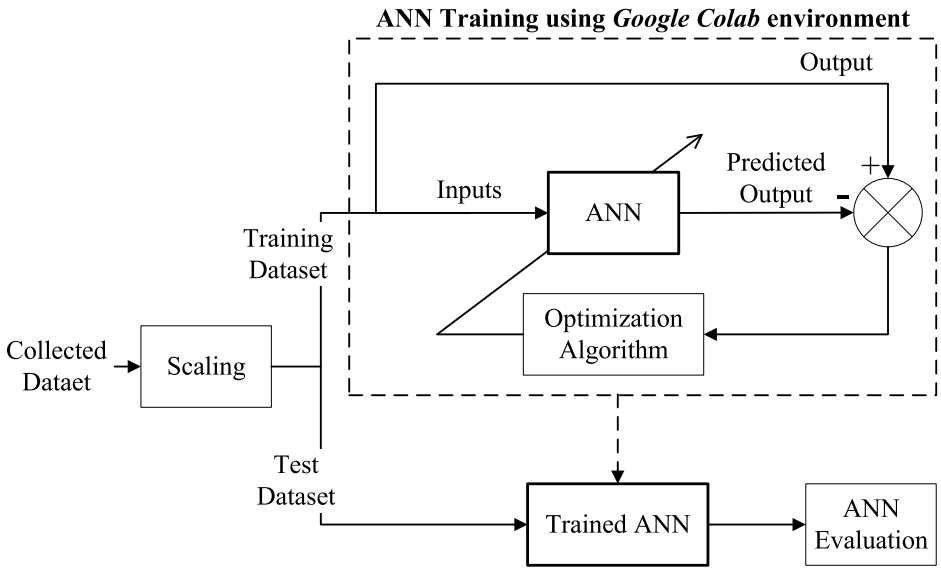


Figure V.14: Scheme of ANN training process

the model. This procedure is repeated k times, ensuring each fold serves as the validation set exactly once. The final evaluation metric is then calculated as the average of the metrics obtained across all folds [186].

We observed that increasing the number of hidden layers beyond two did not yield significant improvements in the MSE. However, employing three hidden layers notably reduced the maximum error on both training and test datasets. While it's generally acceptable to use the same number of neurons for all hidden layers [186], our experimentation revealed that employing a larger first layer followed by smaller subsequent layers led to superior performance in our case. Optimal results were achieved with three hidden layers comprising 24, 12, and 4 neurons, as illustrated in Figure V.15. These findings are summarized in Figure V.16, where all parameters are normalized for visualization in the same 3D graph.

The choice of activation functions significantly influences the properties and performance of ANNs, as they are responsible in introducing non-linearity to the network. While the sigmoid function is commonly employed for this purpose [190], we have tested in our work several activation functions and the best performance was attained using the hyperbolic tangent (tanh) function for all layers.

The tanh function is an activation function that is renowned to perform well in many applications, particularly in image and speech recognition. It exhibits smoothness, continuity, and differentiability, mapping inputs to a range between -1 and 1. Unlike the sigmoid function, the tanh function yields a zero-centered output, facilitating convergence during the training phase. Its effectiveness in deep learning scenarios, where networks with multiple hidden layers are used to learn complex representations of the input data, has been well-documented [191]. Therefore, the selection of the tanh activation function in our study is not surprising, given our utilization of a neural network with multiple hidden layers to learn a complex mapping between the sensor measurements and the yaw angle.

For the optimization algorithm, we employed two well-known algorithms; Stochastic Gradient Descent (SGD) and Adaptive Moment Estimation (Adam). Unlike the traditional

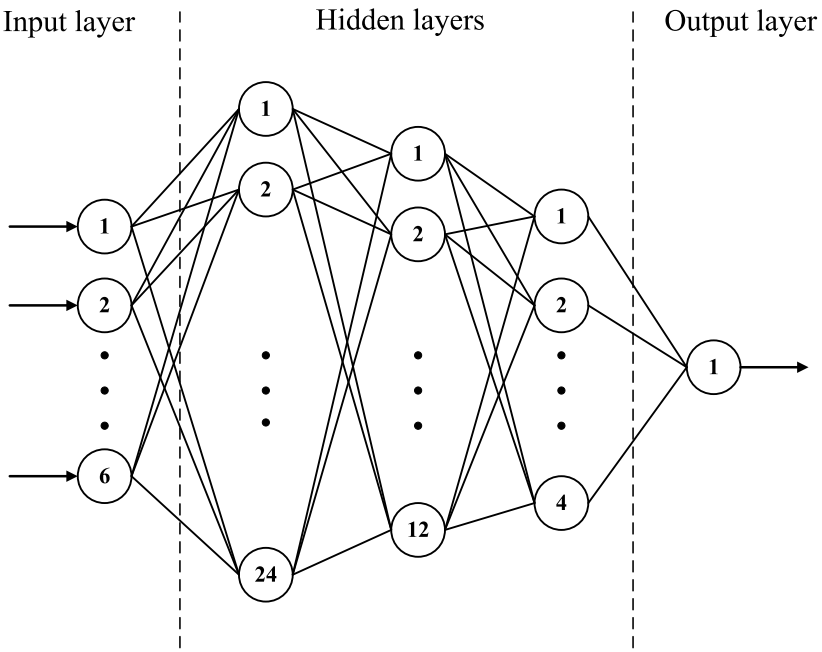


Figure V.15: ANN's adopted architecture

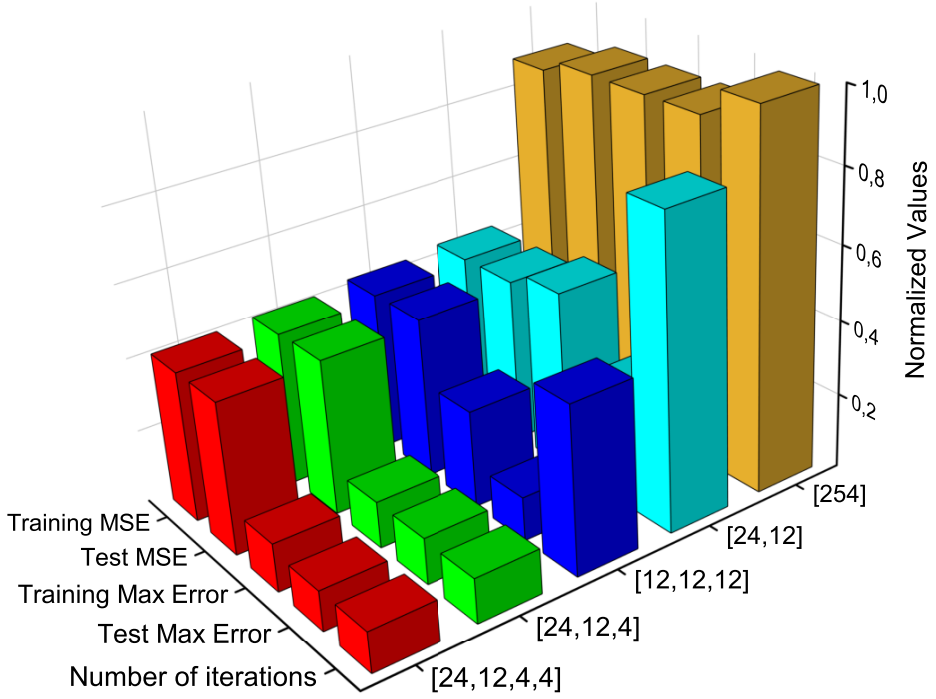


Figure V.16: Performance comparison between different ANN architectures

Gradient Descent, SGD does not iterate over the entire training set to update parameters at each iteration. Instead, it tracks the negative gradient of the loss function after encountering either a single sample or a small set of samples. Thus, SGD tackles the issue of the high computational cost. However, the primary challenge with SGD lies in selecting an appropriate learning rate, where a small rate results in slow convergence, while a large one can cause the loss function to fluctuate around the minimum or even to diverge [192].

The Adam algorithm addresses this concern by calculating adaptive learning rates for

each parameter. It achieves this by estimating the first and second moments of the gradient, allowing Adam to utilize a larger effective step size [193]. Figure V.17 depicts the training loss at each epoch with the two algorithms. Both algorithms have converged to the same optimal solution with a noticeably quick convergence for Adam optimizer.

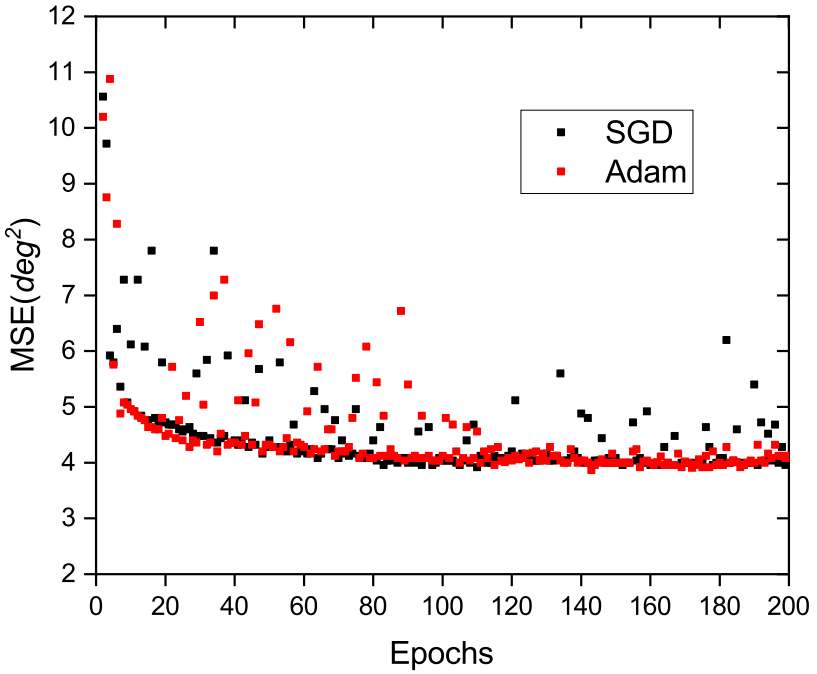


Figure V.17: Training loss history with Adam and SGD optimizers

V.5 Results and Discussion

Table V.2 presents the statistical outcomes obtained from for the evaluation of the trained ANN using the test dataset, which constitutes 20% (41260 samples) of the entire collected dataset. The RMSE and the maximum error metrics of the four methods were computed to evaluate the effectiveness of the trained model.

Table V.2: Statistical results and computational time of the four methods

Method	**RMSE** (deg)	**Maximum error** (deg)	**Average execution time** (μs)
Conventional	10.42	54.28	5.99
Madgwick	6.10	40.93	130.83
Mahony	7.92	55.74	76.11
ANN	**1.95**	**8.72**	**3578.82**

Based on the findings, the RMSE of the proposed ANN, which measures the dispersion of estimation errors, is relatively smaller in comparison to alternative methods. This suggests that the trained ANN demonstrates high accuracy in predicting output values for new, unseen inputs. While the maximum measured error is approximately 8°, signifying instances where predictions deviate considerably from actual values, it still represents a noticeable enhancement compared to other methods whose maximum error exceeds 40°.

Figure V.18 showcases the Cumulative Distribution Functions (CDFs) of the yaw estimation error obtained by the different approaches using the testing dataset. Interestingly, over 70% of error occurrences yielded by the ANN are below 2°. Conversely, conventional tilt compensation method, Madgwick, and Mahony filters exhibit comparable performances with over 30% of error occurrences exceeding 5°, as depicted in Figure V.19, which outlines the yaw estimation error statistics obtained by the four methods.

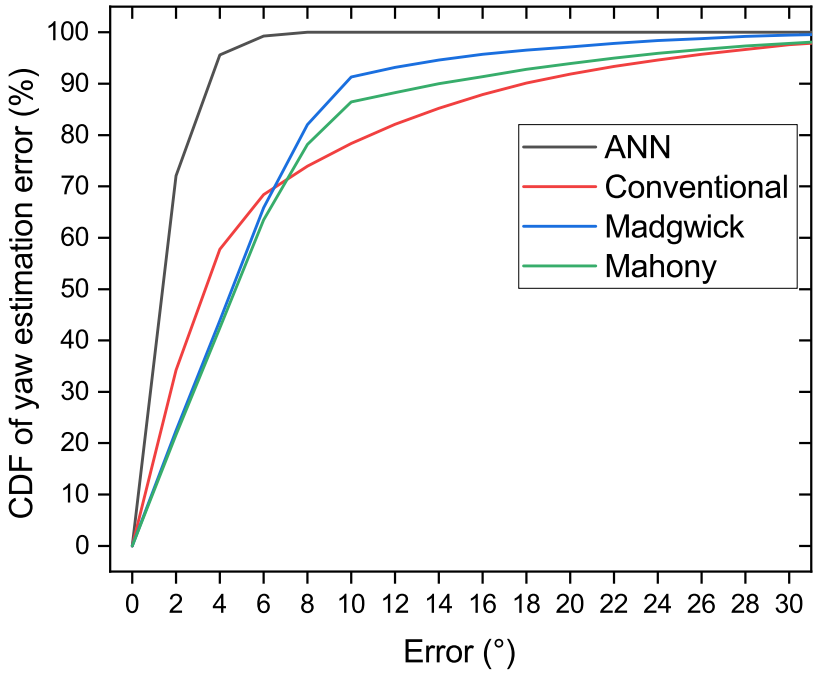


Figure V.18: CDFs of yaw estimation error obtained by the four methods

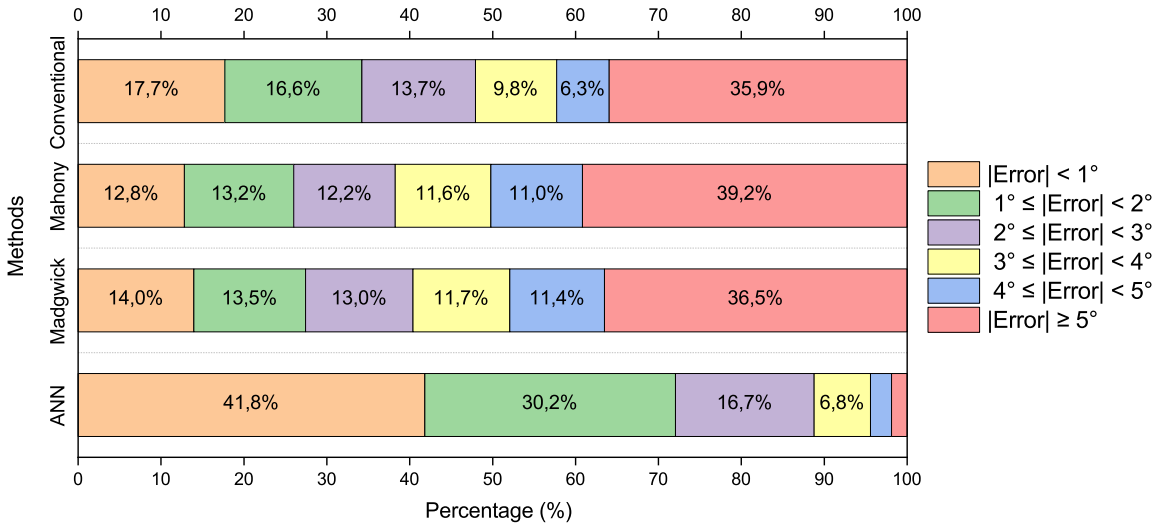


Figure V.19: Histograms of the four methods estimation errors

An examination was conducted to assess the computational efficiency of the four methods. The trained ANN was implemented on the Raspberry Pi 3b+ utilizing the *TensorFlow* library. The findings of this analysis are detailed in Table V.2, which presents the corresponding execution times for each of the four methods. It was noted that the proposed ANN necessitates a considerably longer processing time compared to the other three methods. Specifically, the runtime of the ANN was estimated to be approximately 3 ms, whereas the execution times for the two CFs and the conventional tilt compensation method were observed

to be around 100 μs and 10 μs, respectively.

To visually depict these results, Figure V.20 is presented. It offers a concise overview of the comparisons among the four methods. All parameters have been normalized to facilitate clearer visualization within a single 3D graph.

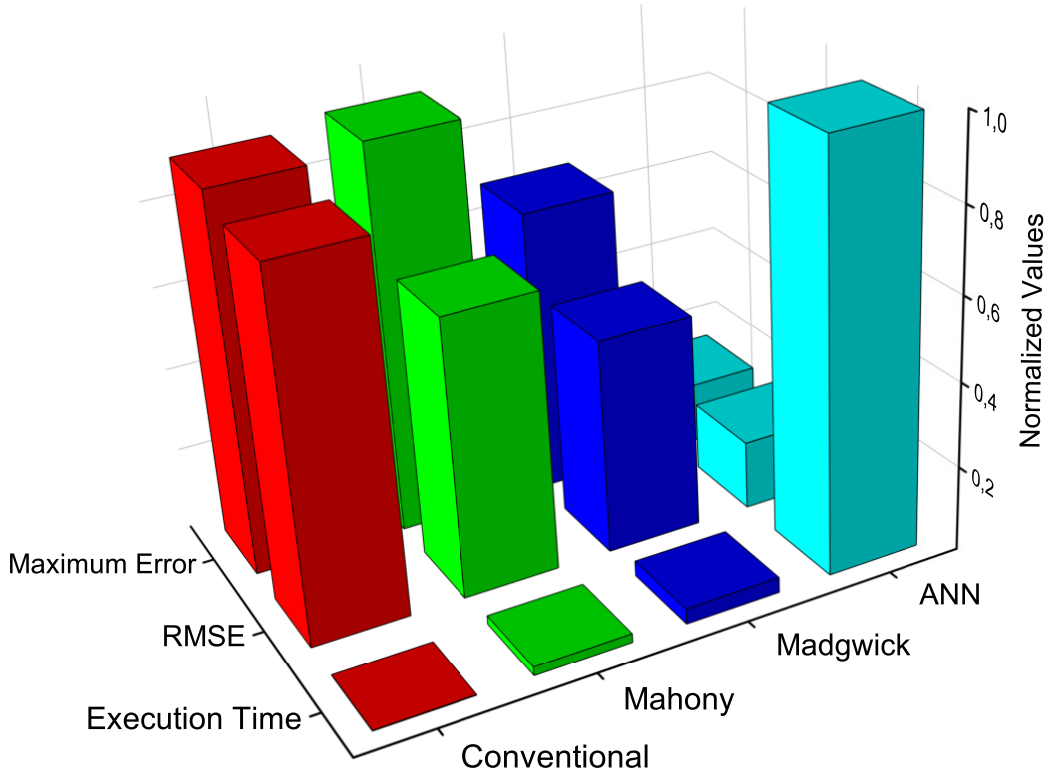


Figure V.20: Performance comparison summary

In summary, our proposed ANN demonstrates superior accuracy in comparison to the conventional tilt compensation method, Madgwick, and Mahony filters. Nonetheless, this superior performance comes at the cost of a more complex system, leading to extended computational time. Hence, while our approach excels in accuracy, it may not be the optimal choice for applications prioritizing real-time processing or low computational requirements.

However, there remain several limitations that need to be tackled to enhance the effectiveness and generalization capabilities of our proposed solution. A primary challenge in ML-based approaches is the availability of large and diverse datasets. Although we employed a relatively large dataset for training, its limited diversity may influence the ANN's performance on unseen scenarios. To address this concern, we plan to use a pan-tilt unit for precise positioning in two axes, enabling precise data labelling for training in both static and dynamic modes.

While our proposed ANN can accurately estimate tilt using accelerometer data alone, this method can provide reliable results only when the sensor remains stationary or experiences minimal acceleration. However, in various scenarios, the inclusion of gyroscope data as inputs becomes imperative. Furthermore, our study employed a non-magnetic platform, eliminating interference with magnetometer readings. Yet, in practical applications, magnetic disturbances often emanate from nearby materials and electromagnetic systems.

V.6 Conclusion

In this chapter, we introduce an AI-based approach for addressing one aspect of orientation, specifically tilt compensation in yaw estimation. We initially highlight the limitations of the conventional tilt compensation method and subsequently propose an ANN that utilizes accelerometer and magnetometer measurements as features, eliminating the need for complicated calibration procedures. Notably, our proposed solution eliminates the need to estimate pitch and roll angles.

To achieve optimal outcomes, we explore various ANN architectures and configurations, paying particular attention to the dataset collection process. We then compare the performance of our proposed solution with that of the conventional tilt compensation method and two well-established CFs, namely Madgwick and Mahony filters. Our findings indicate that the proposed solution surpasses existing methods in terms of accuracy, boasting an RMSE of 1.95° and over 70% of error occurrences being below 2°. However, it's worth noting that the ANN's average execution time exceeds that of other methods.

Looking ahead, we aim to further evaluate our proposed solution using dynamic platforms such as Unmanned Aerial Vehicles (UAVs) to conduct additional tests. Furthermore, we intend to implement the proposed ANN on platforms equipped with high-speed parallel data processing capabilities, such as field-programmable gate arrays (FPGAs).

Overall, this chapter presents a promising solution for tilt compensation in yaw estimation utilizing low-cost IMUs and the Raspberry Pi platform. The performance of our proposed solution outperforms that of existing methods in terms of accuracy, and further evaluations are planned to assess its performance in dynamic scenarios.

Chapter VI

Conclusions

Acknowledging the urgent need to enhance productivity, sustainability, and efficiency in our country's agricultural sector, it is imperative for our farmers to adopt modern precision agriculture techniques, which often involve the use of autonomous agricultural vehicles.

This dissertation focuses on two primary aspects related to autonomous agricultural vehicles: position and orientation estimation. Notwithstanding the availability of various solutions on the market, our work aims to develop cost-effective and innovative solutions that are accessible to our farmers. The work presented in this thesis represents a pivotal first step towards the development of accessible solutions for positioning and orientation estimation in agricultural vehicles.

VI.1 Findings and Contributions

VI.1.1 For Positioning

We proposed to explore the potential of employing GPS-based relative positioning approaches for agriculture applications as an alternative to traditional absolute positioning solutions. To achieve this, we implemented three approaches in real-time, namely, Absolute Position Differencing (APD), Pseudorange Single Differencing (PSD), and Pseudorange Double Differencing (PDD), using low-cost modules.

Real-world experiments have been conducted in various settings, including agricultural field, to evaluate the effectiveness of these approaches in typical agricultural environments. The key findings are as follows:

- The PDD approach yielded the most favorable results in agricultural field, with over 97% of estimation errors remaining below 3 m. This represents a significant enhancement in positioning accuracy compared to standalone GPS positioning, which typically offers accuracy within the range of 10 to 15 m when using low-cost single-frequency GPS receivers;

- In regions lacking wide-area DGPS services, like Algeria, the level of accuracy achieved by the PDD approach is comparable to that provided by the Wide Area Augmentation System (WAAS) service within the USA;
- The level of accuracy yielded by the PDD approach enables the effective execution of various operations, including variable-rate application, soil and yield data referencing, tillage, certain types of fertilizer and chemical application, and seeding. However, tasks requiring extremely high accuracy in positioning may pose challenges for the proposed solution.

VI.1.2 For Orientation

Furthermore, beyond the knowledge of the current position, understanding the orientation of agricultural vehicles is fundamental for effective navigation. While existing algorithms have proven to be effective in determining pitch and roll angles, the estimation of the yaw angle presents significant challenges due to various factors.

Our research focuses on one of these factors, specifically tilt compensation in yaw estimation, employing a low-cost IMU. We assess the conventional tilt compensation method and subsequently introduce an AI-based solution, comparing its performance to established methods. The primary findings are outlined below:

- Through a series of experiments, we identify limitations in the conventional tilt compensation method, particularly for large tilt angles and when the IMU is pointing toward the east or west directions;
- We present an innovative machine learning-based approach as an alternative, employing an artificial neural network (ANN) that utilizes accelerometer and magnetometer measurements as input features;
- Our comparative analysis demonstrates that the proposed solution surpasses existing methods in terms of accuracy, achieving an RMSE of 1.95° and with over 70% of errors b being less than 2°. However, it's worth noting that the average execution time of the ANN is higher compared to other methods.

VI.2 Recommendations for Future Work

VI.2.1 For Positioning

Overall, the conducted real-world experiments represent a significant advancement towards actual precision agriculture applications. Hence, our proposed system is expected to serve as a practical positioning solution applicable to both aerial and ground vehicles, particularly in regions where farmers face challenges affording expensive existing positioning solutions. Nevertheless, there is scope for further exploration and improvement to enhance performance in the future.

Our forthcoming efforts will involve a more thorough evaluation of the proposed solution through additional experiments, focusing particularly on high dynamics scenarios. Additionally, we plan to expand our assessment of the low-cost system by incorporating more than two nodes to validate the efficacy of the proposed GPS data transmission approach.

Furthermore, our future work aims to enhance the robustness of the proposed positioning system by incorporating more advanced techniques such as sensor fusion or dead reckoning, particularly in order to tackle the issue of GPS signals discontinuity. Exploring new AI methods to mitigate uncorrelated errors such as receiver noise and multipath interference presents another good option for complementing our existing research.

VI.2.2 For Orientation

One of the significant limitations of the research concerning the tilt-compensation in yaw estimation is the strong dependence on the quality of the dataset used to train and test the ANN. While we employed a relatively large dataset, our intention is to diversify it further by integrating a pan-tilt unit. This device will facilitate precise positioning in two axes, allowing for accurate labeling of data for both static and dynamic modes.

Furthermore, the current implementation of the ANN utilizes accelerometer data as input to capture tilt information. However, this approach may yield reliable results only when the sensor remains stationary or experiences minimal acceleration. In other scenarios, integrating gyroscope data becomes essential. Additionally, our work employs a basic calibration method due to the use of a non-magnetic platform. To address this, we plan to adopt a more sophisticated calibration algorithm capable of mitigating magnetic disturbances commonly encountered from nearby materials and electromagnetic systems.

Additionally, we observed that the ANN has longer computing time compared to other methods. As a result, our future plans involve implementing the proposed ANN on a platform equipped with high-speed parallel data processing capabilities, such as a field-programmable gate array (FPGA). This enhancement aims to optimize computational efficiency and improve overall performance.

Bibliography

[1] The future of food and agriculture-Trends and challenges. Report, Food and Agriculture Organization of the United Nations, 2017.

[2] Pablo Gonzalez-De-Santos, Roemi Fernández, Delia Sepúlveda, Eduardo Navas, and Manuel Armada. Unmanned ground vehicles for smart farms. *Agron.-Clim. Chang. Food Secur*, 6:73, 2020.

[3] Precision Agriculture in the 21st Century: Geospatial and Information Technologies in Crop Management. Report, National Research Council, 1997.

[4] Manoj Karkee and Qin Zhang. *Fundamentals of agricultural and field robotics*. Springer, 2021.

[5] Andreas Krietemeyer, Marie Claire ten Veldhuis, Hans van der Marel, Eugenio Realini, and Nick van de Giesen. Potential of cost-efficient single frequency GNSS receivers for water vapor monitoring. *Remote Sensing*, 10(9):1493, 2018.

[6] The European Commission and The European GNSS Agency. GNSS Market Report. Technical Report 4, 2015.

[7] E D Kaplan and C J Hegarty. *Understanding GPS/GNSS: Principles and Applications*. Artech House mobile communications series. Artech House, 2017.

[8] European Union Agency for the Space Programme. What is SBAS?, 2021.

[9] G. Langfelder and A. Tocchio. MEMS integrating motion and displacement sensors. In Stoyan Nihtianov and Antonio Luque, editors, *Smart Sensors and MEMS: Intelligent Devices and Microsystems for Industrial Applications*, pages 366–401. Woodhead Publishing, 2013.

[10] Andrea Cirillo, Pasquale Cirillo, Giuseppe De Maria, Ciro Natale, and Salvatore Pirozzi. A comparison of multisensor attitude estimation algorithms. *Multisensor Attitude Estimation: Fundamental Concepts and Applications*, pages 529–540, 2016.

[11] Minh Long Hoang, Antonio Pietrosanto, Salvatore Dello Iacono, and Vincenzo Paciello. Pre-processing technique for compass-less madgwick in heading estimation for industry 4.0. In *I2MTC 2020 - International Instrumentation and Measurement Technology Conference, Proceedings*, pages 1–6, 2020.

[12] Fernando Alfredo Auat Cheein and Ricardo Carelli. Agricultural robotics: Unmanned robotic service units in agricultural tasks. *IEEE Industrial Electronics Magazine*, 7(3):48–58, 2013.

[13] Paul Groves. *Principles of GNSS, Inertial, and Multisensor Integrated Navigation Systems, Second Edition*. 2013.

[14] Jorge A. Heraud and Arthur F. Lange. *Agricultural automatic vehicle guidance from horses to GPS: How we got here, and where we are going*. American Society of Agricultural and Biological Engineers St. Joseph, 2009.

[15] Thomas Gordon Kirk, GC Zoerb, and JN Wilson. *A furrow-following tractor guidance system*. PhD thesis, University of Saskatchewan, 1974.

[16] MB Widden and JR Blair. A new automatic tractor guidance system. *Journal of Agricultural Engineering Research*, 17(1):10–21, 1972.

[17] Gerhard Jahns. *Automatic guidance in agriculture: A review*. ASAE, 1983.

[18] J N Wilson. Guidance of agricultural vehicles—a historical perspective. *Computers and electronics in agriculture*, 25(1-2):3–9, 2000.

[19] H W Griepentrog, B S Blackmore, and S G Vougioukas. 4.2 Positioning and Navigation. 2006.

[20] Avital Bechar and Clement Vigneault. Agricultural robots for field operations: Concepts and components. *Biosystems Engineering*, 149:94–111, 2016.

[21] Johann Borenstein, Hobart R Everett, Liqiang Feng, and David Wehe. Mobile robot positioning: Sensors and techniques. *Journal of robotic systems*, 14(4):231–249, 1997.

[22] Ming Li, Kenji Imou, Katsuhiro Wakabayashi, and Shinya Yokoyama. Review of research on agricultural vehicle autonomous guidance. *International Journal of Agricultural and Biological Engineering*, 2(3):1–16, 2009.

[23] D G Gunderson, T G Kirk, and J N Wilson. Feasibility study of closed circuit TV as a guidance assist for field equipment. *American Society of Agricultural Engineers Paper NCR*, pages 82–117, 1982.

[24] John B. Gerrish, George C. Stockman, Lixin Mann, and Gongzhu Hu. Path-finding by image processing in agricultural field operations. *SAE Technical Papers*, pages 540–554, 1986.

[25] John Franklin Reid. *The development of computer vision algorithms for agricultural vehicle guidance*. Texas A&M University, 1987.

[26] J R Brandon, S W Searcy, and R J Babowicz. Distributed control for vision based tractor guidance. *Paper-American Society of Agricultural Engineers (USA)*, 1989.

[27] Neil H. Brown, Hugh C. Wood, and James N. Wilson. Development of Guidance System Using Local Sensors for Agricultural Vehicles. In *Optics in Agriculture*, volume 1379, pages 54–68. SPIE, 1991.

[28] J. Billingsley and M. Schoenfisch. The successful development of a vision guidance system for agriculture. *Computers and Electronics in Agriculture*, 16(2):147–163, 1997.

[29] M A Dickson, B Ni, J F Reid, Q Zhang, and Others. A Robust Procedure to Obtain a Guidance Directrix for Vision-Based Vehicle Guidance Systems. In *Automation Technology for Off-Road Equipment Proceedings of the 2002 Conference*, page 317. American Society of Agricultural and Biological Engineers, 2002.

[30] E. R. Benson, J. F. Reid, and Q. Zhang. Machine Vision-based Guidance System for Agricultural Grain Harvesters using Cut-edge Detection. *Biosystems Engineering*, 86(4):389–398, 2003.

[31] Masahiko Yokota, Akira Mizushima, Kazunobu Ishii, and Noboru Noguchi. 3-D GIS map generation using a robot tractor with a laser scanner. In *2005 ASAE Annual Meeting*, page 1. American Society of Agricultural and Biological Engineers, 2005.

[32] T Satow, K Matsuda, S B Ming, K Hironaka, and D L S Tan. Development of laser crop row sensor for automatic guidance system of implements. In *Automation Technology for Off-Road Equipment Proceedings of the 2004 Conference*, page 131. American Society of Agricultural and Biological Engineers, 2004.

[33] Oscar Cabanero Barawid. *Development of electronic utility robot vehicle.* PhD thesis, Hokkaido University, 2010.

[34] Ulrich Weiss and Peter Biber. Plant detection and mapping for agricultural robots using a 3D LIDAR sensor. *Robotics and autonomous systems*, 59(5):265–273, 2011.

[35] Jacqueline Libby and George Kantor. Deployment of a point and line feature localization system for an outdoor agriculture vehicle. In *2011 IEEE International Conference on Robotics and Automation*, pages 1565–1570. IEEE, 2011.

[36] N Shalal, T Low, C McCarthy, and N Hancock. A review of autonomous navigation systems in agricultural environments. 2013.

[37] T Hague, J A Marchant, and N D Tillett. Ground based sensing systems for autonomous agricultural vehicles. *Computers and Electronics in Agriculture*, 25(1-2):11–28, 2000.

[38] Qin Zhang. *Precision agriculture technology for crop farming.* Taylor & Francis, 2016.

[39] M Toda, O Kitani, T Okamoto, and T Torii. Navigation method for a mobile robot via sonar-based crop row mapping and fuzzy logic control. *Journal of Agricultural Engineering Research*, 72(4):299–309, 1999.

[40] M Iida and T F Burks. Ultrasonic sensor development for automatic steering control of orchard tractor. In *Automation Technology for Off-Road Equipment Proceedings of the 2002 Conference*, page 221. American Society of Agricultural and Biological Engineers, 2002.

[41] I H Celen, E Onler, and E Kilic. A design of an autonomous agricultural robot to navigate between rows. In *2015 International Conference on Electrical, Automation and Mechanical Engineering*, pages 349–352. Atlantis Press, 2015.

[42] Joseph S Dvorak, Marvin L Stone, and Kelvin P Self. Object detection for agricultural and construction environments using an ultrasonic sensor. *Journal of agricultural safety and health*, 22(2):107–119, 2016.

[43] Limin Liu, Yajia Liu, Xiongkui He, and Weihong Liu. Precision variable-rate spraying robot by using single 3d lidar in orchards. *Agronomy*, 12(10):2509, 2022.

[44] Samuel J LeVoir, Peter A Farley, Tao Sun, and Chong Xu. High-accuracy adaptive low-cost location sensing subsystems for autonomous rover in precision agriculture. *IEEE Open Journal of Industry Applications*, 1:74–94, 2020.

[45] Gokhan Bayar, Marcel Bergerman, A Bugra Koku, and E Ilhan Konukseven. Localization and control of an autonomous orchard vehicle. *Computers and Electronics in Agriculture*, 115:118–128, 2015.

[46] Chika Yinka-Banjo and Olasupo Ajayi. Sky-Farmers: Applications of Unmanned Aerial Vehicles (UAV) in Agriculture. In George Dekoulis, editor, *Autonomous Vehicles*, chapter 6. IntechOpen, Rijeka, 2019.

[47] Michael O'Connor, Thomas Bell, Gabriel Elkaim, and Bradford Parkinson. Automatic steering of farm vehicles using gps. In *Proceedings of the Third International Conference on Precision Agriculture*, pages 767–777. Wiley Online Library, 1996.

[48] Qin Zhang, John F Reid, and Noboru Noguchi. Agricultural vehicle navigation using multiple guidance sensors. In *Proceedings of the international conference on field and service robotics*, pages 293–298. Citeseer, 1999.

[49] Francisco Rovira Más, Qin Zhang, and Alan C Hansen. *Mechatronics and intelligent systems for off-road vehicles*. Springer Science & Business Media, 2010.

[50] Han Shufeng, He Yong, and Fang Hui. Recent development in automatic guidance and autonomous vehicle for agriculture: A Review. *Journal of Zhejiang University*, 44(4):381–391, 2018.

[51] UNITED NATIONS Office for Outer Space Affairs. Global Navigation Satellite Systems (GNSS). Accessed: 2023-10-30.

[52] Dmytro Lenniy. How to Pair GPS Agriculture Tools with Advanced Technologies. [Accessed 02-11-2023].

[53] Spyros Fountas, Katerina Aggelopoulou, and Theofanis A Gemtos. Precision agriculture: crop management for improved productivity and reduced environmental impact or improved sustainability. *Supply chain management for sustainable food networks*, pages 41–65, 2015.

[54] Manuel Pérez Ruiz and Shrini Upadhyaya. *GNSS in precision agricultural operations*. Intech, 2012.

[55] John Alexander Thomasson, Craig P Baillie, Diogenes L Antille, Craig R Lobsey, Cheryl L McCarthy, et al. *Autonomous technologies in agricultural equipment: a review of the state of the art*. American Society of Agricultural and Biological Engineers St. Joseph, MI, USA, 2019.

[56] National Coordination Office for Space-Based Positioning, Navigation, and Timing. Gps.gov: Space segment. [Accessed 02-10-2023].

[57] Ronald William and Hedgecock Ii. *Precise Real-Time Relative Localization Using Single-Frequency GPS*. Dissertation, Vanderbilt University, Nashville, 2014.

[58] National Coordination Office for Space-Based Positioning, Navigation, and Timing. Gps.gov: Control segment. [Accessed 04-11-2023].

[59] Navstar GPS Space Segment/ User Segment L5 Interfaces. Interface Specification Document, Space and Missile Systems Center, 2022.

[60] Àvila Rodrìguez J.A. GPS Signal Plan. Accessed: 2023-11-13.

[61] Amit Kumar, Shubham Kumar, Preet Lal, Purabi Saikia, Prashant K Srivastava, and George P Petropoulos. Introduction to gps/gnss technology. In *GPS and GNSS Technology in Geosciences*, pages 3–20. Elsevier, 2021.

[62] Jan Van Sickle. *GPS and GNSS for Land Surveyors*. CRC Press, 2023.

[63] Global Positioning System Standard Positioning Service Performance Standard. Interface Specification Document, U.S. Department of Defense, 2020.

[64] Navstar GPS Space Segment/Navigation User Interfaces IS-GPS-200. Interface Specification Document, Space and Missile Systems Center, 2021.

[65] Malek Karaim. *Ultra-tight GPS/INS integrated system for land vehicle navigation in challenging environments*. PhD thesis, Queen's University (Canada), 2019.

[66] José Darrozes, Nicolas Roussel, and Mehrez Zribi. 7 - the reflected global navigation satellite system (gnss-r): from theory to practice. In Nicolas Baghdadi and Mehrez Zribi, editors, *Microwave Remote Sensing of Land Surface*, pages 303–355. Elsevier, 2016.

[67] Pavan Kumar, Prashant K. Srivastava, Prasoon Tiwari, and R. K. Mall. *Application of GPS and GNSS technology in geosciences*. Elsevier Science, 2021.

[68] André Silva Aguiar, Filipe Neves dos Santos, José Boaventura Cunha, Héber Sobreira, and Armando Jorge Sousa. Localization and mapping for robots in agriculture and forestry: A survey. *Robotics*, 9(4):97, 2020.

[69] Marcos Duarte, Filipe Neves dos Santos, Armando Sousa, and Raul Morais. Agricultural wireless sensor mapping for robot localization. In *Robot 2015: Second Iberian Robotics Conference: Advances in Robotics, Volume 1*, pages 359–370. Springer, 2016.

[70] Jawad Iqbal, Rui Xu, Shangpeng Sun, and Changying Li. Simulation of an autonomous mobile robot for lidar-based in-field phenotyping and navigation. *Robotics*, 9(2):46, 2020.

[71] Marco Bietresato, Giovanni Carabin, Daniela D'Auria, Raimondo Gallo, Gianluca Ristorto, Fabrizio Mazzetto, Renato Vidoni, Alessandro Gasparetto, and Lorenzo Scalera. A tracked mobile robotic lab for monitoring the plants volume and health. In *2016 12th IEEE/ASME International Conference on Mechatronic and Embedded Systems and Applications (MESA)*, pages 1–6. IEEE, 2016.

[72] Trygve Utstumo, Frode Urdal, Anders Brevik, Jarle Dørum, Jan Netland, Øyvind Overskeid, Therese W Berge, and Jan Tommy Gravdahl. Robotic in-row weed control in vegetables. *Computers and electronics in agriculture*, 154:36–45, 2018.

[73] Y G Ampatzidis, S G Vougioukas, D D Bochtis, and C A Tsatsarelis. A yield mapping system for hand-harvested fruits based on RFID and GPS location technologies: field testing. *Precision agriculture*, 10(1):63–72, 2009.

[74] N Alam, AT Balaei, and AG Dempster. Range and range-rate measurements using DSRC: facts and challenges. In *IGNSS Symposium*, 2009.

[75] Liu Jixiu, Ye Quan, Shu Leizheng, and Gao Yang. Relative Position and Attitude Estimation of Non-cooperative Spacecraft Based on Stereo Camera and Dynamics. *Journal of Physics: Conference Series*, 1924(1):12025, 2021.

[76] Daiqin Yang, Fang Zhao, Kai Liu, Hock Beng Lim, Emilio Frazzoli, and Daniela Rus. A GPS pseudorange based cooperative vehicular distance measurement technique. In *IEEE Vehicular Technology Conference*, pages 1–5. IEEE, 2012.

[77] Nima Alam, Allison Kealy, and Andrew G. Dempster. An INS-aided tight integration approach for relative positioning enhancement in VANETs. *IEEE Transactions on Intelligent Transportation Systems*, 14(4):1992–1996, 2013.

[78] Fabian De Ponte Müller, Alexander Steingass, and Thomas Strang. Zero-baseline measurements for relative positioning in vehicular environments. In *6th European Workshop on GNSS Signals and Signal Processing*, 2013.

[79] W Trigos, G Pedraza, and R Ramos-Pollan. A Differential Cooperative Positioning Approach for Multi-Device Positioning Improvement. *Ingenieria Solidaria*, 15(28):1–30, 2019.

[80] Will Hedgecock, Miklos Maroti, Janos Sallai, Peter Volgyesi, and Akos Ledeczi. High-accuracy differential tracking of low-cost GPS receivers. In *MobiSys 2013 - Proceedings of the 11th Annual International Conference on Mobile Systems, Applications, and Services*, pages 221–234, 2013.

[81] Fabian De Ponte Müller, Estefania Munoz Diaz, Bernhard Kloiber, and Thomas Strang. Bayesian cooperative relative vehicle positioning using pseudorange differences. In *Record - IEEE PLANS, Position Location and Navigation Symposium*, pages 434–444, 2014.

[82] Jiawen Shen, Shizhuang Wang, Yawei Zhai, and Xingqun Zhan. Cooperative relative navigation for multi-UAV systems by exploiting GNSS and peer-to-peer ranging measurements. *IET Radar, Sonar and Navigation*, 15(1):21–36, 2020.

[83] Khaoula Lassoued, Philippe Bonnifait, and Isabelle Fantoni. Cooperative localization of vehicles sharing GNSS pseudoranges corrections with no base station using set inversion. In *IEEE Intelligent Vehicles Symposium Proceedings*, volume 2016-August, pages 496–501. IEEE, 2016.

[84] Kai Liu, Hock Beng Lim, Emilio Frazzoli, Houling Ji, and Victor C.S. Lee. Improving positioning accuracy using GPS pseudorange measurements for cooperative vehicular localization. *IEEE Transactions on Vehicular Technology*, 63(6):2544–2556, 2014.

[85] Suhua Tang, Nao Kawanishi, Rei Furukawa, and Nobuaki Kubo. Experimental evaluation of cooperative relative positioning for intelligent transportation system. *International Journal of Navigation and Observation*, 2014, 2014.

[86] Muhammad Tahir, Sayed Saad Afzal, Muhammad Saad Chughtai, and Khurram Ali. On the Accuracy of Inter-Vehicular Range Measurements Using GNSS Observables in a Cooperative Framework. *IEEE Transactions on Intelligent Transportation Systems*, 20(2):682–691, 2019.

[87] Alex Minetto, Calogero Cristodaro, and Fabio Dovis. A collaborative method for positioning based on GNSS inter agent range estimation. In *25th European Signal Processing Conference, EUSIPCO 2017*, volume 2017-January, pages 2714–2718, 2017.

[88] Vincent Havyarimana, Zhu Xiao, Pierre Claver Bizimana, Damien Hanyurwimfura, and Hongbo Jiang. Toward Accurate Intervehicle Positioning Based on GNSS Pseudorange Measurements under Non-Gaussian Generalized Errors. *IEEE Transactions on Instrumentation and Measurement*, 70:1–12, 2020.

[89] Alex Minetto, Andrea Nardin, and Fabio Dovis. Modelling and experimental assessment of inter-personal distancing based on shared GNSS observables. *Sensors*, 21(8):2588, 2021.

[90] Gerardo Allende-Alba, Oliver Montenbruck, Stefan Hackel, and Michel Tossaint. Relative positioning of formation-flying spacecraft using single-receiver GPS carrier phase ambiguity fixing. *GPS Solutions*, 22(3):1–11, 2018.

[91] Adyasha Mohanty, Asta Wu, Sriramya Bhamidipati, and Grace Gao. Precise Relative Positioning via Tight-Coupling of GPS Carrier Phase and Multiple UWBs. *IEEE Robotics and Automation Letters*, 7(2):5757–5762, 2022.

[92] Shuqing Zeng. Performance evaluation of automotive radars using carrier-phase differential GPS. *IEEE Transactions on Instrumentation and Measurement*, 59(10):2732–2741, 2010.

[93] Scott Martin, William Travis, and David Bevly. Performance comparison of single and dual frequency closely coupled GPS/INS relative positioning systems. In *Record - IEEE PLANS, Position Location and Navigation Symposium*, pages 544–551, 2010.

[94] Marco Rao and Gianluca Falco. Code Tracking and Pseudorange. *InsideGNSS*, (January / February):26–33, 2012.

[95] Faan Wang, Weichao Zhuang, Guodong Yin, Shuaipeng Liu, Ying Liu, and Haoxuan Dong. Robust inter-vehicle distance measurement using cooperative vehicle localization. *Sensors*, 21(6):2048, 2021.

[96] u-blox. NEO-6 Data Sheet, 2011.

[97] Nordic Semiconductor. nRF2401 Single Chip 2.4 GHz Radio Transceiver, 2008.

[98] Raspberry Pi Foundation. Raspberry Pi 3 Model B+, 2018.

[99] The Geany contributors. Geany - The Flyweight IDE.

[100] PyPI. pyserial 3.5, 2020.

[101] PyPI. spidev 3.6, 2020.

[102] Brian Lavery. lib_nrf24, 2018.

[103] u-blox. ZED-F9P Product Summary, 2023.

[104] Robert Grisson, Mark Alley, and Conrad HeatWole. Precision Farming Tools: Global Positioning System (GPS). In *Virginia Cooperative Extension*, pages 442–503, 2009.

[105] Hassen Fourati and Djamel Eddine Chouaib Belkhiat. *Multisensor attitude estimation: fundamental concepts and applications*. CRC Press, 2016.

[106] Richard M Murray, Zexiang Li, and S Shankar Sastry. *A mathematical introduction to robotic manipulation*. CRC press, 2017.

[107] Xiaoji Niu, Tao Liu, Jian Kuang, Quan Zhang, and Chi Guo. Pedestrian trajectory estimation based on foot-mounted inertial navigation system for multistory buildings in postprocessing mode. *IEEE Internet of Things Journal*, 9(9):6879–6892, 2021.

[108] Hongze Yang, Yong Lu, Zhiyong Zheng, Sheng Liu, Guobao He, Shen Chen, and Qianen He. Reliability enhancement method of attitude estimation for wearable motion capture systems in human lower limb rehabilitation. *IEEE Sensors Journal*, 2023.

[109] Juyoung Lee, Sang Chul Ahn, and Jae-In Hwang. A walking-in-place method for virtual reality using position and orientation tracking. *Sensors*, 18(9), 2018.

[110] Qilong Yuan, Ehsan Asadi, Qinghua Lu, Guilin Yang, and I-Ming Chen. Uncertainty-based imu orientation tracking algorithm for dynamic motions. *IEEE/ASME Transactions on mechatronics*, 24(2):872–882, 2019.

[111] Christian Eling, Philipp Zeimetz, and Heiner Kuhlmann. Development of an instantaneous gnss/mems attitude determination system. *GPS solutions*, 17:129–138, 2013.

[112] Mattia Giurato and Marco Lovera. Quadrotor attitude determination: a comparison study. In *2016 IEEE Conference on Control Applications (CCA)*, pages 21–26. IEEE, 2016.

[113] Wei Ding. *Attitude Estimation Methods Using Low-cost GNSS and MEMS MARG Sensors and Their Integration*. Dissertation, University of Calgary, Alberta, 2022.

[114] Hashim A. Hashim. Attitude determination and estimation using vector observations: Review, challenges and comparative results. *arXiv preprint arXiv:2001.03787*, 2020.

[115] Harold D Black. A passive system for determining the attitude of a satellite. *AIAA journal*, 2(7):1350–1351, 1964.

[116] Malcolm David Shuster and S D_ Oh. Three-axis attitude determination from vector observations. *Journal of guidance and Control*, 4(1):70–77, 1981.

[117] F Landis Markley. Attitude determination using vector observations and the singular value decomposition. *Journal of the Astronautical Sciences*, 36(3):245–258, 1988.

[118] F Landis Markley and John L Crassidis. *Fundamentals of spacecraft attitude determination and control*, volume 1286. Springer, 2014.

[119] Fuzhen Zhang. Quaternions and matrices of quaternions. *Linear algebra and its applications*, 251:21–57, 1997.

[120] Paul Groves. *Principles of GNSS, Inertial, and Multisensor Integrated Navigation Systems, Second Edition*. 2013.

[121] Djamel Dhahbane, Abdelkrim Nemra, and Samir Sakhi. Attitude determination and attitude estimation in aircraft and spacecraft navigation. a survey. In *2020 2nd International Workshop on Human-Centric Smart Environments for Health and Well-being (IHSH)*, pages 187–192. IEEE, 2021.

[122] Xiaoping Yun, Eric R Bachmann, and Robert B McGhee. A simplified quaternion-based algorithm for orientation estimation from earth gravity and magnetic field measurements. *IEEE Transactions on instrumentation and measurement*, 57(3):638–650, 2008.

[123] James Diebel. Representing attitude: Euler angles, unit quaternions, and rotation vectors. *Matrix*, 58(15-16):1–35, 2006.

[124] Daniel Choukroun, Itzhack Y Bar-Itzhack, and Yaakov Oshman. Novel quaternion kalman filter. *IEEE Transactions on Aerospace and Electronic Systems*, 42(1):174–190, 2006.

[125] Zhaomin Ma, Zhengqiang Chen, and Ling Huang. A review: The survey of attitude estimation in autonomous uav navigation. In *2019 International Conference on Wireless Communication, Network and Multimedia Engineering (WCNME 2019)*, pages 50–53. Atlantis Press, 2019.

[126] Lan Huang, Jianmei Song, and Chunyan Zhang. Observability analysis and filter design for a vision inertial absolute navigation system for uav using landmarks. *Optik*, 149:455–468, 2017.

[127] Junho Yang, Ashwin Dani, Soon-Jo Chung, and Seth Hutchinson. Vision-based localization and robot-centric mapping in riverine environments. *Journal of Field Robotics*, 34(3):429–450, 2017.

[128] Lin Zhao, Na Li, Liang Li, Yi Zhang, and Chun Cheng. Real-time gnss-based attitude determination in the measurement domain. *Sensors*, 17(2):296, 2017.

[129] Xing Liu, Tarig Ballal, and Tareq Y Al-Naffouri. Gnss attitude determination using a constrained wrapped least squares approach. In *2020 IEEE/ION Position, Location and Navigation Symposium (PLANS)*, pages 1135–1139. IEEE, 2020.

[130] Zhang Nan, Sun Jianfeng, Jiang Peng, Liu Di, and Wang Penghui. Pose estimation algorithms for lidar scene based on point normal vector. *Infrared and Laser Engineering*, 49(1):0105004, 2020.

[131] Jin Q Cui, Shupeng Lai, Xiangxu Dong, and Ben M Chen. Autonomous navigation of uav in foliage environment. *Journal of intelligent & robotic systems*, 84:259–276, 2016.

[132] G Ajay Kumar, Ashok Kumar Patil, Rekha Patil, Seong Sill Park, and Young Ho Chai. A lidar and imu integrated indoor navigation system for uavs and its application in real-time pipeline classification. *Sensors*, 17(6):1268, 2017.

[133] Marco Carratù, Salvatore Dello Iacono, Minh Long Hoang, and Antonio Pietrosanto. Energy characterization of attitude algorithms. In *2019 IEEE 17th International Conference on Industrial Informatics (INDIN)*, volume 1, pages 1585–1590. IEEE, 2019.

[134] Marco Caruso, Angelo Maria Sabatini, Marco Knaflitz, Ugo Della Croce, and Andrea Cereatti. Extension of the rigid-constraint method for the heuristic suboptimal parameter tuning to ten sensor fusion algorithms using inertial and magnetic sensing. *Sensors*, 21(18):6307, 2021.

[135] Xu Ru, Nian Gu, Hang Shang, and Heng Zhang. Mems inertial sensor calibration technology: Current status and future trends. *Micromachines*, 13(6):879, 2022.

[136] Milad Nazarahari and Hossein Rouhani. Sensor fusion algorithms for orientation tracking via magnetic and inertial measurement units: An experimental comparison survey. *Information Fusion*, 76:8–23, 2021.

[137] Daniel Weber, Clemens Gühmann, and Thomas Seel. Neural networks versus conventional filters for inertial-sensor-based attitude estimation. In *2020 IEEE 23rd International Conference on Information Fusion (FUSION)*, pages 1–8. IEEE, 2020.

[138] Rudolph Emil Kalman. A new approach to linear filtering and prediction problems. 1960.

[139] Roberta Veloso Garcia, Paula Cristiane Pinto Mesquita Pardal, HK Kuga, and MC Zanardi. Nonlinear filtering for sequential spacecraft attitude estimation with real data: Cubature kalman filter, unscented kalman filter and extended kalman filter. *Advances in Space Research*, 63(2):1038–1050, 2019.

[140] Gabriele Ligorio and Angelo M Sabatini. A novel kalman filter for human motion tracking with an inertial-based dynamic inclinometer. *IEEE Transactions on Biomedical Engineering*, 62(8):2033–2043, 2015.

[141] Pedro Neto, Nuno Mendes, and António Paulo Moreira. Kalman filter-based yaw angle estimation by fusing inertial and magnetic sensing. In *CONTROLO'2014–Proceedings of the 11th Portuguese Conference on Automatic Control*, pages 679–688. Springer, 2015.

[142] Ramasamy Kannan. Orientation estimation based on lkf using differential state equation. *IEEE Sensors Journal*, 15(11):6156–6163, 2015.

[143] Romy Budhi Widodo, Chikamune Wada, et al. Attitude estimation using kalman filtering: external acceleration compensation considerations. *Journal of Sensors*, 2016, 2016.

[144] Jouni Hartikainen, Arno Solin, and Simo Särkkä. Optimal filtering with kalman filters and smoothers. *Department of biomedica engineering and computational sciences, Aalto University School of Science, 16th August*, 2011.

[145] M Koifman and SJ Merhav. Autonomously aided strapdown attitude reference system. *Journal of guidance, control, and dynamics*, 14(6):1164–1172, 1991.

[146] Young-Soo Suh, Sang-Kyeong Park, Hee-Jun Kang, and Young-Shick Ro. Attitude estimation adaptively compensating external acceleration. *JSME International Journal Series C Mechanical Systems, Machine Elements and Manufacturing*, 49(1):172–179, 2006.

[147] Phillip Tome and Okan Yalak. Improvement of orientation estimation in pedestrian navigation by compensation of magnetic disturbances. *Navigation*, 55(3):179–190, 2008.

[148] Qigao Fan, Hai Zhang, Peng Pan, Xiangpeng Zhuang, Jie Jia, Pengsong Zhang, Zhengqing Zhao, Gaowen Zhu, and Yuanyuan Tang. Improved pedestrian dead reckoning based on a robust adaptive kalman filter for indoor inertial location system. *Sensors*, 19(2):294, 2019.

[149] Zhi-An Deng, Guofeng Wang, Ying Hu, and Di Wu. Heading estimation for indoor pedestrian navigation using a smartphone in the pocket. *Sensors*, 15(9):21518–21536, 2015.

[150] Pablo Bernal-Polo and Humberto Martínez Barberá. Orientation estimation by means of extended kalman filter, quaternions, and charts. 2017.

[151] Sebastjan Šlajpah, Roman Kamnik, and Marko Munih. Compensation for magnetic disturbances in motion estimation to provide feedback to wearable robotic systems. *IEEE Transactions on Neural Systems and Rehabilitation Engineering*, 25(12):2398–2406, 2017.

[152] Simon J Julier and Jeffrey K Uhlmann. Unscented filtering and nonlinear estimation. *Proceedings of the IEEE*, 92(3):401–422, 2004.

[153] Ienkaran Arasaratnam and Simon Haykin. Cubature kalman filters. *IEEE Transactions on automatic control*, 54(6):1254–1269, 2009.

[154] Marco Caruso, Angelo Maria Sabatini, Daniel Laidig, Thomas Seel, Marco Knaflitz, Ugo Della Croce, and Andrea Cereatti. Analysis of the accuracy of ten algorithms for orientation estimation using inertial and magnetic sensing under optimal conditions: One size does not fit all. *Sensors*, 21(7):2543, 2021.

[155] Minh Long Hoang, Salvatore Dello Iacono, Vincenzo Paciello, and Antonio Pietrosanto. Measurement optimization for orientation tracking based on no motion no integration technique. *IEEE Transactions on Instrumentation and Measurement*, 70:1–10, 2020.

[156] Milad Nazarahari and Hossein Rouhani. 40 years of sensor fusion for orientation tracking via magnetic and inertial measurement units: Methods, lessons learned, and future challenges. *Information Fusion*, 68:67–84, 2021.

[157] Sebastian OH Madgwick, Andrew JL Harrison, and Ravi Vaidyanathan. Estimation of imu and marg orientation using a gradient descent algorithm. In *2011 IEEE international conference on rehabilitation robotics*, pages 1–7. IEEE, 2011.

[158] Robert Mahony, Tarek Hamel, and Jean-Michel Pflimlin. Nonlinear complementary filters on the special orthogonal group. *IEEE Transactions on automatic control*, 53(5):1203–1218, 2008.

[159] Simone A Ludwig and Kaleb D Burnham. Comparison of euler estimate using extended kalman filter, madgwick and mahony on quadcopter flight data. In *2018 International Conference on Unmanned Aircraft Systems (ICUAS)*, pages 1236–1241. IEEE, 2018.

[160] Ming Zhang, Mingming Zhang, Yiming Chen, and Mingyang Li. Imu data processing for inertial aided navigation: A recurrent neural network based approach. In *2021 IEEE International Conference on Robotics and Automation (ICRA)*, pages 3992–3998. IEEE, 2021.

[161] Mohammad K Al-Sharman, Yahya Zweiri, Mohammad Abdel Kareem Jaradat, Raghad Al-Husari, Dongming Gan, and Lakmal D Seneviratne. Deep-learning-based neural network training for state estimation enhancement: Application to attitude estimation. *IEEE Transactions on Instrumentation and Measurement*, 69(1):24–34, 2019.

[162] Ruihao Li, Chunlian Fu, Wei Yi, and Xiaodong Yi. Calib-net: Calibrating the low-cost imu via deep convolutional neural network. *Frontiers in Robotics and AI*, 8:772583, 2022.

[163] Jau-Hsiung Wang and Yang Gao. A new magnetic compass calibration algorithm using neural networks. *Measurement Science and Technology*, 17(1):153, 2005.

[164] Rita Fontanella, Domenico Accardo, Egidio Caricati, Stefano Cimmino, Domenico De Simone, and Giovanni Lucignano. Improving inertial attitude measurement performance by exploiting mems gyros and neural thermal calibration. In *AIAA Information Systems-AIAA Infotech@ Aerospace*, page 1134. 2017.

[165] Kai-Wei Chiang, Hsiu-Wen Chang, Chia-Yuan Li, and Yun-Wen Huang. An artificial neural network embedded position and orientation determination algorithm for low cost mems ins/gps integrated sensors. *Sensors*, 9(4):2586–2610, 2009.

[166] Djamel Dhahbane, Abdelkrim Nemra, and Samir Sakhi. Neural network-based attitude estimation. In *Artificial Intelligence and Renewables Towards an Energy Transition 4*, pages 500–511. Springer, 2021.

[167] Mahdi Abolfazli Esfahani, Han Wang, Keyu Wu, and Shenghai Yuan. Orinet: Robust 3-d orientation estimation with a single particular imu. *IEEE Robotics and Automation Letters*, 5(2):399–406, 2019.

[168] Peng Li, Wen-An Zhang, Yuqiang Jin, Zihan Hu, and Linqing Wang. Attitude estimation using iterative indirect kalman with neural network for inertial sensors. *IEEE Transactions on Instrumentation and Measurement*, 2023.

[169] Daniel Weber, Clemens Gühmann, and Thomas Seel. Riann—a robust neural network outperforms attitude estimation filters. *AI*, 2(3):444–463, 2021.

[170] Yaohua Liu, Yimin Zhou, and Xiang Li. Attitude estimation of unmanned aerial vehicle based on lstm neural network. In *2018 international joint conference on neural networks (IJCNN)*, pages 1–6. IEEE, 2018.

[171] Arman Asgharpoor Golroudbari and Mohammad Hossein Sabour. Generalizable end-to-end deep learning frameworks for real-time attitude estimation using 6dof inertial measurement units. *Measurement*, 217:113105, 2023.

[172] Valérie Renaudin, Muhammad Haris Afzal, and Gérard Lachapelle. Complete triaxis magnetometer calibration in the magnetic domain. *Journal of Sensors*, 2010, 2010.

[173] Jiakun Li, Kuangi Shu, and Heng Zhang. An efficient method for tri-axis magnetometer calibration. In *2019 IEEE SmartWorld, Ubiquitous Intelligence & Computing, Advanced & Trusted Computing, Scalable Computing & Communications, Cloud & Big Data Computing, Internet of People and Smart City Innovation (SmartWorld/SCALCOM/UIC/ATC/CBDCom/IOP/SCI)*, pages 654–660. IEEE, 2019.

[174] Alwin Poulose, Jihun Kim, and Dong Seog Han. Indoor localization with smartphones: Magnetometer calibration. In *2019 IEEE International Conference on Consumer Electronics (ICCE)*, pages 1–3. IEEE, 2019.

[175] InvenSense. MPU-9250 Product Specification, 2016.

[176] Shihao Xu, Ruizhi Chen, Yue Yu, Guangyi Guo, and Lixiong Huang. Locating smartphones indoors using built-in sensors and wi-fi ranging with an enhanced particle filter. *IEEE Access*, 7:95140–95153, 2019.

[177] Erol Duymaz and Berker Işik. A novel method for tilt compensation in inertial sensor systems. In *2021 29th Signal Processing and Communications Applications Conference (SIU)*, pages 1–4. IEEE, 2021.

[178] Mohamed E Hanafi, Mohammed AH Abozied, Yehia Z Elhalwagy, and Ahmed Omar Elfarouk. Multi-sensory data fusion for high performance attitude estimation. In *International Conference on Aerospace Sciences and Aviation Technology*, volume 18, pages 1–11. The Military Technical College, 2019.

[179] László Árvai and Szilvia Homolya. Filtering methods for indoor magnetic compass. In *2020 21th International Carpathian Control Conference (ICCC)*, pages 1–5. IEEE, 2020.

[180] Ashwin Ahuja, Andrea Ferlini, and Cecilia Mascolo. Pilotear: Enabling in-ear inertial navigation. In *Adjunct Proceedings of the 2021 ACM International Joint Conference on Pervasive and Ubiquitous Computing and Proceedings of the 2021 ACM International Symposium on Wearable Computers*, pages 139–145, 2021.

[181] Shu Wang, Aiguo Wang, Mengyuan Ran, Li Liu, Yuxin Peng, Ming Liu, Guoxin Su, Adi Alhudhaif, Fayadh Alenezi, and Norah Alnaim. Hand gesture recognition framework using a lie group based spatio-temporal recurrent network with multiple hand-worn motion sensors. *Information Sciences*, 606:722–741, 2022.

[182] Jozef Zurada, Alan S. Levitan, and Jian Guan. A comparison of regression and artificial intelligence methods in a mass appraisal context. *Journal of Real Estate Research*, 33(3):349–387, 2011.

[183] Antoni Ligeza. *Artificial Intelligence: A Modern Approach*, volume 9. Pearson Education, Inc., 1995.

[184] Charalampos Bratsas, Kleanthis Koupidis, Josep-Maria Salanova, Konstantinos Giannakopoulos, Aristeidis Kaloudis, and Georgia Aifadopoulou. A comparison of machine learning methods for the prediction of traffic speed in urban places. *Sustainability*, 12(1):142, 2019.

[185] Boran Sekeroglu, Yoney Kirsal Ever, Kamil Dimililer, and Fadi Al-Turjman. Comparative evaluation and comprehensive analysis of machine learning models for regression problems. *Data Intelligence*, 4(3):620–652, 2022.

[186] Ivan Nunes da Silva, Danilo Hernane Spatti, Rogerio Andrade Flauzino, Luisa Helena Bartocci Liboni, and Silas Franco dos Reis Alves. *Artificial neural networks: A practical course*. Springer International Publishing, 2016.

[187] Nicholas Lange, C. M. Bishop, and B. D. Ripley. *Neural Networks for Pattern Recognition.*, volume 92. Oxford University Press, USA, 1997.

[188] Max Kuhn and Kjell Johnson. *Feature engineering and selection: A practical approach for predictive models*. CRC Press, 2019.

[189] Ian H. Witten, Eibe Frank, Mark A. Hall, and Christopher J. Pal. *Data Mining: Practical Machine Learning Tools and Techniques*. Morgan Kaufmann, 2016.

[190] Mohamed H. Bakr and Mohamed H. Negm. Modeling and design of high-frequency structures using artificial neural networks and space mapping. In M Jamal Deen, editor, *Advances in Imaging and Electron Physics*, volume 174 of *Advances in Imaging and Electron Physics*, pages 223–260. Elsevier, 2012.

[191] Yann LeCun, Yoshua Bengio, and Geoffrey Hinton. Deep learning. *Nature*, 521(7553):436–444, 2015.

[192] Léon Bottou. *Stochastic gradient descent tricks*, volume 7700 LECTU, pages 421–436. Springer Berlin Heidelberg, Berlin, Heidelberg, 2012.

[193] Diederik P. Kingma and Jimmy Lei Ba. Adam: A method for stochastic optimization. *3rd International Conference on Learning Representations, ICLR 2015 - Conference Track Proceedings*, 2015.